MICROSCOPIC PROCESSES IN HETEROEPITAXIAL GROWTH: NUCLEATION, GROWTH AND ALLOYING OF SILVER ON THE (111) SURFACE OF PLATINIUM

PAR

HOLGER RÖDER

Physicien diplômé de l'Université de Bonn
de nationalité allemande

'
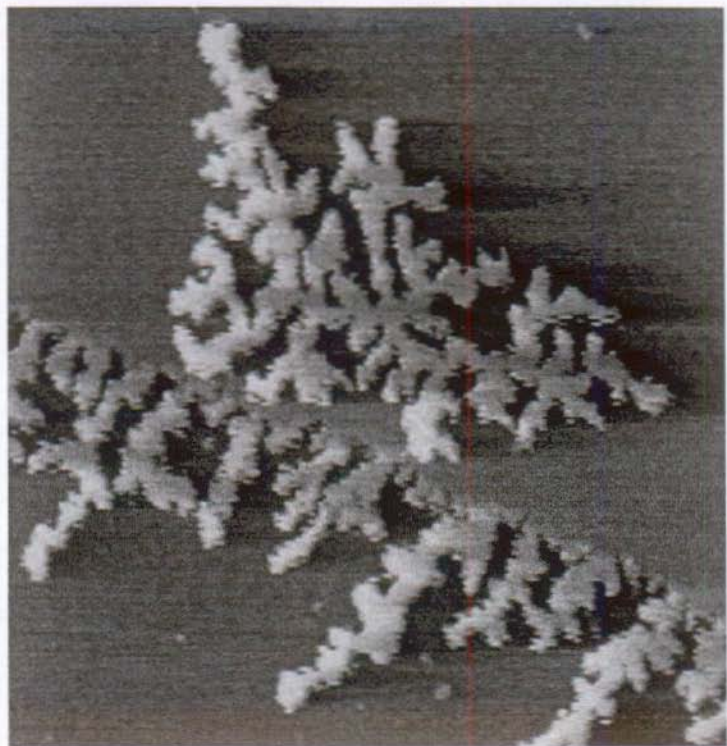
100 Å

Ramified Ag aggregate grown near a monatomic step on the Pt(111) surface

*"Wissenschaft ist der **Versuch**, der chaotischen Mannigfaltigkeit der Sinneserlebnisse, ein logisch einheitliches gedankliches System zuzuordnen."*

Albert Einstein (1940)

Résumé

Dans le but d'étudier les mécanismes microscopiques de l'épitaxie de couches métalliques ultraminces, un microscope à effet tunnel à température variable a été construit. Il permet d'effectuer des mesures *in situ* à des températures comprises entre T = 25K et 800K. Le système modèle Ag/Pt(111) est obtenu sous ultravide par condensation de la vapeur d'argent sur une surface monocristalline de Pt. Afin d'étudier les processus d'agrégation, les modifications morphologiques ont été visualisées en fonction de la température du substrat et du flux de déposition.

Dans le domaine au-dessous de la monocouche (ML: monolayer) et pour des températures de substrat comprises entre 35K et 500K, on observe une transition entre l'agrégation limitée par la diffusion et l'équilibre thermodynamique des films d'Ag. En contrôlant la température durant la croissance, des morphologies bidimensionnelles de l'Ag peuvent être sélectionnées de manière précise: distribution aléatoire d'adatomes et petits agrégats ou îlots dendritiques et grands îlots denses ou encore mélange bidimensionnel gaz-condensat à l'équilibre. Par recuit de l'Ag déposé à T ≤ 50K, on obtient un collection d'agrégats avec une étroite distribution de taille.

La nucléation à partir de la phase vapeur a été suivie à l'échelle atomique entre 50K et 130K. Pour T ≤ 110K, les germes stables pour la nucléation sont des dimères. Par comparaison avec les équations théoriques de taux de nucléation, on obtient une barrière de diffusion latérale des adatomes d'Ag sur Pt(111) E_D = 157±10 meV. Une estimation de l'énergie de liaison Ag-Ag donne E_2 = 320±30 meV.

Pour 110K ≤ T ≤ 130K, on observe en fonction du flux une transition entre une croissance ramifiée aléatoirement et la croissance fractale de dendrites. Son origine microscopique réside dans la différence entre les deux directions

de diffusion le long des bords données par le substrat. Cette anisotropie peut, d'une part, être dominante et la forme mésoscopique des agrégats obtenus est dendritique. Elle peut, d'autre part, être dégénérée et il en résulte des structures fractales ramifiées aléatoirement. Les barrières de diffusion ont été estimées à l'aide de modèles théoriques de croissance fractale.

Pour T > 620K et des taux de recouvrement Θ < 1 ML, la déposition d'Ag conduit à la formation d'un alliage bidimensionnel de surface. Celui-ci est constitué d'agrégats d'Ag dissous dans la couche de Pt et d'agrégats de Pt inclus dans la première couche d'Ag (0.5 ML < Θ < 1 ML). Cette dissolution se produit à partir des bords de marches et se trouve confinée dans la plus haute couche du support. Les grains enveloppés ont une étroite distribution de taille centrée autour de 10Å pour Θ < 0.25 ML et Θ > 0.75 ML. Aux recouvrements intermédiaires, les agrégats sont disposés en stries.

La croissance de la première couche d'Ag sur Pt(111) est pseudomorphique. La contrainte, issue du désaccord de maille de 4.3% dans la première couche d'Ag compressé, se relâche dans la seconde couche grâce à la formation de deux structures faiblement incommensurables: la phase métastable constituée de stries (T < 500K) et le réseau de parois de domaine obtenu lors d'un recuit (T > 700K). La troisième couche et les suivantes présentent un réseau hexagonal de dislocations que la microscopie à effet tunnel peut résoudre jusqu'à 15 ML. Lorsque le recouvrement atteint 25 ML, la structure est relaxée vers celle de l'Ag massif.

A T > 500K, les multicouches d'Ag forment un film continu. A plus basse température, le transport de masse entre couches étant bloqué, le régime de croissance devient cinétique. A partir d'un nombre critique de couches variant entre n^* = 1 (T = 130K) et n^* ≈ 10 (T ≈ 300K), la croissance devient tridimensionnelle. Pour différents intervalles de n^*, le transport de masse entre couches a été étudié en fonction de la mobilité de l'adatome, de la taille et de la forme des îlots terminaux ainsi que de la barrière d'activation V_e pour la descente d'une marche monoatomique.

Abstract

Microscopic processes in the epitaxial growth of thin metal films has been experimentally investigated. For this purpose a variable temperature scanning tunneling microscope has been constructed allowing *in situ* measurements between T = 25K and 800K. The studied model system is vapor phase deposition of silver onto a monocrystalline (111) platinum substrate. The overlayer aggregation process is studied by imaging of the Ag film morphology as a function of substrate temperature and deposition flux.

In the submonolayer domain at substrate temperatures T between 35 K and 500 K a transition from diffusion limited aggregation to thermodynamic equilibrium of the Ag films is observed. By temperature control the two-dimensional morphologies can be tuned in a very defined way: from randomly distributed adatoms and small clusters, through highly dendritic islands, dense large islands with irregular or smooth boundaries to an equilibrium 2D condensate-gas mixture. By annealing of Ag deposited at T < 50K size-selected clusters with a narrow size distribution are aggregated.

The vapor phase nucleation process is followed on atomic scale between 50K- 130K and dimers are identified as stable nuclei for $T \leq 110K$. The lateral diffusion barrier for Ag adatoms on Pt(111), $E_D = 157 \pm 10$ meV, is determined by quantitative comparison with rate equations from nucleation theory. The Ag-Ag binding energy is estimated to $E_2 = 320 \pm 30$ meV.

A transition from randomly ramified to dendritic fractal growth is observed for $110K \leq T \leq 130K$ by variation of the deposition flux. The microscopic origin of this crossover has been identified to be the anisotropy in step edge diffusion. This anisotropy is either amplified to the mesoscopic cluster shape and trigonal dendrites result, or it is degenerated and randomly ramified fractals occur. The step edge diffusion barriers are estimated by comparison with theoretical growth models.

For T > 620K and coverages Θ < 1 ML the deposition of Ag gives rise to the formation of a two-dimensional surface alloy consisting of Ag-clusters dissolved in the Pt-layer (Θ < 0.5 ML) and Pt-clusters in the Ag-matrix layer (0.5 ML < Θ < 1 ML), respectively. The dissolution of silver into the Pt surface layer and vice versa proceeds from the step edges and is confined to the topmost layer. The embedded clusters have a narrow size distribution centered around 10 Å for Θ < 0.25 ML and Θ > 0.75 ML. In the intermediate coverage range the clusters are arranged in a striped phase.

The first Ag monolayer grows pseudomorphically on Pt(111). The 4.3% misfit strain in the compressed monolayer is relieved in the Ag bilayer by the formation of two weakly incommensurate structures: the metastable striped phase (T < 500K) which converts into a trigonal network of domain walls upon annealing (T > 700K). The third and higher layers exhibit a hexagonal misfit dislocation network resolvable by STM up to 15 ML. After Θ > 25 ML the film structure is relaxed with the natural Ag lattice constant.

In the thermodynamic growth regime (T > 500K) Ag multilayers grow layerwise. At lower temperatures the mass transport between growing layers is hindered, thus the film morphology is determined by kinetics. Two-dimensional growth is observed up to a critical layer number n^* which increases with T from $n^* = 1$ (T = 130K) to $n^* \approx 10$ (T = 300K). The dependence of the interlayer mass transport on the adatom mobility, the size and shape of overlayer islands, and the activation barrier V_e for Ag atoms to step down from a growing island, is investigated for the different n^* ranges.

Table of contents

1. Introduction

Thin film technology is simultaneously one of the oldest arts and one of the newest sciences. The Egyptians appear to have been the earliest practitioners of the art of gold beating and mechanical rolling to produce thin gold leafs for durable ornamentation and protection purposes. Leaf samples dating from the Eighteenth Dynasty (1567 - 1320 BC.) measured 0.3 microns in thickness, thus comparable to the standards used in solid state device fabrication nowadays [Ohr 92].

Improving surface properties by covering the outside of objects with appropriate film layers is conceptually a simple approach. Its technical optimization, however, demands detailed know-how. Since the mechanical and chemical behavior of thin films is a fundamental factor in all kinds of industrial processes, research in this field has a long history. For example, measurements on the stress present in films have been made as early as the end of the nineteenth century [Mil 77].

Today, the development of thin film technologies is mainly triggered by the technological possibilities of quantum semiconductor structures to tailor their electronic and optical properties for specific device applications. Molecular beam epitaxy (MBE) and related nonequilibrium growth techniques have the ability to create superlattices with periodicity of a few atomic layers (see e.g. [Par 85, Cha 85, Her 89]). Such metastable heterostructures possess remarkable properties which cannot be obtained in equilibrium systems, establishing new concepts in the physics of materials.

The phenomenon of epitaxial growth refers to the competition between two crystalline phases. An epitaxial film looses its natural structure by matching the substrate lattice. Since all electronic, optical and magnetic properties of a

1

material depend on its crystalline structure ("function follows form"), the epitaxial strain can be handled as a tool. Designing semiconductor band gaps in a predictable fashion is up to now the most important application of strained layer epitaxy (see e.g. [Hul 90, Pea 90]).

Semiconductor-metal and metal-metal epitaxy became hot topics during recent years. Potential applications such as the purposeful fabrication of new magnetic materials or high T_C-superconducting multilayers have already been realized [Fal 901]. The strong correlation between magnetic properties and morphology of strained two-dimensional iron grown on a W(110) substrate [Elm 94] is an instructive example for the functional modification of metallic overlayers by "epitaxial architecture".

Despite its importance, the knowledge of the nonequilibrium growth techniques involved in the building of artificially structured materials is far from being sufficient. Our understanding of the atomic processes that control growth kinetics is remarkably primitive [Pee 90]. At first glance, this is surprising, since mass transport by diffusion of particles on surfaces is an important step in many other surface phenomena, such as heterogeneous catalysis, phase transitions, segregation and sintering. This inability to describe the formation of atomically engineered materials in a quantitative manner appears even more evident when considering the complex nonlinear coupling of the microscopic processes taking place in growth.

Over the last several years, scanning probe microscopies have advanced to the leading experimental tool in thin film investigations. This is primarily due to their ability to image film morphologies in real space and in a wide lateral range (subnanometer range to several micrometers) with high vertical (≤ 0.01 nm) and lateral resolution (≤ 0.1 nm). In this work scanning tunneling microscopy (STM) [Bin 82] has been applied to study thin metal
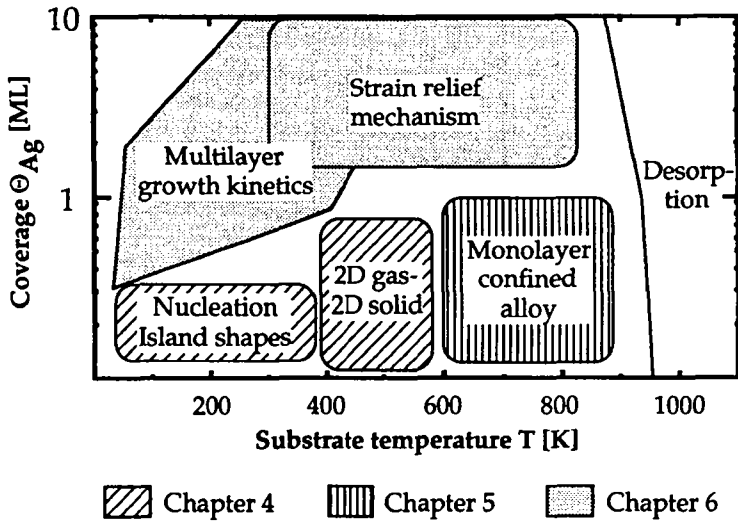
Fig. 1.1: Location of the main issues treated in this thesis displayed in the (Θ,T)-plane of vapor phase growth of Ag on Pt(111).

film growth. In this framework it was enriched by the possibility of measurements at variable substrate temperature in the large range from T = 25K to 800K.

As every thesis must necessarily establish its boundaries, in the present case this task is rather simple: research on one heteroepitaxial model system is presented. The formation of ultrathin Ag films, vapor deposited on the Pt(111) surface has been investigated by means of variable temperature STM. Fig. 1.1 displays the main issues reported in the chapters 4 to 6 covering the results. In chapter 2, general principles and the different atomic motions involved in vapor phase growth are introduced. The third chapter contains experimental details, and furthermore deals with imaging effects. The latter are important for the interpretation of STM topographies presented in Chapter 5 (monolayer confined Ag/Pt alloy surface), and Chapter 6 (strain

relief structures visible on the film surface caused by the structural misfit between Ag and Pt).

The ultimate goal of "epitaxial architecture" is the precise formation of atomically sharp interfaces. In this thesis, the therefore required insight of the atomic motions at the growing interface is obtained by *nanoscale* characterization of the heteroepitaxial system. Because nonequilibrium film morphologies are determined by the microscopic processes involved in growth, it is, on the other hand, possible to learn something about these processes by comparison of structures grown under different growth conditions. A typical example is the measurement of the energetic barrier for an activated process by variation of the temperature.

Once these atomistic quantities are determined, the resulting film morphology can in principle be predicted for certain evaporation conditions and can, by adjusting substrate temperature and deposition rate, i.e. the two external growth parameters in the case of vapor phase growth, also be tuned to almost any morphology desired. The latter is especially demonstrated in chapter 4. By choosing the "proper" condensation kinetics small two-dimensional Ag clusters of defined size (one to several hundred atoms) can be formed in a parallel manner on the Pt substrate. This diffusion-controlled aggregation is a distinctly different approach to build epitaxial "nanostructures" in comparison to techniques which use local probe microscopies to displace atoms on surfaces (see e.g. [Eig 90, Zep 92]). In certain cases, the atom-by-atom manipulation can be replaced by the precise knowledge of the "natural" aggregation process. For future technological applications this concept has the advantage that more than one nanostructure can be built at a time and represents, therefore, a promising tool to tailor epitaxial structures on a nanometer scale.

4

2. Concepts in heteroepitaxial thin film growth

The objective of this chapter is twofold. It serves as general introduction, as well as guideline for the present work. General statements made here are directly related with the behavior observed for Ag growth on Pt(111) facilitating the detailed discussion in the following chapters. In the first section general principles and definitions are introduced and the role of thermodynamics and kinetics in thin film growth is discussed. The essential energetics of film layers is briefly described in the second section. Finally, the last section contains a survey of the microscopic processes involved in heteroepitaxial growth.

2.1 General principles

Epitaxy is a relationship between two crystalline phases, which makes it possible for a crystalline phase "g" (guest) to grow in a structure dependent manner onto a given phase of given structure "h" (host). When the substances of guest and host are the same the phenomenon is called homoepitaxy, and otherwise heteroepitaxy. Such oriented deposits have a long history in mineralogy [Pas 75, Sche 93], but the first systematic study of epitaxy was carried out in 1928 by Royer [Roy 28] using X-ray diffraction. He also introduced the name epitaxy (from the Greek "επι – ταξισ" meaning "on" - "arrangement") for this phenomenon. The most important result of his studies -the geometrical approach for the understanding of epitaxy- has remained prominent up to present days. Oriented growth occurs only if it involves two crystalline lattice planes that have networks of identical or quasi-identical symmetry and of closely similar lattice constants. Thus forming an epitaxial guest lattice different from its "natural" crystalline

structure requires a well adapted host phase. The degree to which the two lattices match or not is the key parameter in the realization of epitaxy.

Epitaxial host-guest relationships occur frequently by the formation of solid layers on single crystalline substrates either by electrochemical deposition from solutions, or from melts, or from gas-phase deposits. In this thesis, vapor phase deposition of thin epitaxial films is investigated using an almost perfect single crystalline surface as host phase. The physical concepts to describe thin film formation are closely related to the more general subject of crystal growth (see e.g. [Har 73, Bar 79, Hur 93]). Indeed, also a three-dimensional crystal grows at his two-dimensional interface to the environment by attachment of atoms to the crystal surface. Thus, surface and interface properties play an essential role in this field.

It was Kossel in 1927, who first analyzed the atomic inhomogeneity of a crystal surface and emphasized the fundamental importance to the growth process of atomic steps and kinks [Kos 27]. In 1949, Burton, Cabrera and Frank showed that crystal dislocations were capable of providing the sources of steps required for the continuous growth of a crystal even at low vapor supersaturation [Bur 49]. A theoretical estimation of the crystal growth-rate under the assumption of homogeneous vapor phase nucleation [Vol 26, Bec 35] exceeded the experimental value by a factor of e^{3600} ! Thus the up to that time used approximation of perfect crystals which grow had to be dropped. This recognition lead to a theory of growth of real crystals [Bur 51] which is the nowadays base of an atomistic understanding of crystal growth [Gil 63].

Thin film growth, by definition, is a dynamic phenomenon. The consideration of thermodynamics as well as kinetics is therefore essential. While thermodynamics embodies the essence of the behavior of the physical system at equilibrium, the kinetics controls the ability of the system

6

i

to move towards the equilibrium state within the given conditions. The phenomena in vapor phase growth on solid substrates range from "practically" equilibrium on the one hand to "practically" nonequilibrium on the other, as revealed in many studies of growing films (see e.g. [Ker 79, Mer 84, Ven 84, Lag 90]). The microscopic processes involved in growth are thermally activated. Their equilibration time may accordingly be anywhere between real short and real long on the appropriate time scale, depending strongly on the substrate temperature T. Consequently, a distinction between an equilibrium and a kinetic growth form is not always possible.

In fact, the equilibrium state of the entire system, the substrate, the growing film and the vapor is not possible. For growth to occur, a driving force for attachment of vapor species to the solid surface at a rate higher than the rate of loss due to evaporation must exist, implying departure from global equilibrium. The degree of vapor supersaturation ζ is defined as the ratio of deposition rate R to the rate of evaporation. The sticking coefficient of metals on metallic substrates is nearly one in the substrate temperature range of interest. As a consequence, ζ values of the order 10^{20} are reached for typical growth rates. But distinction needs to be made between global, partial and local equilibrium [Mad 83]. Even if the equilibrium state of the entire system is not realized, partial equilibrium between the substrate and the growing film may be established. Furthermore, on a local spatial scale the use of equilibrium thermodynamics, specifically the minimum free energy criteria, may be a valid approach to describe kinetically determined film structures [Mer 84].

2.2 Energetics of epitaxial films

2.2.1 Strain in epitaxial overlayers

Atoms adsorbed on crystal surfaces often form ordered structures. Adsorbate patterns and their phase transitions are a well-developed theoretical topic (see e.g. [Das 75, Bak 82, Per 92]). Their symmetry and stability depend on the adsorbate-substrate potential energy and the lateral adsorbate-adsorbate interaction. These two elements are already included in the simple Frenkel-Kontorova (FK) model [Fre 38] of a one-dimensional solid on a rigid substrate (see Fig. 2.1).

A chain of atoms connected by harmonic springs is brought in contact with a sinusoidal potential (periodicity a, amplitude V). The equilibrium separation of atoms in the chain is b and the strength of the harmonic restoring forces between them is measured by κ. The total energy of the system is given by the following Hamiltonian [Fra 491]:

$$H = \sum_n \left[\kappa \, (x_{n+1} - x_n - b)^2 + V \, (1 - \cos\frac{2\pi}{a} x_n) \right]$$

where x_n is the absolute position of the nth atom. The problem contains three parameters: the misfit $f = \frac{b-a}{a}$ and the two constants κ and V. Their relation determines the ground state atomic arrangement. For fixed misfit f there are two limiting cases:

- When the spring constant κ is large and the corrugation V of the substrate adhesion is small, the springs dominate and the chain retains its natural lattice constant b. This is the incommensurate (I) state sketched in Fig. 2.1 a).
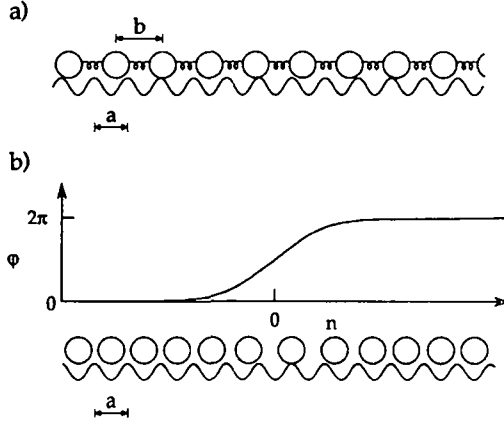
Fig. 2.1: a) One-dimensional Frenkel - Kontorova (FK) model. An array of atoms connected with harmonic springs with an equilibrium "lattice constant" b interacts with a substrate potential of periodicity a.
b) Single domain wall solution of the FK model and the corresponding atomic displacements. Over the length of the domain wall (centered at n = 0) one atom is missing with respect to a commensurate layer (a), b) from [Bak 82]).

• In the reverse case, i.e. for weak lateral interaction, the second energy term in H dominates and the chain atoms "lock-in" the potential valleys. This is the commensurate (C) state. Due to the small κ the deformation of the chain plays a negligible role in energetics.

In the intermediate case, an energetic competition takes place between the elastic energy to strain the overlayer and the "lock-in" energy which is minimized when all chain atoms are in registry with the substrate. For comparable spring and adhesive forces the outcome is a weakly incommensurate phase. The displacement pattern is analytically calculable in the continuum limit, i.e. by introducing the phase φ_n by $x_n = na + \frac{a}{2\pi}\varphi_n$ and setting $\varphi_n - \varphi_{n-1} = d\varphi/dn$. Minimization of the corresponding

Hamiltonian yields a non-linear differential equation exhibiting many solutions. Apart from the trivial C and I state also a soliton solution emerges describing a wall which separates two commensurate regions. More general solutions contain a periodic array of such domain walls [Bak 82].

Fig 2.1 b) shows the function $\varphi(n)$ for one soliton centered at n = 0 and illustrates the atomic displacement for positive misfit (b > a). Within the wall the adsorbate bonds are stretched while in the surrounding regions the layer is compressed to match the substrate. This compromise between "lock-in" and elastic energy represents an elegant way to relieve strain while sacrificing only a small amount of substrate adhesion. Since atoms are missing (or inserted for misfit f < 0) along the domain walls, the name misfit dislocation (MD) is used in the context of thin film epitaxy.

At fixed κ and V the variation of f leads to the following relations: small misfit favors the C state while a large difference between the "lattice constants" a and b favors the I state. It exists a critical misfit $f_c \propto \sqrt{V/\kappa}$ above which the coherently matched C state becomes unstable [Fra 492, Ker 88]. The concept of MD's plays a central role for the transition between C and I state. When the distance l between MD's is large, the total energy E can be written in the form:

$$E = \frac{A}{l}(f_c - f) + \frac{B}{l}\exp(-\frac{l}{l_0})$$

where A, B, l_0 are positive constants [Bak 76, Zan 91]. The MD density $\frac{1}{l}$ is connected to the average separation $\bar{b}$ between adjacent atoms through the equation: $\frac{1}{l} = \frac{\bar{b} - a}{a}$.

The first term in E can be regarded as an individual MD energy and the second one as an exponentially decaying repulsive interaction between the walls. When E is minimized with respect to l (the remaining free

parameter), then the C-I transition can be seen in the following way: for $f <$ f_c, both terms in E are positive and the minimum corresponds to $l \rightarrow \infty$, i.e. no MD's and the chain is in registry. For $f > f_c$ only the first term becomes negative and the sum has its minimum at finite l. The equilibrium MD-density is therefore a compromise between the energy gain of MD creation and the energy cost due the MD repulsion.

The FK-model is a rough approximation of the energetics of an epitaxial monolayer. The forces to stretch (compress) atomic bonds have anharmonic contributions, the substrate is not perfectly rigid and chemical bonding considerations are completely neglected in the model. The latter is for metallic cohesion of secondary importance due to the delocalized nature of metallic bonds. Improvements to and generalization of the above analysis enable a more realistic modeling of misfit accommodation in thin film epitaxy (see e.g. [Mat 751, Mer 75, Hul 90, Zan 91]). It comes out that the basic results of the FK-model remain valid.

When a critical misfit f_c is exceeded, equilibrium requires the misfit accommodation to be shared between homogeneous film strain and the introduction of misfit dislocations. This is illustrated in Fig 2.2 a) where the lattice energy of the film-substrate interface is qualitatively plotted as a function of misfit. The curves refer to the two extreme cases: first, only dislocations are used to adjust the film lattice on the substrate; second, the pseudomorphic case, where the film is coherently strained to continue the stacking sequence of the substrate. Pseudomorphy is only the ground state for $f < f_c$, i.e. below the crossing point of the two curves.

The structural misfit between the face-centered-cubic (fcc) metals silver and platinum is +4.3% (lattice constants at T = 300K: a_{Pt} = 3.92Å, a_{Ag} = 4.09Å). Ag monolayers on the Pt(111) surface form a pseudomorphic structure, as

11
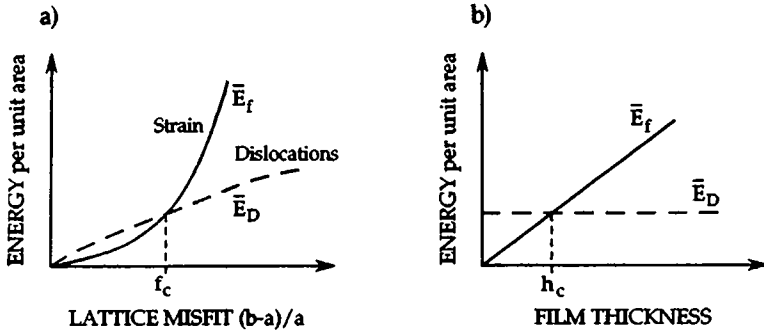
Fig. 2.2: a), b) Qualitative plots of lattice energy stored at the heteroepitaxial interface per unit area as a function of misfit in a) and film thickness in b). The dashed lines show the energy by adjustment of the film and substrate lattices by dislocations, while the full lines are valid for a homogeneously strained film (from [Lüt 93]).

revealed by STM in the present work, as well as by structural characterization with low-energy electron diffraction (LEED) [Schm 89, Här 93] and by a recent investigation using photoelectron forward scattering [Ran 94]. The coherent matching of the Ag monolayer corresponds to a compression by 8.3% of its atomic density with respect to a bulk Ag(111) plane. To stabilize this two-dimensional lattice the Ag-Pt bonding has to be stronger than the lateral Ag-Ag interaction or, in other words, the critical misfit f_c is larger than 4.3%.

For a given film-substrate pair, all energetic and structural parameters are fixed and the remaining question is what happens when the film grows in height. The simplest answer incorporates the two-dimensional FK-result by making the following replacement: $\kappa \rightarrow \kappa h$, i.e. it is assumed that the overlayer stiffness increases linearly with the film thickness h [Zan 91]. Using the dependence $f_c \propto \sqrt{V/\kappa}$ it follows $f_c \propto \sqrt{1/h}$ and one expects a critical thickness h_c, above which a coherently strained film is no longer the ground state.

12

Although the above derivation is scanty, the result is in principle right, as shown in Fig. 2.2 b). The elastic energy required to match homogeneously the substrate is nearly proportional to the number of strained bonds. Thus, the lattice energy $\overline{E}_f$ of a coherently strained film increases linearly with h. The film adjustment by dislocations is to first order independent of h, since thicker films are no more stressed than thin ones. Thus, the energy $\overline{E}_D(h)$ can be approximated by a straight line crossing the pseudomorphic energy $\overline{E}_f$ at the critical height h_c.

Quantitatively, the equilibrium theory of strained films is hardly verified in real heteroepitaxial systems [Hul 90, Zan 91, Ter 942]. Structural defects present on the substrate will propagate upward with the growing film leading to relaxation by threading dislocations. If their density is low, the growth of unrelaxed structures far beyond the critical thickness is possible. This can be explained by the slow nucleation kinetics of misfit dislocations. The large biaxial strain of these metastable structures plays an important role in strained-layer devices [Pea 90, Pee 90].

2.2.2 Thermodynamic growth modes

The phenomenon by which thin films grow in different modes was first addressed by Bauer [Bau 58]. He pointed out that three main growth modes are obtained under quasi-equilibrium growth conditions. By using solely thermodynamic parameters his characterization of film morphologies focuses on the essential energetics: the work to create surfaces and interfaces. This advantage of the model is at the same time its disadvantage, as will be discussed below.

One way to derive the growth modes is the analysis of the wetting behavior of a cap-shaped drop, as sketched in Fig 2.3 d). The contact angle ϕ depends on the tensions γ_s, γ_f, and γ_i, i.e. the characteristic free energies per unit

13
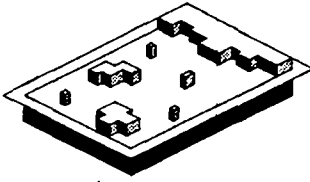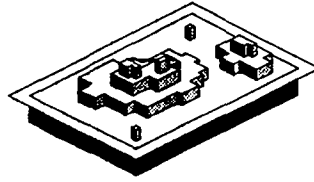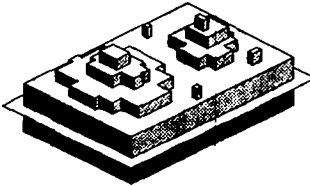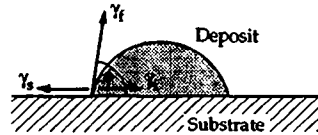
Fig. 2.3: a)-c) Schematic representation of the three thermodynamic growth modes. Two-dimensional growth in a), three-dimensional growth in b) and the hybrid case of three-dimensional "islanding" after layer-by-layer growth of one or several monolayer(s) in c) (from [Pee 90]).
d) Simplified picture of a cap-shaped island showing the directions of the surface and interface tensions γ_s, γ_f, and γ_i (from [Lüt 93]).

area to create an additional piece of surface, film and interface, respectively [Gen 85]. Since the γ's can also be interpreted as a force per unit length, force equilibrium at the point where substrate and deposit touch requires: $\gamma_s = \gamma_i + \gamma_f \cos\phi$ [You 05]. Complete wetting is achieved for $\phi = 0$, thus the following condition has to be fulfilled:

$$\gamma_s \geq \gamma_f + \gamma_i \quad \Leftrightarrow \quad (\gamma_f + \gamma_i - \gamma_s) = \Delta\gamma \leq 0$$

The minimum free energy configuration of a film as a function of height can be deduced by using this wetting condition **for each adlayer n** [Bau 86] by setting $\gamma_{fn} + \gamma_{in} - \gamma_s = \Delta\gamma_n \leq 0$, where γ_s remains the surface energy of the

14

substrate, γ_{fn} is the layer-dependent surface energy of the film and γ_{in} the interfacial energy between two successive layers. A sign change of $\Delta\gamma_n(n)$ at the critical layer number n* indicates the transition from a smooth 2D- to a rough 3D-film morphology.

In Fig. 2.3 a), b) the degenerated cases n* = 0 and n* = ∞ are illustrated. The corresponding Volmer-Weber (VW) [Vol 26] and Frank-van der Merve (FM) growth modes [Fra 492] describe 3D-islands on the bare substrate and smooth stacking of an infinite thick film, respectively. The hybrid case of a finite n* is shown in Fig. 2.3 c). In this case, for n > n*, the film bulls up into 3D-islands after the formation of smooth wetting layers up to n = n*. Historically, this Stranski-Krastanov (SK) growth mechanism has been first calculated for a monovalent ionic crystal (M^+X^-) onto a divalent $(M^{2+}X^{2-})$ substrate [Stra 38], where the initial formation of a monolayer is followed by the condensation of two ions high nuclei.

The SK-growth mode is associated to an energetic instability occurring at finite film height. Apart from the layer dependence of the misfit accommodation another possibility is given by a symmetry break of the film structure. A currently statement found in the literature is that the transition from pseudomorphy to dislocation formation coincides with the critical height n* coming out from the layer-dependent wetting condition (see e.g. [Mat 752, Ber 88, Gen 92]). This point justifies reliable quantification [Mer 94]. One problem in this context is the use of the word "growth mode" causing sometimes unclearness. Although defined by the above thermodynamic conditions, "growth mode" is often used in a different way by describing the fact that a system grows like the FM-, VW- or SK-morphology (under certain nonequilibrium growth conditions).

Nevertheless, the misfit accommodation is clearly a driving force for a sign change of $\Delta\gamma_n$. The sum $\gamma_{fn} + \gamma_{in}$ contains a chemical and a structural component. A pseudomorphic growth of the first wetting layers results in a positive strain energy contribution which increases with n. The negative adhesion contribution due to the substrate influence decreases with n. Finally, at the critical layer number n^* the wetting condition can not be fulfilled any longer, i.e. $\gamma_{fn} + \gamma_{in} \geq \gamma_s$, for $n > n^*$. In principle, the above argumentation is nothing else than the derivation of the critical thickness h_c in 2.2.1, but here in the formulation of surface and interface tensions. The film can not form up to an infinite thickness a coherently strained surface.

One solution for the energetic instability is the introduction of misfit dislocations. The growth mode criterion, on the other hand, suggests the collection of subsequent deposited material into "strain-free" 3D-islands to reduce surface and interface area. Both situations are observed in the experiments. The apparent conflict is a problem of the growth mode model to describe quantitatively the SK growth mode. In fact, the n-dependent wetting condition is rigorously only valid in the homoepitaxial case or for zero misfit [Bau 86]. Using surface and interface energies to predict the film instability requires a clear separation of the different energetic contributions to γ_{fn} and γ_{in}, as recently pointed out by Raeker et al. [Rae 94].

Although the growth modes are well defined, they are based on the fact that macroscopic properties (surface, interface energies) are attributed to microscopic systems (down to one atomic layer !). Thus, the theory deals with rather poor available quantities not directly related to measurable parameters. This type of statement can already be found in Kossel's theory of crystal growth written in 1927 [Kos 27]:

L

"Man bemerkt ferner, wenn man sich die Molekularvorgänge beim Wachstum näher vorzustellen sucht, daß der Begriff der Oberflächenenergie gegenüber all dem, was hier im Einzelnen vor sich gehen muß, allzu grob ist"

The surface energy relation of Ag(111) and Pt(111) is $\gamma_{Pt(111)} = 1.06 \gg \gamma_{Ag(111)}$ = 0.56 eV/atom [Mie 78]. By assuming $\gamma_{fn} \approx \gamma_{Ag(111)}$ and a small influence of γ_{in} (factor 2 between γ_f and γ_s) one expects the FM-growth mode. Indeed, for substrate temperatures T > 500K a smooth Ag film forms on Pt(111). Furthermore, a 25 layer thick film is completely relaxed to the bulk lattice of Ag, as revealed by He-diffraction measurements [Rom 94]. Thus, the 4.3% strain in this heteroepitaxial system can be relieved without formation of 3D-islands. This result is in disagreement with thermodynamic film models predicting for non-zero misfit always film instability [Bru 87, Gra 88].

2.3 Atomistic processes

Thermodynamic considerations are independent of the question **how** an epitaxial film is formed. In the kinetic growth regime, however, the film formation has to be seen as a sequence of atomistic processes where the outcome depends strongly on the particular way taken by the randomly deposited atoms. Thus, predictions require detailed knowledge of the microscopic processes relevant in vapor phase growth. The most important processes are sketched in Fig. 2.4 a) and their essential properties are discussed in this section.

The arriving film atom dissipates its heat of condensation E_A to the solid through one or a series of inelastic collisions. Once bound at the surface its motion will be governed by the corrugation of the binding potential (see Fig. 2.4 b)), as well as by its interaction with the other adsorbed film atoms. The
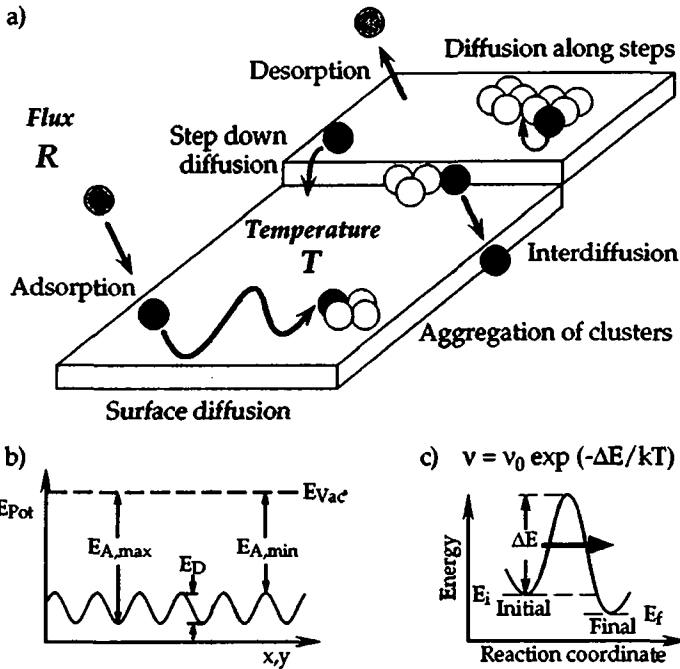
Fig. 2.4: a) Overview of atomistic processes taking place during vapor phase growth of a thin film. The external controlled parameters are the deposition flux R and the substrate temperature T.
b) Potential energy of a particle during adsorption. The ratio between diffusion barrier E_D and adsorption energy E_A is about 1/10 to 1/20.
c) Energy diagram of a thermally activated process and the corresponding transition rate v.

latter leads to coupling of the individual "growth trajectories" and ordering of the adsorbate becomes possible. In this microscopic view, also defects, like atomic steps participate in the growth scenario in the same way as each deposited atom. The ordering kinetics is influenced by two external controlled parameters marked in Fig. 2.4 a): the substrate temperature T and the deposition flux R.

18

Since all atomic displacements on the substrate are thermally activated processes, the influence of T is most pronounced. The transition rate v between two atomic states separated by an energy barrier ΔE depends exponentially on T, as sketched in Fig. 2.4 c). Quantitatively, this dependence is derived from the "transition state theory" [Gla 41] which is a good approximation for all dynamic processes on surfaces (see e.g. [Lew 78, Hen 91]). The transition rate v between initial and final state is proportional to the probability to obtain the energy $E_i + \Delta E$ of the transition state and hence proportional to a Boltzmann-factor $\exp(-\Delta E/kT)$. The proportionality constant v_0 can be interpreted as the number of attempts per unit time that the system tries to overcome the barrier ΔE. The order of magnitude for v_0 is given by the universal factor kT/h (= $2x10^{10}$ [(sK)$^{-1}$] T) entering usually in the calculations of these processes (see e.g. [Chr 75, Wah 90]). Thus, the attempt frequency v_0 corresponds to the typical frequency of lattice vibrations ($\approx 10^{12}$-10^{13} Hz) and its T-dependence is usually negligible regarding the Boltzmann-factor.

The average time between two deposition events (on a certain surface area) is given by the deposition flux R. Thus, the appropriate time scale (with respect to the atomic mobility) for modeling nonequilibrium morphologies is set by the flux R which enters as important parameter in kinetic growth theories (see e.g. [Kas 77, Lew 78, Sto 81, Ven 84]). Input parameters in such an analysis are e.g. the energetic barriers, binding energies of clusters, etc. or simply the probabilities of certain hopping events (Monte Carlo methods).

Unfortunately, these calculations require the knowledge of a large number of kinetic parameters which are normally not available. In view of a quantitative comparison with experiments, the important point is therefore the reduction of complexity. Experimentally, one tries therefore to vary the developing film structure (density, size and shape of adlayer islands) in such

19

a way that differences (as a function of the external growth parameters) are ideally caused by one or by only few of the microscopic processes.

In the following, a brief survey of the essential dynamic processes is given in view of application to Ag growth kinetics on Pt(111).

2.3.1 Surface diffusion

An adatom migrates along the surface by overcoming the activation barrier E_D at the saddle points between neighboring sites ($E_i = E_f$ on a flat surface). This hopping image is valid for $kT \ll E_D$, which means that the residence time spent at the adsorption site is long compared with the time spent in the transition state. This situation is in analogy to the two-dimensional random walk where a particle on a discrete lattice has equal probability to hop to neighboring sites. For $kT \gg E_D$ no energetic barrier hinders the lateral displacements of atoms and the adsorbate structure can be described e.g. by a 2D-gas equation.

The first quantitative theory of diffusion has been developed in the context of Brownian motion [Ein 05, Smo 06]. Experimentally, a microscopic view of diffusion has become possible since 1937 by Müller's invention of the field emission microscope (FEM) [Mül 37]. Using the later developed field ion microscope (FIM) [Mül 51] Ehrlich and Hubba carried out the first systematic study of atomic diffusion in the sixties [Ehr 661].

FIM provides information about the location of individual adatoms and is therefore the ideal method to verify the basic laws of diffusion by statistical analysis of atomic displacements [Ehr 662]. The FIM image is formed from a sharp tip by ionization of neutral gas atoms in the presence of the high electric field (≈ 4 V/Å) in the vicinity of the tip. Although restricted to small substrates (a few hundred lattice sites) much information about microscopic processes relevant in crystal growth has been obtained by this method (see

20

e.g. [Ehr 84]). Due to the relatively low adsorption energy E_A of Ag on Pt(111) ($\approx$ 3 eV) a FIM-study of this system is not possible. The high imaging field requires a minimum adsorption energy ($\geq$ 4 eV) to avoid field desorption.

The classical Einstein-relation $\langle \Delta x^2 \rangle = 2Dt$ describes well the statistics of the motion of single metal atoms on metallic substrates [Ehr 91]. The mean square displacement $\langle \Delta x^2 \rangle$ along one coordinate is proportional to the diffusion time interval t and the diffusivity D (entering as material constant in Fick's law of macroscopic diffusion). The connection with the energetic corrugation of the substrate is given by the Arrhenius-behavior $D = D_0 \exp(-E_D/kT)$ where D_0 is the preexponential factor. Under the assumption of uncorrelated hops and negligible entropy of activation, the following relation is valid: $D_0 = v_0 \, l^2/4$, where l is the distance between two adsorption sites (jump length) and v_0 the above introduced attempt frequency. D_0 should be on the order of 10^{-3} cm^2/s for typical values $l \approx 3$Å and $v_0 \approx 10^{13}$ Hz. Deviation from this behavior indicates a diffusion mechanism which is not adequately described by the random walk model.

Fig. 2.5 a) illustrates the lattice symmetry of the Pt(111) surface. The bulk stacking is continued by adsorption on a fcc- or bulk-site and is therefore the expected adsorption site for Ag. Calculations for Ag/Pt(111) indicate indeed a small energetic difference between the fcc- and hcp-site in favor to a slightly stronger binding of an Ag atom in fcc-geometry [Bla 92, Fei 941]. For Ir on Ir(111) the hcp- or surface-site is favored (E_{fcc} - E_{hcp} $\approx$ 0.04 eV) [Wan 911]; calculations for Al/Al(111) predict also an energetically preferred hcp-site (E_{fcc} - E_{hcp} = 0.04 eV) [Stu 941, Stu 942]. Consequently, the bulk structure seems to play only a minor role for the energetics of a single adsorbed atom. FIM results of Ir$_x$-clusters on Ir(111) confirm this picture. Although E_{hcp} < E_{fcc} for single Ir adatoms, it has been found that atoms in a cluster prefer to

21

a)   b)
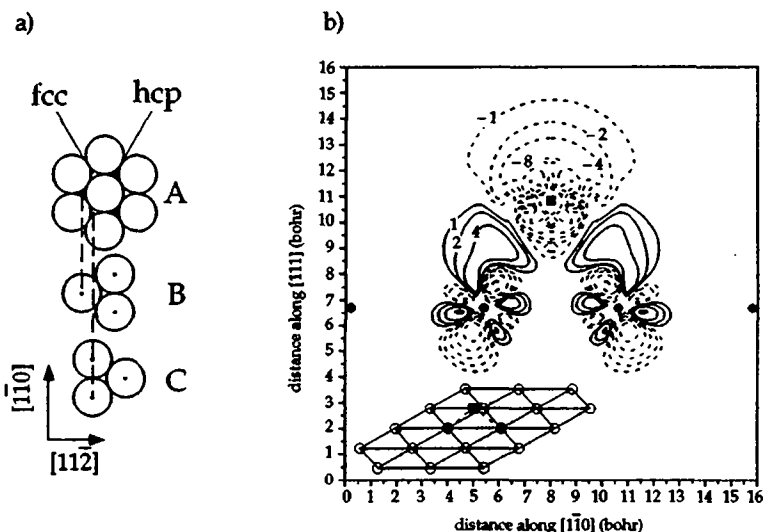
Fig. 2.5: a) Hexagonal symmetry of the (111) face of a face-centered-cubic (fcc) crystal. The indicated ABC stacking sequence of subsequent (111) planes produces two types of threefold hollow site labeled fcc and hcp. Below the hcp site, an atom of the second layer is situated as in the hexagonal-close-packed (hcp) lattice having AB stacking sequence of subsequent (0001) planes.

b) Transition state for Ag diffusion on Pt(111). The image shows the bond charge density for optimal Ag adsorption in a two-fold bridge site on Pt(111), as calculated by first principles calculations. Contour labels are in units of 10^{-3} e/bohr^3. Solid contours represent an increase in electron density and dashed contours correspond to a decrease relative to the sum of clean surface and isolated Pt atom pseudocharges. Details in text (from [Fei 941]).

occupy fcc-sites if the cluster size increases to x ≈ 7, i.e. when the adsorbate approaches the bulk structure [Wan 89].

First principles (FP) calculations predict the Ag adsorption energy on a twofold bridge site 0.20 eV higher than on a fcc/hcp-site [Fei 941]. Thus, for hopping to the adjacent threefold hollow site an Ag atom has to overcome the energetic barrier $E_D = 0.20$ eV. A calculation by means of the embedded

atom method (EAM) [Daw 83, Daw 93] resulted in a static barrier of $E_D = 0.051$ eV, a molecular dynamics simulation with EAM potentials gave a dynamic barrier of $E_D = 0.058$ eV [Bla 92, Mas 931]. The experimental value derived in this work is $E_D = 0.157 \pm 0.01$ eV.

The difference of the EAM-values to the FP- and experimental values can qualitatively be understood based on the following arguments [Fei 941, Fei 942]. The EAM picture of metallic bonding is that each atom is embedded in a host electron gas created by its neighboring atoms. The total energy of the system is therefore mainly approximated by focusing on the many-atom aspects of bonding (see also [Nør 93]) leading to the computational efficiency of the EAM. Ag and Pt are reliably described by the EAM since they do not tend to bond directionally because their valence d-shells are nearly full.

The application of the EAM to surface problems, however, leads systematically to lower calculated energies due to the lower coordination of surface atoms, without affecting the qualitative agreement between relative values with experiments [Daw 93]. In the case of Ag adsorption on Pt the directional bonding effects which are not countenanced by the EAM can be seen in Fig 2.5 b) in form of the built-up of electron density in the middle of each Ag-Pt bond [Fei 941]. The FP calculations, on the other hand, predict a more corrugated Ag/Pt(111) potential with respect to the experimental values, thus in the same way as observed for Pt/Pt(111) ($E_D^{exp} = 0.25$ eV $< E_D^{FP} = 0.38$ eV) [Fei 942].

2.2.2 Adsorption and "transient mobility"

The fundamental question concerning the adsorption process itself is how a condensing atom gives up its considerable heat of condensation to the surface lattice. For example: it has been reported for Xe adsorption on Pt(111) at T = 4K that impinging atoms can scatter hundreds of angstroms across the

surface to reach step edges as preferred adsorption sites, although their diffusion should be frozen [Wei 92, Abr 94]. The observed effect has been attributed to "transient mobility", i.e. the idea that after impact a fraction of the adsorption energy E_A is converted in kinetic energy to skip across the surface. Due to the large difference between E_A and E_D and the unknown efficiency of the energy transfer to the surface, transient mobility effects appear physically reasonable.

Concerning the condensation process for chemisorbed metal atoms on metallic substrates contradictory results have been obtained. Transient mobility has been attributed to cause low temperature quasi layer-by-layer growth of several metals on Cu(100) and Ag(100) surfaces [Ege 89]. FIM results [Wan 911] and molecular dynamics simulations [San 911, Lor 93], however, indicate that the energy transfer at the first point of impact is efficient and the deposited atom is rapidly localized. Also for Ag growth on Pt(111) no indication of transient mobility, i.e clustering at very low temperatures, has been observed (see 4.2.1).

2.3.3 Aggregation of clusters

In the classical capillary model of thin film nucleation (see e.g. [Neu 70, Lüt 93]) positive fluctuations of the free-energy are required to form stable aggregates on the surface. Using the thermodynamic liquid-drop model the free energy of an aggregate goes through a maximum as it grows through its "critical" size. The latter arises from the different size-dependencies of the volume- and surface-energy term for small drops. To avoid the dissociation into the vapor phase a vapor supersaturation greater than unity is therefore required to overcome this condensation barrier ("nucleation work").

It was Walton, who first recognized that under usual growth conditions the size of the critical nucleus is very small (a few atoms) [Wal 62]. The critical
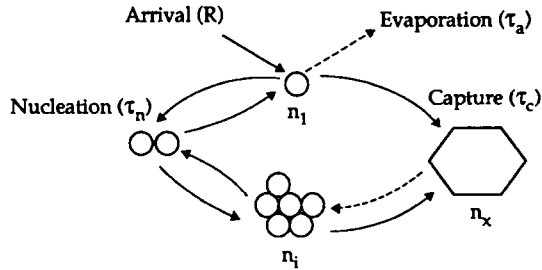
Fig. 2.6: Illustration of the interaction between different cluster population n_j in the early stages of film growth. The adatom concentration n_1 determines the density of critical clusters (n_i) and of stable nuclei (n_x). Decreasing of n_1 happens with the time constants of nucleation (τ_n), evaporation (τ_a) and the capture rate (τ_c) of stable nuclei. This loss is compensated by the deposition flux R. The two dotted lines indicate the processes which are less important for low temperatures, i.e. the desorption of adatoms and the decay of stable clusters (from [Ven 86]).

size i is thereby defined as the largest unstable cluster size, i.e. only clusters with sizes j > i have a higher probability to grow than to decay. In atomistic nucleation theories the building of critical and subsequent stable nuclei proceeds by the statistically encounter of diffusing atoms and clusters on the substrate [Zin 66, Lew 67, Ven 73].

Fig. 2.6 is an illustration how the different cluster populations which are present on the surface can interact. Nucleation of critical, and growth of stable clusters are competing processes since both reduce the single adatom density n_1. With increasing deposition time adatoms are predominantly captured by stable clusters which cover finally the whole substrate. Nucleation theories predict the saturated nucleation density $n_x(R,T)$ as a function of the external growth parameters (see e.g. [Lew 78, Ven 84]).
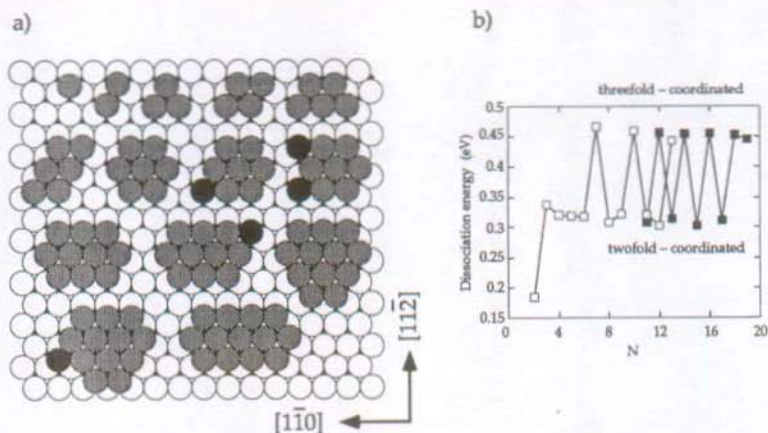
25

a)   b)

Fig. 2.7:   a) Possible structures of two-dimensional clusters up to the size n = 13 on the (111) surface of a fcc crystal. Atoms with an in-plane coordination number of two have been marked for cluster sizes n >7. First row: n = 1 to 5; second row: n = 6 to 9, with the heptamer being the smallest size where at least all the atoms are threefold-coordinated; third row: n = 10 to 12, with n = 12 in a concentric arrangement avoiding twofold-coordinated atoms in its elongated shape; fourth row: n = 13 is the reverse case to n = 12. Here the concentric shell structure leads to the lower dissociation energy due to the twofold-coordinated border atom.

b) Dissociation energy (E_n-E_{n-1}-E_1) of Ag_n clusters on Pt(111) calculated with the embedded atom method. The theory predicts a stability gap of about 0.13 eV between symmetric clusters and arrangements with twofold-coordinated atoms. The open squares refer to elongated structures and filled squares to concentric shell structures (from [Mas 931]).

Comparison with experiments requires the knowledge of the critical cluster size i, its binding energy E_i, the adatom diffusivity D (clusters are usually assumed to be immobile), and the time constant of evaporation τ_a. The function n_x(R,T) depends strongly on the critical cluster size i since the probability to produce statistically a certain cluster type changes dramatically

with the number of atoms involved. With increasing temperature T the critical size i increases due to thermal dissociation of clusters, explaining the $n_x(R,T)$ dependence on the cluster binding energy E_i.

Fig. 2.7 shows in a) some possible geometric structures of two-dimensional Ag clusters on Pt(111) and in b) the calculated dissociation energies as a function of cluster size [Mas 93]. Closed two-dimensional shells ("magic clusters") give rise to a particular stability at certain sizes (n = 7, 10, 12, etc.). This is the signature of the alternation between structures in which every atom has at least three nearest neighbors and structures with one or two atoms twofold coordinated. The simple correlation between the dissociation energy and the coordination of border atoms has been confirmed by calculations of Ni clusters on Ni(111) [Liu 92, Liu 93, Mas 932] and Pt clusters on Pt(111) [Nør 93]. FIM measurements of the dissociation temperature of Ir_x-clusters on Ir(111) show a less pronounced stability effect for the heptamer [Wan 90].

2.3.4 Step down diffusion

Every real substrate contains steps and the adsorption potential near a monatomic step controls the "step-adatom" interaction. The detailed form of the potential governs the mass transport between growing layers. An adatom adsorbed close to the up- or down-side of a step will have a different probability of moving into the step edge position [Schw 66]. Thus, in general, the step potential has an asymmetric form as shown in the upper picture of Fig. 2.8 a). One lattice site away from an ascending step the atom will "feel" the higher coordination at the step edge, while close to a descending step an additional barrier V_e ("Schwoebel"-barrier) may be present expressing the lower coordination during a "jump down" process.
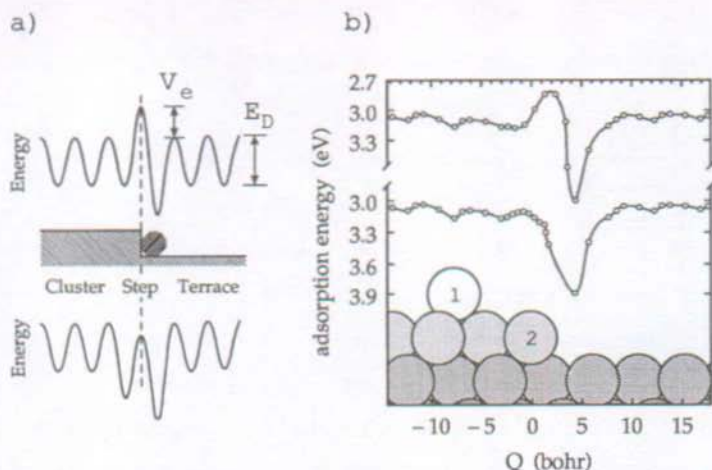
27

Fig. 2.8: a) Classical view of the potential at a step (upper curve) and the potential consistent with FIM measurements (lower curve) of Ir diffusion on Ir(111) (performed with an Ir cluster on top of the tip) (from [Wan 912]).

b): Density-functional calculation of adsorption energy along the diffusion path of an Al adatom crossing a B-type step on Al(111). The generalized coordinate Q is $X_1 + X_2$ where X_1 and X_2 are the x coordinates of the atoms labeled 1 and 2, respectively. The x axis is parallel to the surface and perpendicular to the step orientation. The upper curve is calculated for a "roll over" process of atom 1, while the lower one shows the E(Q)-dependence for the exchange process, i.e. atom 1 takes the position of atom 2 and pushes the former one forward (from [Stu 941]).

The lower potential in a) is consistent with FIM measurements of Ir incorporation at descending steps of Ir clusters [Wan 912]. For larger clusters even a trapping of the Ir atom at the descending step rather than a reflection due to a barrier V_e has been found. The conditions for incorporation depend quite sensitively to the local atomic arrangement and the "jump down" mechanism may involve an exchange process with the step atoms as revealed for W incorporation in descending Ir steps [Wan 912]. The latter is

illustrated in b) showing calculations of the step potential for Al/Al(111) [Stu 941, Stu 942]. The theory predicts that an Al adatom has to pass a considerably higher barrier, V_e, to descend the step by using the classical "roll over" path than by an exchange process.

In recent FIM studies it has been found that the "active" region of the step potential is not restricted to the two lattice sites on both sides of the step edge [Wan 932, Wan 931]. Ir growth on an Ir(111) surface with a central iridium cluster adsorbed on it results in a depleted zone around the cluster. Atoms deposited two sites apart from the ascending cluster step are trapped even at $T \approx 20K$ where diffusion on the terrace is frozen in. Thus, the effective "capture radius" of a cluster is increased by the width of this empty zone.

2.3.5 Diffusion along step edges

One interesting aspect of fcc (111) surfaces is that there are two types of close-packed step orientations, as shown in Fig. 2.9 a). Due to their different atomic structure one expects a different diffusivity along A- and B-steps. An atom adsorbed at the step is trapped in the potential minimum of the ascending step as described in 2.3.4. Its diffusion is therefore restricted to a one-dimensional random walk parallel to the step as illustrated in b). At a kink site an atom increases its in-plane coordination by one bond, i.e. kinks act as sinks for diffusing step atoms (as long as T is low enough that kink dissociation is forbidden). The second possibility for a one-dimensional condensation event is the encounter of two diffusing atoms at the step. By this way a kink - anti-kink pair has nucleated and the step grows perpendicular to its orientation.
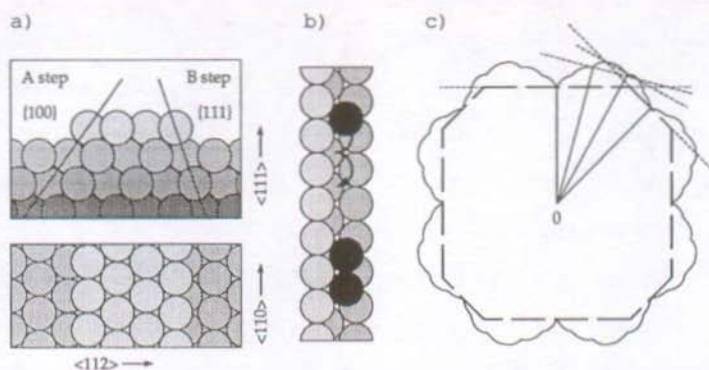
29

Fig. 2.9: a) Side and top view of the two possible close-packed step orientations on the (111) surface of a fcc lattice. The shown four-atom wide stripe runs along a <110> direction. A-type steps have {100} microfacets (see left hand side of the stripe), while the B-type step (right hand side) forms a {111} facet with the layers below (from [Stu 941]).

b) Illustration of one-dimensional diffusion along the steps and the creation of a kink - anti-kink pair, i.e. the nucleation of a 1D layer.

c) Wulff construction in two dimensions obtained by drawing planes perpendicular to the radius vector $\gamma(\tilde{n})\,\tilde{n}$. The crystal equilibrium shape is geometrically similar to the surface which can be reached from the origin without crossing any of the constructed planes (from [Her 51]).

The growth shape of adlayer islands is determined by the diffusion kinetics of the atoms adsorbed at its perimeter. Fast edge diffusion leads to low growth speed perpendicular to the step direction. The best example in this context has been given by Michely et al. for Pt growth on Pt(111) [Mic 93]. The authors could correlate the anisotropic growth shape of Pt island to the different diffusivity of Pt atoms along A- and B-steps. At high temperature the shape of an adlayer island is equilibrated and can be deduced from the Wulff construction [Wul 01] (see Fig. 2.9 c)). The 2D-equilibrium shape on a fcc (111) surface is a hexagon solely bounded by close-packed steps to minimize kinks and thus the total free energy of the border. The length

ratio between A- and B-type steps of the equilibrium hexagon reflects therefore the ratio between the step free energies γ_A and γ_B [Mic 912, Mic 93]. B steps have in the case of Pt/Pt(111) the lower free energy per unit step length which appears natural since {111} facets do have a lower surface free energy than the {100} ones.

2.3.6 Interdiffusion

Interdiffusion between film and substrate atoms leads to smearing out of the film-substrate interface. Alloy formation is observed for Ag films on Pt(111) at submonolayer coverages (T > 620K). The driving force is the discontinuity of physical properties, such as bonding, lattice parameter, and thermal expansion coefficients [Mer 84]. The thermodynamic criterion for the miscibility of two metallic components is discussed in chapter 5. Its use in the framework of the growth mode model is difficult since the heat of mixing is an additional contribution to the poorly defined interfacial energy [Bau 82]. The formation kinetics for the necessary place exchanges between film and substrate atoms proceeds by temperature dependent rate processes [Bau 82, Mer 84].

Intermixing has been found at higher temperatures e.g. for the system Ag/Pd(111) [Gug 80, Fis 93]. Here the Ag films are similarly strained as in the case of Ag/Pt(111) because the lattice constants of Pt (a_{Pt} = 3.92Å) and Pd (a_{Pd} = 3.89Å) differ only slightly. Also the strain relief mechanism for Ag/Pd(111) [Eis 93, Ran 94] is comparable with the results discussed in chapter 6. Thus, similarly strained Ag layers intermix with two chemical different substrate atoms which indicates the close relation between alloy formation of heteroepitaxial films and the strain-driven tendency to smooth the film-substrate interface.
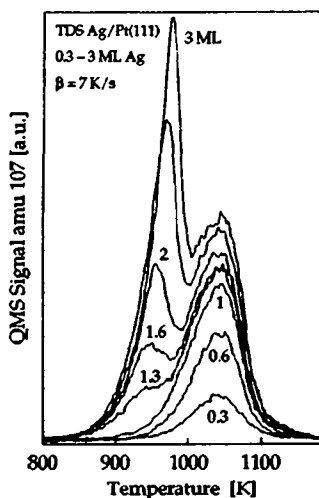
Fig. 2.10: Thermal desorption of Ag from Pt(111). At submonolayer coverages, the TDS spectra show a single desorption peak with a peak maximum at T = 1042K. For coverages Θ > 1 ML the development of a second peak with a lower temperature maximum is seen, i.e. the higher layers are less strongly bonded to the substrate (from [Här 93]).

2.3.7 Desorption

The mean residence time of single atoms on the surface before desorption is $\tau_a = \nu_0^{-1} \exp(E_a/kT)$. In several previous studies of Ag growth on Pt(111) [Dav 82, Paf 85, Här 93] thermal desorption spectroscopy (TDS) has been applied to Ag films on Pt(111). The TDS-spectra shown in Fig. 2.10 give a first hint for the layer dependent Ag structure on the substrate. The activation energy E_d for desorption measured by TDS reflects directly the strength of the adsorption potential E_A [Hen 91, Lüt 93].

The analysis of the multilayer desorption peak corresponds to an activation energy of $E_d = 2.86\pm0.04$ eV ($\nu_0 = 2\times10^{14}$ Hz) [Här 93]. This energy is, within the error margin, equal to the heat of sublimation of bulk Ag. The desorption temperature maximum of the first monolayer, however, is

32

about 70K higher yielding, according to first-order desorption kinetics analysis, a 0.17 eV higher desorption energy (E_d = 3.04±0.02 eV, v_0 = 1.5±0.5x10^{14} Hz) [Här 93]. Thus, Ag deposited on the Pt(111) surface seems to be 6% more strongly bonded to the substrate than to a bulk surface of Ag.

3. Experimental

A short introduction in the field of scanning probe methods is followed by a description of the developed STM instrumentation. The last section contains theoretical results which are relevant for the image interpretation in this thesis. This part displays typical measurements and is furthermore used to quantify the performance of the constructed microscope.

3.1 Scanning probe methods

Due to its invention in 1981 by Binnig and Rohrer [Bin 82], the scanning tunneling microscope has initiated a novel tool in experimental surface science: the local probe microscopy. The interaction between a fixed probe particle and the sample surface is used to measure the spatial dependence of surface properties on a nanometer scale. Today, numerous scanning probe microscopies (SPM) are available replacing the electron tunneling by other interactions (various kinds of forces, heat transfer, ionic conductance, optical and acoustic near-field microscopies, etc.) to address a variety of insights from surfaces, interfaces and mesoscopic systems (a numerous number of reviews and books are available, see e.g. [Wic 89, Mur 90, Beh 90, Gün 92, Roh 94])

The fundamental new approach of these methods is the performance of an experiment between atom-sized regions of the probe and the object of investigation. The spatial resolution of a SPM method depends on the effective probe size R, the distance d between probe and object, and the distance dependence f(d) and the lateral variation of the interaction under consideration [Roh 94]. For an exponential distance dependence $f(d) \propto \exp(-\kappa d)$, the localization is of the order $\sqrt{(d+R)/\kappa}$, where $1/\kappa$ is the decay length of the interaction. For electron tunneling between two bare metal
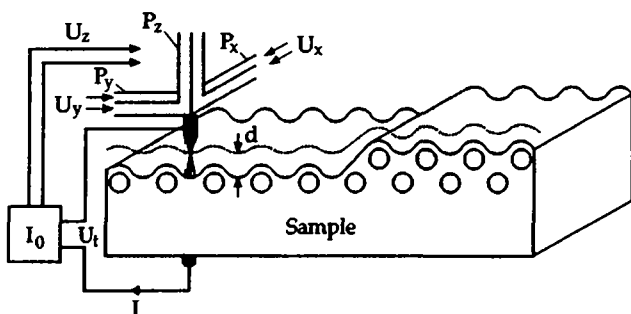
Fig. 3.1: Operation principle of the scanning tunneling microscope in the constant current mode. During scanning in x,y directions a feedback circuit keeps constant the current I_0 of electrons tunneling between a sharp tip and the sample surface. The deflection $\Delta z(x,y)$ to stabilize I_0 is generated by the piezoelectric transducer P_z. The applied tension U_z is at the same time measurement signal, i.e. $\Delta U_z(x,y)$ reflects the surface topography (from [Bin 86J]).

surfaces, $1/\kappa$ is about 0.4Å and the tunneling distance d is between 5Å to 10Å. Thus, assuming a size R of several Å for one of the tunneling electrodes, most of the tunneling current flows between atom-sized regions.

The experimental requirement to use these microscopies is the macroscopic control of the probe-sample interaction restricted to microscopic dimensions. For electron tunneling this is possible by applying a voltage U_t between a sharp tip and the sample surface and measuring the resulting tunneling current I_t. The ideal STM probe has only one atom on the tip apex fixed in a chemically and mechanically stable position. In the constant current mode of the STM (see Fig. 3.1) the tunneling current I_t flowing through the apex atom is kept constant at I_0 stabilizing the tip-sample interaction. The width d of the tunneling barrier is easily controlled with subatomic precision, since I_t changes roughly by one order of magnitude for every Å change of d [Bin 81]. Scanning the tip in the orthogonal x,y

directions at constant tunneling parameters I_t, U_t represents the spatial dependence $z(x,y)$ of tip positions with equal barrier width $d\big|_{U_t,I_t}$.

Several other STM modes of operation are widely used (see e.g. [Beh 86, Bon 93]). They follow other trajectories in the STM parameter space (x,y,z,I_t,U_t) to extract, for example, the spatial variation of the apparent barrier height $\partial I_t/\partial z\big|_{U_t,I_t}$. This quantity is (for large gap widths) proportional to the square root of the local work function ϕ of the surface [Che 911, Schu 922]. On non-homogeneous surfaces local changes of ϕ can be attributed to chemical and structural defects resolvable by the map $\partial I_t/\partial z\big|_{U_t,I_t}(x,y)$ [Beh 86]. Spatial resolved tunneling spectroscopy records $I_t(U_t)$-curves as a function of the tip position $z(x,y)$ (see e.g. [Ham 89, Win 92]), historically the motivation for the STM-development [Bin 87]. The spectroscopic use of the STM focuses on the local electronic structure of surfaces. Unfortunately, a $I_t(U_t)\big|_{x,y,z}$ spectrum results from a convolution of tip and sample properties with a complex dependence on the barrier width d. Deconvolution is feasible [Che 92, Cro 932], but laborious since the imaging tip structure is in general unknown.

It has been shown theoretically [Che 912] and experimentally [Dür 86, Dür 88] that forces are involved in the STM imaging process, at least at small gap widths. This reveals the close relation of STM and atomic force microscopy (AFM) [Bin 861]. Furthermore, the inelastic part of the tunneling current, i.e. electrons which loose energy by traversing the barrier, is a further channel of nanometer scale imaging. Photons are emitted [Gim 88, Ber 92] and molecules may be excited in the tunneling gap [Per 86, Bar 88]. While the latter is experimentally difficult to observe [Zep 912], photon emission from the STM is nowadays routinely used to characterize surfaces and adsorbed molecules [Ber 93]. Many other phenomena in the STM junction have been reported, e.g. optical interactions induced by laser illumination in

the tunneling gap [Arn 87, Kuk 90]. Thus, the "classical" STM remains a fascinating tool to develop new scanning probe methods.

3.2 Variable temperature scanning tunneling microscopy

The formation of the chemically and structurally inhomogeneous interfacial region between epitaxial film and substrate requires clean experimental conditions to control the presence of impurities. Due to this fact, substrate preparation, vapor phase deposition, and STM-measurements were performed in an ultra-high vacuum (UHV) environment. The second experimental requirement has been deduced in the second chapter and consists of controlling the external growth parameters, i.e. the deposition flux R and the substrate temperature T. Vapor phase deposition is performed by evaporation of the film material. By choosing different temperatures of the Knudsen effusion cell the flux R of the Ag beam is easily adjustable [Knu 09]. Controlling the influence of substrate temperature T is experimentally more difficult. Imaging of metastable film morphologies requires temperature control during all preparational stages and during STM-observation. The latter is necessary to avoid post-growth changes of the film due to the measuring conditions. For this purpose, a home built STM has been used allowing variable temperature measurements in the range from T = 25K to 800K. Thus, for a given metastable morphology, an adapted imaging temperature can be chosen preventing modifications of the film.

3.2.1 The "beetle" STM

The instrument built is based on the "beetle" STM [Bes 87, Fro 89, Mic 912]. Similar experimental set-ups for UHV characterization of metal surfaces have been constructed by Michely [Mic 911] and by Wolf [Wol 90]. In the
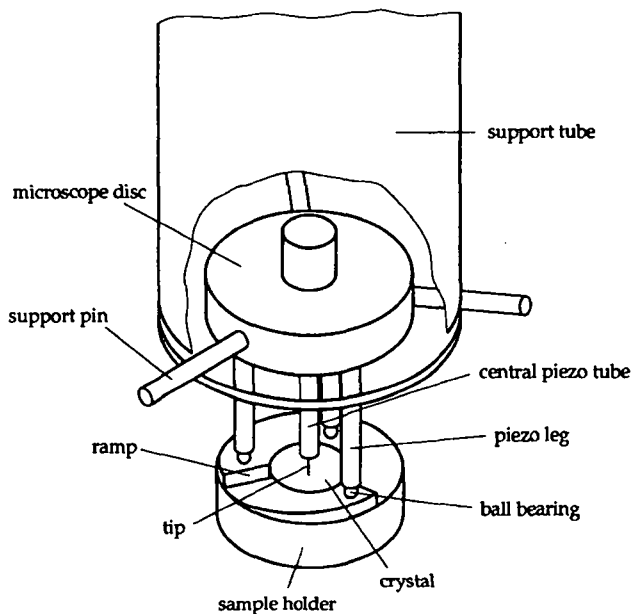
Fig. 3.2: Sketch of the used "beetle" STM. The microscope can be lowered onto the sample holder by means of a UHV-manipulator on which the support tube is mounted. During measurements the STM is mechanically uncoupled from the support tube. The only exception is the electrical contact of the piezoceramics performed with thin ($\varnothing = 50$ µm) wires.

present work, the accessible temperature range of this STM type (reported so far 100K to 450K [Mic 912]) could be increased especially to lower temperatures. General principles and design criteria for STM constructions can be found e.g. in [Poh 86, Kuk 89].

The association with a beetle becomes evident by inspection of Fig. 3.2 showing the principal idea of the instrument [Bes 87]. The microscope consists of an aluminum disc which holds four identical piezoceramic tubes ($l = 13$ mm, $\varnothing_0 = 2.6$ mm, $\varnothing_i = 1.75$ mm, material: "Vibrit" 420 [Sie]). The three outer piezo tubes (the "legs") are mounted in a threefold symmetric

arrangement. In the center of the disc the central piezo tube (the "feeler") carries the tunneling tip. The legs are equipped with small spheres to which the whole microscope stands on a molybdenum ring with three ramps cut into it. Each ramp is 0.4 mm high, spans an arc of 120° and is used as "standing area" for one of the three "beetle" legs [Fro 89]. The Pt-crystal is clamped between the sample holder and the ring.

Once the "beetle" STM is mechanically uncoupled from the upper support tube, all displacements are generated by the piezo tubes by applying appropriate voltage pulses to the piezo electrodes (see Fig. 3.3). The tip approach is achieved by a collective motion of the legs rotating the microscope clockwise. Thus, the instrument is "screwing" itself down the ramps and moves the tip towards the sample. The rotation is automatically stopped when a tunneling current is detected. Sample scans can now be performed by two ways. Either the central tube scanner moves the tip in all three spatial directions, or scanning is done by the outer piezo tubes and only the z movement is performed by the central piezo.

Changing the scanning region to investigate different sample areas is also possible by two methods. First method: off-set voltages on the piezo legs bend the hole disc to move the tip relatively to the sample. This method can even be used during image acquisition and enables a continuous shifting of the scanning zone. Second method: a linear transport of the hole microscope as used for the coarse approach. The disadvantage of this method is that tunneling has to be interrupted during the displacement. The feedback circuit is too slow to follow the abrupt sliding of the metal spheres over the ramps. The advantage of this linear transport is that larger STM displacements are easily achieved without a new mechanical tip approach, i.e. afterwards the tunneling contact can be achieved by means of off-set voltages on the z-piezo electrode.
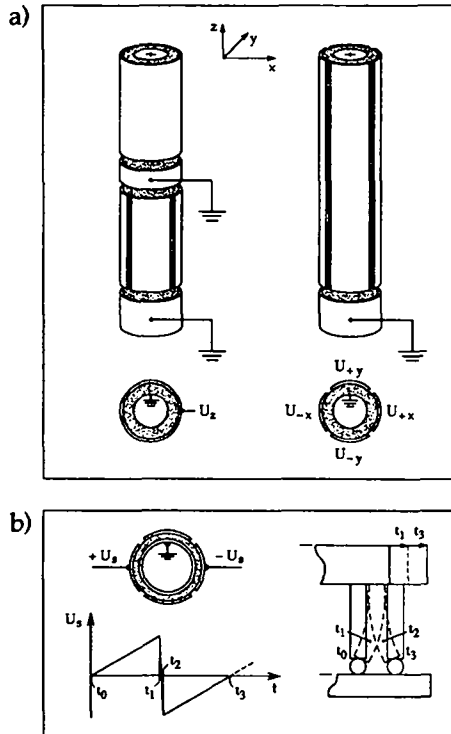
Fig. 3.3: a) Electrode segmentation of the radial polarized piezoceramic tubes. The inner wall is grounded and voltage on the outer electrode causes a uniform expansion or shrinkage of the tube [Bin 862]. Left: central piezo holding the tip. The upper part is used for displacements in z direction. The middle part is grounded to avoid coupling with the lower scanning part [Car 88]. Right: piezo tube acting as "beetle" leg. Voltage on these vertical separated electrodes bend the tube perpendicular to its symmetry axis (in the same way for the scanning part of the central piezo). Due to the macroscopic tube dimensions the bending angle is very small for the STM scan lengths used leading only to a lateral displacement of the tube (from [Mic 911], modified).

b) Displacement of the microscope by means of triangular pulses on the outer piezo tubes. During the steep part of $U_S(t)$ the legs glide over the ramps, while the disc doesn't move due to its inertia. This leads to an effective transport with respect to the sample enabling tip approach and lateral displacements to change the scanning region (from [Mic 911]).

41

Routinely, the first scanning mode has been used: the tip is displaced alone by means of the central piezo tube. Scanning with the legs has a lower mechanical stability due to the lower resonance frequency of the whole disc with respect to the single tube scanner. A second reason is that the outer tube scanners are more sensitive for thermal drift effects, since they have direct thermal contact with the sample.

The tip structure is continuously modified by applying voltage pulses which leads to material exchange between tip and surface. Once this "trial and error" procedure has led to satisfying resolution, the scanning region is changed to record images. During this preparational method, the continuous shifting of the scanning area performed with off-set voltages on the legs is advantageous. Using this displacement method, it can be avoided that an optimized tip structure is further altered by scanning on previously modified surface regions.

The principal advantages of this microscope type are the following:

- The design of the "beetle" STM is simple and compact. Due to its "pocket-size" and rigid construction it is not very sensitive to external vibrations.

- The thermal drift is compensated by the fact that the microscope stands on piezo legs which have equal thermal expansion rates as the central tube scanner to which the tip is mounted. Thus, to first order, the tip-sample distance remains unchanged upon temperature variation.

- The STM requires only one flange ($\varnothing_i \geq 63$ mm) at the top of the UHV chamber facilitating the combination with other analytical methods [Röd 91]. Since the microscope is placed on the sample,

no complicated sample transfer mechanisms inside the UHV system are necessary.

3.2.2 Sample manipulator and UHV-chamber

The excellent temperature stability of the "beetle" STM allows measurements at variable crystal temperature in a room temperature environment. The temperature of the sample is changed by means of the cryogenic specimen holder sketched in Fig. 3.4. As discussed below, this implies essentially no cooling or heating of the microscope. The sample and its small holder are contained in a rigid UHV-manipulator with only one degree of freedom: a rotation around the horizontal axis of the support tube ($\varnothing_0$ = 54 mm). After lifting of the STM, the crystal can be rotated under full temperature control in front of the substrate and film preparation stages. Due to this possibility, metastable film morphologies can be imaged at the same temperature as prepared or at a desired different temperature.

The design goal of the sample manipulator is to achieve a compromise between two requirements. First, a mechanically stiff construction sufficiently damped is required to act as "beetle" STM base. Second, a thermally isolated sample with a large range of temperature variability is desired. Cooling of the sample is the technical critical point by finding a good middle course between the two demands. Heating causes no mechanical vibrations and can effortlessly integrate in a temperature compensated STM design. Cooling, on the other hand, produces vibrations due to the liquid He flux of the home made cryostat. The latter demands a mechanically "soft" connection to the crystal holder with a high thermal conductivity. For this purpose, the hat-shaped Pt-sample ($\varnothing$ = 11 mm) is clamped to a small Cu piece which is connected to the cryostat heat exchanger through a soft Cu braid ($\varnothing$ = 4 mm, length 50 mm) [Dav 86, Mic
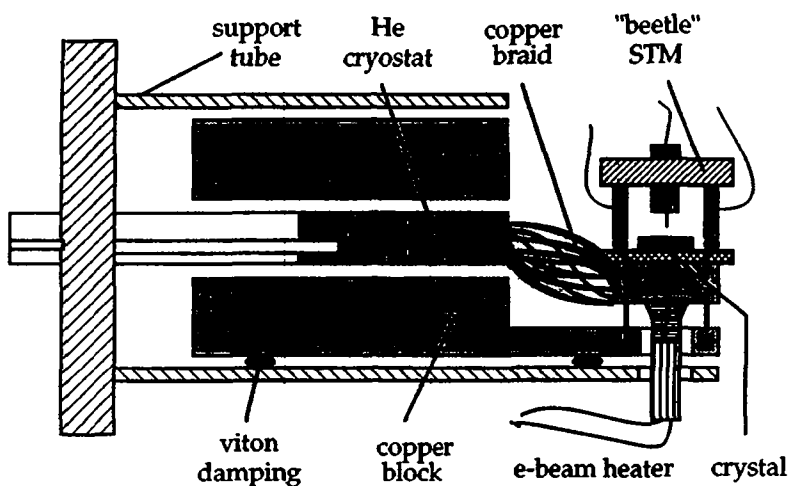
Fig. 3.4: Essential elements of the UHV sample manipulator. Details in text.

911]. The braid is furthermore untwisted into several single cords to reduce its stiffness.

In order to cool and heat only the sample, this small assembly is thermally isolated from the big Cu block on which it is rigidly mounted. This fixation is performed by three pulling and three pushing stainless steel screws (ø = 1.4 mm). Their low thermal conductivity towards the Cu block allows sample temperatures down to T = 25K [Dav 86]. The cylindrical Cu block resides on viton spacers damping high frequency external vibrations [Mic 911] and has no otherwise mechanical contact inside the support tube. The only exceptions are the electrical connections of the filament and the thermocouple wires measuring the crystal temperature. As a further vibration isolation the whole UHV chamber is mechanically damped against low frequency excitations by an air suspension system. It has been shown that the combination of an external low- with an internal high-

frequency damping stage yields optimum performance [Schm 92]. The stiffness and the damping of the construction are sufficient for a vertical STM stability of about 0.1Å. Especially, no influence of the sample temperature on the STM sensibility has been found, i.e. vibration caused by the He flux are effectively suppressed by means of the soft Cu braid and the big mass of the Cu block.

Heating is done either by radiation or by electron bombardment from the W/Re filament (ϕ = 0.25 mm) located behind the sample. Annealing temperatures up to T = 1300K are possible due to the negative bias on the hot filament (-1250V with respect to the grounded sample). Temperature control of the sample is achieved by Ni-CrNi-thermocouple wires (ϕ_0 = 0.1 mm) spot welded onto the brim of the hat-shape crystal. During film preparation and STM measurements the temperature is kept constant within ±0.1K by means of a commercial PID controller regulating the filament current. From the nucleation studies at low temperatures in chapter 4 the reproducibility of the substrate temperature can be determined to ±1K for T > 50K. Absolute temperature calibration has been checked by holding the whole manipulator outside vacuum in liquid nitrogen yielding ΔT = ±2K. The comparison of the low temperature STM data with thermal energy helium scattering measurements [Rom 94] results in the same error range of the absolute sample temperature calibration.

Lowering the microscope onto the cold or hot sample holder establishes a temperature gradient between both, maintained by the low thermal conductivity of the stainless steel spheres (ϕ = 2,5 mm) glued on the piezo legs. Equilibration occurs within several minutes up to half an hour at the lowest and highest temperatures.
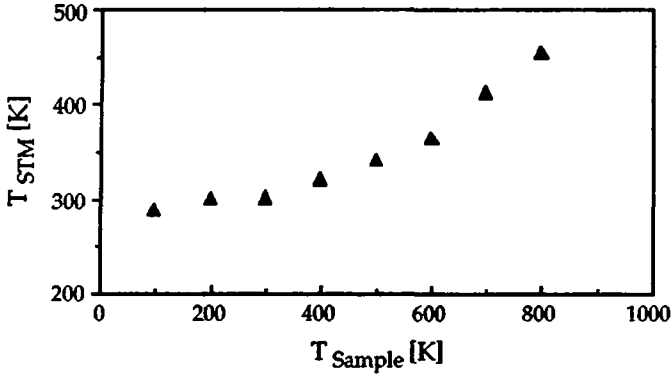
Fig. 3.5: Plot of the STM temperature versus sample temperature measured after an equilibration time > 1h.

The dependence of the equilibrated STM temperature on T_{Sample} is shown in Fig. 3.5, where T_{STM} has been measured at the central tube scanner. For $T_{Sample} < 300K$ the microscope temperature hardly changes, while for $T_{Sample} > 300K$ the thermal radiation from the sample becomes increasingly important. For $T_{Sample} > 600K$ the microscope temperature raises finally with a slope of $\approx 45K$ per 100K sample temperature increase. In the temperature range $25K < T_{Sample} < 500K$, however, the microscope stays basically at room temperature such that thermal effects on the deflection/voltage characteristic of the used piezoceramics are negligible, i. e. they are within the 5% errors bar of the STM calibration. The upper limit is given by the depolarization of the ferroelectric piezoceramics and has been fixed to the bake-out temperature of the UHV-system (450K), i.e. $T_{Sample} = 800K$.
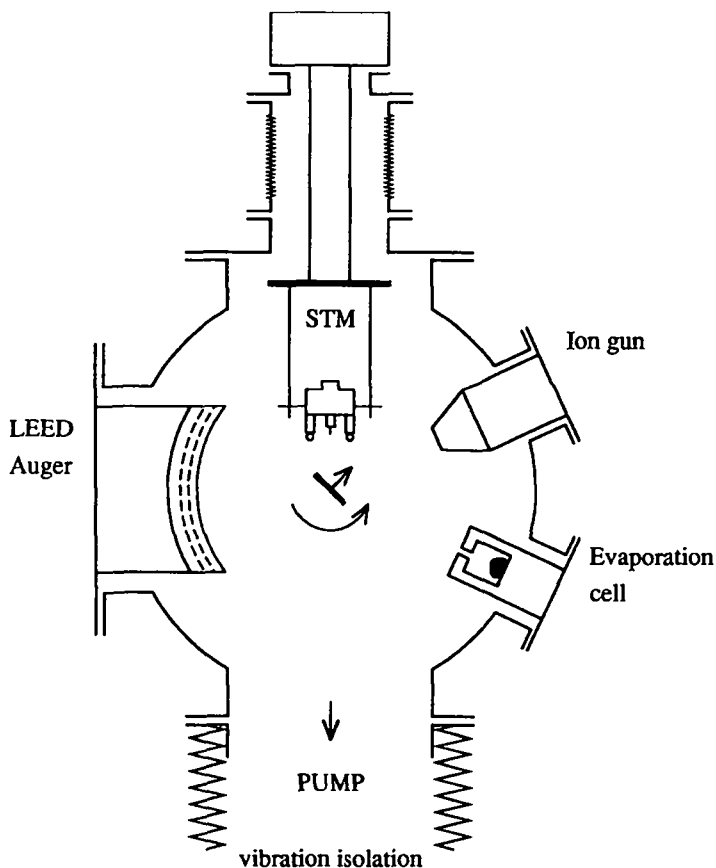
Fig. 3.6: Sketch of the UHV chamber geometry. The shown section lies in the center of the specimen holder. Details in text.

The sample manipulator is attached to a 8" o.d. double cross as UHV chamber (base pressure in the upper 10^{-11} mbar range) sketched in Fig. 3.6. The UHV system is equipped with a 340 l/s turbomolecular pump which can be valved off, a 270 l/s ion pump, and a titanium sublimation pump. A smaller (50 l/s) turbomolecular pump is used for pumping the gas inlet

system and the differential pumped ion source. During STM measurements all mechanical pumps are turned off in order to avoid vibrational perturbations. The rotation of the sample manipulator is performed with a differentially pumped rotary feedthrough. The vacuum of its spacer volume ($< 10^{-3}$ mbar), normally pumped by a rotary vane pump, is maintained by a liquid nitrogen cooled sorption pump during measurements. The UHV system is further equipped with the usual techniques for sample and film preparation and its control: an ion gun, a quadrupole mass analyzer to control the residual gas, a back view LEED, and a MBE Knudsen cell. The LEED electron optics can also be used as retarding field energy analyzer for Auger electron spectroscopy (AES).

3.2.3 Film preparation and image treatment

Experiments have been performed on two different high quality Pt-crystals [Lin 85] oriented in the (111) direction with an accuracy better than 0.1°. The substrates have been each cleaned in UHV by repeated cycles of Ar ion bombardment (650 eV) at $T = 850K$, chemical treatment by exposing in an oxygen atmosphere ($T = 850K$, 5×10^{-7} mbar) and subsequent flash annealing to $T = 1200K$. Surface cleanness has been routinely checked by STM. After the first cleaning cycles, control by AES was no more suitable due to the low sensibility of the present AES set-up ($\geq 1\%$ of a monolayer). The clean Pt(111) surface consists of flat terraces with an average width of 1300Å separated by steps of monatomic height. STM tips have been prepared by electrochemical etching of polycrystalline W wires ($\emptyset_0 = 0.25$ mm) in 5% Na(OH) solution as described in ref. [Mic 88].

Ag films were grown by means of the Knudsen-cell at a background pressure better than 2×10^{-10} mbar. The rate of deposition was calibrated by measuring the Ag-covered area in STM images at $T = 300K$ for almost

monolayer coverage where the effect of borderlines is minimized. Once the rate was calibrated this way, the deposited amounts of Ag lead reproducibly to the expected coverages within 5%. The coverage is given in monolayers of the Pt(111) substrate (1 ML = 1.50 x 10^{15} cm^{-2}). The flux has been varied by changing the Ag evaporation temperature. The obtained flux changes ΔR are well correlated with the tabulated vapor pressure dependence on temperature. In the first experiments a coverage gradient at the crystal borders was present due to an additional aperture in front of the source (mounted to avoid evaporation on the surrounding molybdenum ring). Higher error bars are attributed to the data extracted from these images.

The used electronics corresponds to the commercial "beetle" STM electronics [Bes]. The calibration of the central scanner has been taken from two identical microscopes [Hah 93, Buc 93]. The deflection/voltage conversion of the central piezo tube turns out to 110 Å/V in lateral and 30 Å/V in vertical direction in fair agreement with ref. [Mic 911] where the same piezo tubes were used. All images were obtained under constant tunneling current condition with a scanning frequency of 4 Hz in the fast x-direction. Topographies were recorded in the differential mode as in Fig. 3.7 or in the absolute height mode, where the gray scale reflects the absolute tip height. In these images, as in Fig. 3.8, a planar background has been subtracted to tilt atomic terraces in such a way that they are represented as horizontal areas. In differential topographies a signal proportional to the derivative $\partial z/\partial x$ is recorded using a high pass filter with a cut off frequency of 33 Hz. In these images the film morphology is represented as if it would be seen with illumination at glancing incidence from the left. Filtering of data has been avoided, but in some images the removing of a 50 Hz perturbation frequency has improved the presentation of the film structure.

49

The lateral drift in the STM images is determined by comparison of consecutive recorded images. The drift decreases during the equilibration time, but increases by displacements of the microscope, i.e. depends on the specific position of the microscope onto the sample. Independent of position, a non-vanishing drift of the order 5 nm/min at cryogenic temperatures is observed. Quantitative data extracted from STM images, e.g. island densities, have been always corrected for drift effects. A lateral drift correction of the STM topographies shown here was usually not necessary (< 10% of the image size). Exceptions are the following images : Fig. 4.1, 4.3 b) and 6.9 b).

3.2.4 Experimental outlook

Several improvements of the STM system are possible since the system has been mounted within half a year (project name: "STM Quick"). Some of them have been realized during the redaction of this thesis:

- Around the sample manipulator a new UHV chamber has been constructed avoiding geometric restrictions of the double cross system, e.g. new space to add a cylindrical mirror analyzer (CMA) for higher sensitive AES, a more favorable geometry of the evaporation sources and sputter gun, additional flanges, etc.

- Improvements of the two vibration isolation stages have been realized to increase stability and consequently the lateral and vertical STM resolution.

- The sample has been electrically isolated from the chamber without loosing stability or cooling power. This is one of the requirements to perform a fast tunneling spectroscopy [Bru 92],

i.e. to record $I_t(U_t)\big|_{x,y,z}$ spectra with a spatial resolution of a few
$\mathring{A}^2$.

- A high performance STM electronics has been adapted to the
  system leading to many new possibilities for image acquisition
  and processing.

3.3 STM imaging of Ag layers on Pt(111)

The tunneling effect as a transfer of particles through energetically
forbidden regions is well understood for many phenomena and applications
[Roy 86, Feu 87]. Understanding STM images and spectra in terms of
microscopic tip and sample parameters is a more complex task (a
comprehensive summary of the "state of the art" in STM theory has been
given by Chen [Che 93]). The difficulty to describe atom-scale tunneling in a
quantitative way is best illustrated by application of the uncertainty
principle to the STM problem [Che 93]. Assuming typical values, the energy
uncertainty of the tunneling electron is larger than the absolute value of the
kinetic energy. Thus, the distinction between tunneling and ballistic
transport disappears. Application of the uncertainty relation between
coordinate and momentum leads to a position uncertainty much larger
than the barrier width. Consequently, for any time it is not predictable on
which side of the STM junction the electron can be found.

3.3.1 The s-wave-tip model

The first quantitative theory to explain the image contrast in STM has been
developed by Tersoff and Haman [Ter 83, Ter 85]. The modeling of the tip is
rather scarcely by assuming a spherical piece of free electron metal with a
radius of curvature R in the part where the tip approaches nearest the

sample. First-order time-dependent perturbation theory yields the following expression for I_t:

$$I_t = \frac{2\pi e}{\hbar} \sum_{\mu,\nu} f(E_\nu)\left[1 - f(E_\mu - eU_t)\right] \left|M_{\mu,\nu}\right|^2 \delta(E_\mu - E_\nu) \qquad (1)$$

where $f(E)$ is the Fermi function and $M_{\mu,\nu}$ is the tunneling matrix element between the unperturbed tip and sample states ψ_μ, ψ_ν having energies E_μ and E_ν, respectively [Bar 61]. In the case of low temperature and small bias U_t one obtains an extremely simple dependence for the tunneling current:

$$I_t \propto \sum_{E_\nu = E_F - eU_t}^{E_F} \left|\psi_\nu(\bar{r}_0)\right|^2 = eU_t\, \rho_S(\bar{r}_0, E_F) \qquad (2)$$

where $\rho_S(\bar{r}_0, E_F)$ is the local density of states (LDOS) of the sample taken at the Fermi-level E_F and the center of curvature of the tip $\bar{r}_0$. The exponential dependence $I_t \propto exp(-2\kappa\,d)$ on the barrier width d can be deduced with the help of the omitted prefactors in (2). The decay length κ turns out to $\sqrt{2m_e\phi}/\hbar$, where ϕ is the work function of tip and sample and m_e the electron mass.

Thus, at constant I_t and U_t, the tip follows the lines of constant Fermi-level LDOS. The LDOS is a well-known quantity in surface physics (see e.g. [Smi 75, Zan 88]). For free-electron metals, the Fermi-level LDOS values at a distance from the surface almost coincide with the contours of the total electron density. In this case, the contrast of a constant current topography is therefore directly correlated with the surface charge-density. This basic reading of an STM image is supported by the imaging effects observed for strained Ag layers adsorbed on and embedded in the close-packed Pt(111) surface, as discussed below.

The most important approximation in the Tersoff/Haman theory lies in the evaluation of the matrix element $M_{\mu,\nu}$ by using as tip wave functions only solutions of the Schrödinger equation for a spherical potential wall of radius R (s-waves). Thus, microscopic tip properties are taken out of the problem and the I_t-characteristic reflects the property of the sample only. Coupling of the two tunneling electrodes is not included. The wavefunction overlap in the gap is calculated from eigenstates of the free tip and the free sample, only. This drastic oversimplification together with the macroscopic tip modeling restricts the validity of the s-wave model to large barrier widths. In fact, the description of atomic resolution on low-index metal surfaces is beyond the scope of the LDOS interpretation, as revealed experimentally [Hal 87, Win 89] and theoretically [Che 901]. The observed atomic corrugation amplitudes are a factor 10-100 higher than the LDOS variations.

Using a modified perturbation approach Chen was able to treat the problem of bias dependent coupling of the two unperturbed Hamiltonians of the tip and the sample [Che 88]. By calculating tunneling matrix elements $M_{\mu,\nu}$ with tip-states of s-, p- and d-symmetry [Che 902] the microscopic tip-sample interaction is predictable. The often observed sudden change of resolution and corrugation amplitudes in STM images is therefore quantitatively describable by abrupt alteration of the imaging tip-state. Nevertheless, the s-wave model holds its place as the macroscopic limit of the microscopic STM theory. Zeppenfeld et al. confirmed this behavior by imaging the Pt(111) surface at atomic resolution for a wide range of experimental conditions [Zep 911]. "Low resolution tips" were found showing corrugation values being consistent with the predictions of the Tersoff/Haman theory.
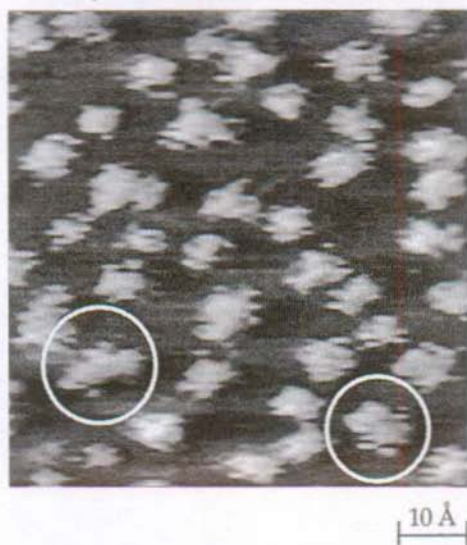
53

$T = 50 \text{ K}, \quad \Theta = 0.1 \text{ ML}$

10 Å

Fig. 3.7: Lateral resolution limit of the home built STM. After deposition of $\Theta = 0.1$ ML at T = 50K a mixture of small clusters (average size $\bar{n} = 2.8 \pm 0.4$ atoms) has been formed. A few individual clusters can be recognized. The encircled linear (left) and triangular (right) trimer are imaged with a next neighbor distance of about 3Å. This differential STM image (68Åx68Å) is an enlargement of Fig. 4.3 b).

3.3.2 Ag/Pt(111): Imaging effects

The lateral resolution limit (≈3Å) of the constructed STM is documented in Fig. 3.7. From a mixture of small adsorbed Ag cluster only a few can be recognized. The lack of atomic resolution images for a direct distinction of cluster sizes leads to an indirect way of data evaluation. Cluster distributions are in the following characterized by the calibrated coverage Θ of the deposit and the island density ρ. The latter is evaluated by counting islands and dividing their number by the area of the image. The ratio of coverage Θ [ML] and island density ρ (in islands per Pt(111) adsorption site ≡ [ML]) is then the average island size $\bar{n}$ (in atoms per island).

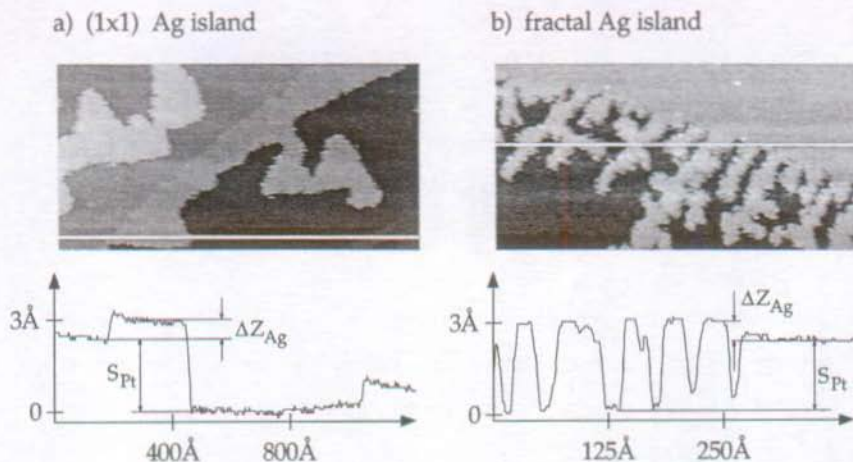a) (1x1) Ag island   b) fractal Ag island

Fig. 3.8: a), b) Imaging height of **monatomic thick Ag** on Pt(111). The absolute height STM topography shows in a) a large (1x1) island attached to an ascending Pt step. An imaging height difference of ΔZ_{Ag} = 0.7Å between the Ag step and the Pt substrate step is observed. About the same ΔZ_{Ag} value is visible in b) for diffusion limited grown Ag attached to an ascending Pt step. The smallest width of the islands is about 20Å. Preparation: a) growth of Θ = 0.5 ML at 350K (imaging at 350K), b) growth of Θ = 0.1 ML at 120K (imaging at 120K) The shown line scans are taken along the white bar marked in the images. Tunneling parameters: a) I_t = 2.0 nA, U_t = -1.2 V, b) I_t = 1.0 nA, U_t = -1.0 V, image sizes: a) 1230Åx615Å, b) 390Åx195Å, used flux R = $1.1x10^{-3}$ ML/s.

Also the imaging of the atomic Pt(111) structure (next neighbor distance of the surface atoms: 2.77Å) was not successful even under stable external conditions (night) and at the smallest gap resistance available (R_G = 250 kΩ). The reason is probably the insufficient stability of the present STM excluding imaging with "high resolution tips". Thus, the below given interpretation of imaging effects deals only with tip states for which the charge-density interpretation of the STM contrast is a reasonable assumption.

Absolute height STM topographies of two-dimensional Ag islands on Pt(111) are shown in Fig. 3.8. The Ag islands (attached to an ascending Pt-step) appear about $\Delta Z_{Ag} = 0.7$Å higher than a monatomic step of the Pt-substrate. This important imaging feature is observed under various tunneling conditions and no dependence on the lateral size of the Ag islands is remarkable. Even fractal Ag island having a width of a few atoms exhibit the same imaging effect. The magnitude of this chemical contrast between Ag and Pt depends slightly on the specific tip structure (variation ±0.2Å). Neither a specific dependence on the gap width, nor an influence of the U_t-polarity could be detected.

A STM image contains a mixture of geometrical and electronic information. The geometrical height of a Pt(111) step is 2.27Å, whereas the spacing between subsequent Ag(111) planes is 2.36Å. As mentioned in 2.2.1, Ag adsorbs pseudomorphically on Pt(111) and is therefore compressed by 8.3% in density compared to its natural lattice. In view of this modified structure, it is unreasonable to explain the observed imaging effect with the 0.1Å step height difference between Ag(111) and Pt(111). Obviously, the height difference ΔZ_{Ag} is related to the electronic properties of the strained two-dimensional Ag.

The first possibility to cause a positive ΔZ_{Ag} value is a smaller apparent barrier height above the Ag islands. If this would be the case, the same tunneling current would lead to a larger gap distance on Ag than on Pt. As mentioned above, the barrier height is to first order related to the work function ϕ. The work function change $\Delta\phi$ during Ag growth on Pt(111) shows a linear drop by 1.2 eV after deposition of one monolayer [Paf 85, Här 93]. The absolute ϕ value at $\Theta = 1$ML is close to the one of Ag(111) suggesting that monatomic Ag islands on Pt(111) exhibit the work function of bulk Ag. Under this assumption, the imaging height difference ΔZ_{Ag} due to the

different decay constants κ_{Ag} and κ_{Pt} is easily calculable. With an absolute barrier width of $d \approx 4\text{-}7\text{Å}$ the work function difference $\Delta\phi = 1.2$ eV causes a step height difference ΔZ_{Ag} of $0.5\text{-}0.8\text{Å}$ in good agreement with the experiment.

Two arguments contradict this work function explanation. First, the quantity ϕ entering in the apparent barrier for the tunneling process cannot directly be identified with the work function measured with a surface integrating method [For 90]. Second, if the barrier height difference between Ag and Pt would be responsible for the imaging effect, a systematic increase of ΔZ_{Ag} with increasing gap width should exist. Since the latter was not detectable the above argumentation leads to inconsistencies.

The second possibility to cause a positive ΔZ_{Ag} value is a higher surface charge-density in the compressed Ag islands with respect to the Pt substrate. For this purpose, the imaging of the second Ag layer is taken into account. In the equilibrium structure of the Ag bilayer the compressive strain is partly relieved by the introduction of domain walls. Their symmetry and atomic structure will be discussed in detail in chapter 6. Obviously, any relaxation of the film as its thickness increases has to contain expanded Ag areas to approach the bulk structure of Ag.

The STM topography in Fig. 3.9 shows the Ag bilayer covering a substrate step which crosses the image from the upper right to the lower left. The second Ag layer of the lower Pt-terrace (left hand side) is attached to the first Ag layer of the upper Pt-terrace (right hand side). The main part of the upper Pt-terrace is covered with the second Ag layer but in the upper right corner a small region of the first layer is visible. The compressed first layer exhibits about the same imaging height as the Ag regions of the lower level second layer which are separated by the domain wall network. Thus, the
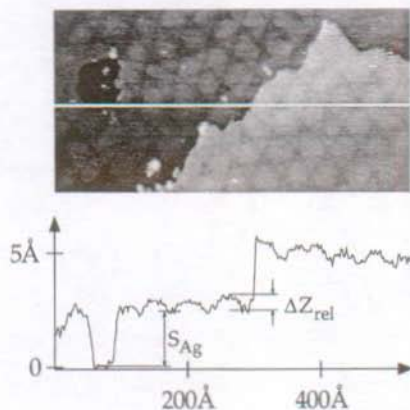
released Ag - bilayer

Fig. 3.9: Imaging height of the equilibrium **relaxation pattern of the Ag bilayer** on Pt(111). The line scan reveals a height difference of up to $\Delta Z_{rel} = 0.7\text{Å}$ between compressed Ag regions and diluted zones. Details in text. Preparation: growth of $\Theta = 1.5$ ML at 400K and subsequent annealing to T = 800K (imaging at 400K). The shown line scan is taken along the white bar marked in the image. Tunneling parameters: $I_t = 1.2$ nA, $U_t = -1.5$ V, Image size: 540Åx270Å, used flux R = 1.1×10^{-3} ML/s.

domain walls represent diluted Ag zones surrounding the areas of compressed Ag. The line scan in Fig. 3.9 compares the modulation of the second layer with its step height and reveals that the domain walls are imaged as depletions of up to $\Delta Z_{rel} \approx 0.7\text{Å}$. This amplitude is not directly comparable with ΔZ_{Ag} but shows that expanding of the compressed Ag leads to lower imaging height.

The imaging of the domain walls as depressions can be understood in terms of their dilution causing a lower electronic-density, thus leading to an imaging height close to their geometry, whereas the compressed areas are imaged higher due to their increased electronic-density. In the same way the compressive strain of the first Ag layer leads to a higher charge-density with respect to the Pt-substrate explaining the imaging height difference ΔZ_{Ag}.

This strain argumentation derived from the height modulation of the Ag bilayer assumes that the surface charge densities of Ag(111) and Pt(111) differ only slightly. This is confirmed by the fact that for both surfaces the STM step height is measured close to the geometry [Wol 90, Ber 92].

A similarly increased imaging height (0.5Å) has been observed in STM images of Au on Ru(0001) [Schr 92], where the Au (1x1) layer is equally compressed by 6.8%. Furthermore, a linear correlation between the surface charge-density and the film atom density has been recently demonstrated for pseudomorphic Cu layers grown on various metallic substrates (misfit range: -5.4% to +15.4%) [Kam 94]. Thus, the observation of an increased electronic-density due to compressive strain seems to be a general feature of mismatched metallic overlayers.

Surprisingly, this "pillow effect" of the surface charge-density remains valid even when both metals are situated in the same atomic plane. Fig. 3.10 shows the imaging heights which are relevant in STM topographies of the Ag/Pt alloy surface. The formation and the structure of this monolayer confined alloy is discussed in detail in chapter 5. The important issue here is that the same chemical contrast between Ag and Pt regions is present. The brighter areas in the STM topography correspond to Ag which is deduced from their augmentation with increasing Ag coverage.

The contrast of the linear Ag structure ($\approx$ 10Å wide) located in the middle of the image has been marked as ΔZ_{Ag}. The line scan in b) compares ΔZ_{Ag} with the step height $S_{Ag/Pt}$ and with two external calibration voltages Z_{cal} for the z-displacement of the piezo scanner. The latter is simply a rectangular modulation of the tip height in x-direction. The steep part of the voltage pulse is much faster than the response time of the feedback loop. Thus, this external tip modulation does not affect the imaging. A height modulation
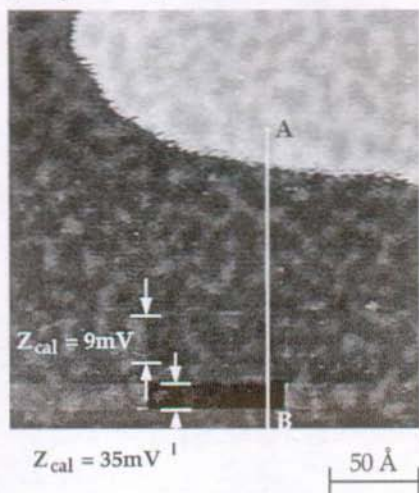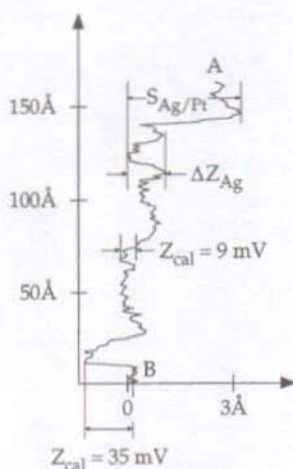
a) Ag/Pt alloy $\Theta = 0.5$ ML   b)

Fig. 3.10: a), b) Imaging height of monatomic thick Ag **embedded** in the Pt(111) surface. Annealing of Ag submonolayer coverages to T > 650K for annealing times > 100s leads to interdiffusion of Ag in the topmost Pt layer.

a) absolute height STM image of the frozen-in structure after deposition of $\Theta = 0.5$ ML at T = 750K (imaging at 400K). The alloy surface exhibits Ag regions of an average size of 10Å separated by Pt areas of the same size. Tunneling parameters: $I_t = 1.0$ nA, $U_t = -2.0$ V, Image size: 230Åx230Å, used flux: 1.1×10^{-3} ML/s.

b) The line scan along the bar AB marked in a) shows the imaging height ΔZ_{Ag} of embedded Ag regions with respect to Pt areas. ΔZ_{Ag} is compared to the imaging heights of a monatomic alloy step $S_{Ag/Pt}$ (upper part of the image) and two external voltage signals Z_{cal} applied during scanning of the lower image part. Details in text.

of $Z_{cal} = 35$ mV corresponds to about 1Å and again ΔZ_{Ag} turns out to 0.7Å. In the case of embedded Ag the obtained amplitude ΔZ_{Ag} depends more strongly on the tip structure which is attributed to the small lateral size of the Ag regions.

60

A similar chemical contrast within one atomic plane has been reported by Schmid et al. [Schm 93]. On the close-packed alloy surface $Pt_{25}Ni_{75}(111)$ Ni and Pt atoms could be distinguished by a height difference of 0.3Å. The contrast mechanism has been attributed to an adsorbate on the tip which tends to form a chemical bond more likely with one element than with the other. Due to the obtained atomic resolution and corresponding small tunnel distance (R_G = 50-300KΩ) these measurements are not directly comparable with Ag/Pt(111). Furthermore, the monolayer confined Ag/Pt alloy exhibits a high degree of chemical order in contrast to $Pt_{25}Ni_{75}(111)$ where only a short range order is present.

The embedded Ag exhibits basically the same strain of 4.3% as in the adsorbed case which has been verified by LEED measurements (see also [Bec 93]). Thus, the STM contrast obtained at the alloy surface corroborates a consistent image in which lateral compressive strain in monatomic Ag layers increases substantially the surface charge-density. The latter is observable by STM down to lateral sizes of 10Å and is hardly affected by the Ag environment, i.e. is valid for Ag adsorbed on Pt, adsorbed on strained Ag with Pt-structure and embedded in Pt.

The STM images shown in the following chapters have been recorded with tunneling currents of I_t = 1.0 to 3.0 nA at sample voltages from U_t = -0.5 to -2.0 V (R_G = 170 MΩ to 2 GΩ). The relatively high voltages lead to large gap widths and the used negative polarity samples mainly electrons from the occupied surface states near the Fermi-level [Beh 86]. Thus, the chosen tunneling parameters focused on the strain mediated imaging contrast between Ag and Pt.

4. Growth of Ag monolayers on Pt(111)

This chapter deals with low coverage (Θ < 0.6 ML) films at substrate temperatures between 35K and 500K. The coverage limit restricts the discussed morphologies and their formation kinetics to two dimensions. The upper temperature limit excludes exchange processes with substrate atoms. Section 4.1 serves as an introduction. The following three sections focus on the nucleation and cluster aggregation processes (4.2), the growth shapes (4.3), and the thermodynamic equilibrium of adsorbed Ag monolayers (4.4).

4.1 From kinetics to thermodynamics

The guideline for the discussion of growing Ag monolayer is given by the four STM images in Fig. 4.1. They show, on a lateral scale of 0.2µm, the main features observed between T = 80K and 400K. Growth and imaging temperatures of the films are identical.

At T = 80K a large number of round islands have nucleated with an average size $\bar{n}$ of 8±4 atoms. Growth at the slightly increased temperature T = 120K changes the island density drastically: here, only a few ramified Ag aggregates are visible. At T = 220K, on substrate terraces of lengths comparable to a) and b), no Ag islands are present. Most of the Ag is attached to the ascending substrate step edges. The perimeter shape of the deposit is still rather irregular and the average branch width has only slightly increased from b) to c).

The global morphology in d) is surprisingly very similar to the T = 80K structure, although grown at 400K. Again, small clusters appear on the substrate terraces. In contrast to the low temperature case, also a large amount of Ag is attached to the Pt step edges. The shape of this condensate

a) T = 80 K   b) T = 120 K

c) T = 220 K   d) T = 400 K

500 Å

Fig. 4.1:   a)-d) Overview of Ag submonolayer morphologies on Pt(111) as a function of temperature. The lateral scale of the four STM images is 0.2μm x 0.2μm. Coverage in monolayers: a) 2%, b)-d): 10%, used deposition flux R: a) $2x10^{-4}$ ML/s, b)-d) $1.1x10^{-3}$ ML/s.

phase is smooth in comparison to b) and c). The Ag monolayer is here already in thermodynamic equilibrium and the cluster phase on the terraces can be interpreted as a two-dimensional gas, as discussed in section 4.4.

The morphologies in a)-c), however, are kinetically determined structures. The transition observed in the three STM images can be understood in the framework of simple qualitative arguments. For this purpose, the three distances Λ_S, Λ_D and Λ_P are introduced:

- Λ_S is the average length of a substrate terrace

- Λ_P is the average diffusion length of an adatom condensed at the perimeter of an Ag island

- Λ_D is the average lateral diffusion length of a deposited adatom

where Λ_D is defined as follows: the deposited adatoms migrate on the surface and, when meeting each other, they can form critical nuclei, which subsequently can grow to islands by attachment of further adatoms. The diffusion of a Ag-adatom is terminated when it hits a critical nucleus or a stable island and condenses there. With increasing coverage the density of stable nuclei increases until a saturation density n_x is reached. From there, impinging Ag atoms condense solely at existing islands. At this state, they are migrating the average distance Λ_D and the saturation density n_x is roughly $1/\Lambda_D^2$, thus Λ_D is about half the average island separation distance.

At low temperatures migration is slow with respect to the deposition rate resulting in small values for Λ_D and a high density of stable nuclei. For T = 80K the saturated value n_x is reached after deposition of about 0.5% of one ML. Thus, the shown island density in a) (Θ = 2% of one ML) is saturated and reflects the distance $\Lambda_D \approx 25$Å.

With further increasing Λ_D, the density n_x decreases and larger clusters (islands containing several tens to thousands of atoms) can grow, the shape of which is now determined by the average diffusion length Λ_P of atoms adsorbed at the perimeter of the island. For small values of Λ_P the islands

grow ramified while for higher values of Λ_P the islands condense in compact shapes. The ramified case is shown at 120K where the separation between the islands ($\Lambda_D \approx 250\text{Å}$) is large compared to $\Lambda_P \approx 3\text{Å}$. This enables the growth of large dendritic islands.

At even higher temperatures, the average adatom diffusion length becomes of the order of the average length between two neighboring substrate steps Λ_S. Heterogeneous nucleation can take place at substrate steps and eventually for $\Lambda_D \gg \Lambda_S$ all islands grow from step edges, a phenomenon which is called "step flow" [Bur 51]. The perimeter shape of these islands is still determined by the magnitude of Λ_P, and can be irregular or smooth. At $T = 220K$, Λ_P is about 15Å and remains thus small with respect to the lateral scale of the deposit ($\Lambda_D \approx 600\text{Å-}700\text{Å}$), leading still to ramified structures.

The reason for the heterogeneous nucleation in the "step flow" regime is that ascending step edges act as sinks for adatoms. The potential barrier V_e at descending steps, however, controls the interlayer mass transport, as deduced in 2.3. For the low coverages in Fig. 4.1 landing events on top of the growing structures have negligible influence on the growing morphologies. But atoms interact from the beginning of deposition with the substrate steps. Their influence on an approaching adatom and therefore the form of the step edge potential can be deduced from the island distribution in the vicinity of descending steps (see e.g. [Gün 93]).

In the case of vanishing "Schwoebel"-barrier V_e, all material landing within a length comparable to Λ_D would be trapped by the step. Thus, a zone denuded of stable islands would be observable on the upper terrace. In Fig. 4.1 a), b) no depletion zone of islands along the descending substrate step edges can be found. Consequently, an additional barrier V_e is present, reflecting adatoms such that nucleation near the descending step remains

66

possible. Unfortunately, one cannot distinguish if the repulsive potential refers only to the Ag coated step or also to the pure Pt step edge because already at lowest coverages the steps exhibit a narrow seam of Ag due to the incorporation of diffusing atoms at ascending steps.

4.2 Low temperature nucleation and cluster aggregation

Experimental studies of nucleation phenomena on substrates have usually applied Electron Microscopy (EM) to monitor the density of stable island as a function of coverage and vapor supersaturation (see e.g. [Rob 64, Ker 79, Ven 84]). Also surface integrating techniques are widely used to extract island density data from nucleation experiments (see e.g. [Ern 92, Zuo 94]). STM studies in this field have mainly focused on homoepitaxial systems to study the "pure" aggregation kinetics (see e.g. Si/Si(001) [Mo 91], Fe/Fe(001) [Stro 93, Stro 94], Au/Au(100) [Gün 94]). In heteroepitaxy, studied here, the structural and chemical competition between adlayer and substrate adds as additional variable to the problem.

Studying nucleation demands the control of defects acting as preferential nucleation sites. Structural defects on the surfaces, like steps and vacancies, as well as adsorbates trap migrating atoms before they encounter a partner of their own. This defect density n_d leads to a minimum density of stable islands. If n_x is the nuclei density which would be obtained on a "defect-free" substrate, then, only for growth conditions with $n_d \ll n_x$, the measured island density data can be evaluated under the assumption of statistical aggregation of film atoms. This is the requirement to correlate the static measurement of island densities with the dynamic parameters of the atomic nucleation process.
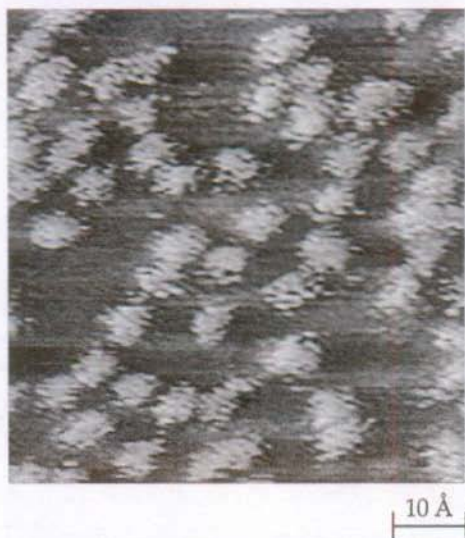
67

$$T = 35 \text{ K}, \quad \Theta = 0.1 \text{ ML}$$

10 Å

Fig. 4.2: Randomly distributed atoms at T = 35K. The average island size has been determined to $\bar{n}$ = **1.2±0.3** (island density ρ = 0.083 ML). The imaged round dots have a width of 4Å to 7Å. Image size: 68Åx68Å; used flux R = 1.1x10^{-3} ML/s.

STM is a suitable method to control the influence of defects on nucleation because it resolves imperfections on an atomic level and reveals their influence on the film morphology in real space. The best example has been given by Chambliss et al. [Cha 91]. Ni deposition at T = 300K on the reconstructed Au(111) surface results in an ordered array of Ni nuclei. Thus, in this case $n_d \approx n_x$ and the obtained film morphology reflects the natural "defects-lattice" of the substrate, i.e. the U-turns of the "herringbone" reconstruction (see e.g. [Bar 90] and also 6.1).

The Pt(111) surface is unreconstructed for T < 1330K [San 92] and in the absence of a supersaturated Pt gas-phase [Bot 93]. Thus on a well-prepared Pt(111) substrate the remaining defects are substrate steps. In the present

68

a) $\Theta = 0.007$ ML

b) $\Theta = 0.12$ ML
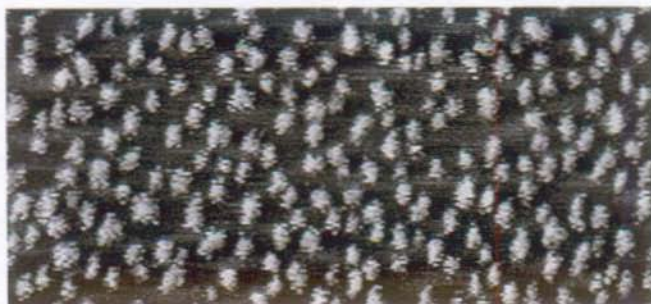
|—— 50 Å ——|

Fig. 4.3: a), b) Nucleation at T = 50K. Deposition of 0.7% and 12% of a monolayer leads to island densities of $\rho = 4.4\pm0.7\times10^{-3}$ ML and $\rho = 4.2\pm0.5\times10^{-2}$ ML, respectively. The average island size changes only slightly from $\bar{n} = 1.6\pm0.6$ in a) to $\bar{n} = 2.8\pm0.4$ in b) due to the coverage increase of a factor 17. Thus mostly dimers are formed under these growth conditions. Image size: 95Åx220Å, used flux R = 1.1×10^{-3} ML/s.

work island densities have been evaluated on terrace areas far away from steps. As seen in Fig. 4.1 b), c) it exists an upper temperature limit set by the miscut of the used single crystal where the influence of steps is no more negligible.

4.2.1 Transition from nucleation to growth

At the lowest substrate temperature studied (T = 35K) the lateral diffusion of deposited Ag atoms is frozen. After deposition of $\Theta = 0.1$ ML the average island size $\bar{n}$ turns out to be 1.2±0.3 atoms, as displayed in Fig. 4.2. The obtained imaging size of Ag atoms (4-7Å) is comparable to single Fe atoms on Pt(111) which have been imaged at T = 4K with a mean width of 7Å [Cro 93].

The onset of adatom mobility is shown in the two STM images of Fig. 4.3 displaying the film morphology for deposition at T = 50K. For the low coverages in a) the average island size turns out to $\bar{n} = 1.6\pm0.6$ atoms per island, and for the high coverage in b) to $\bar{n} = 2.8\pm0.4$ atoms per island. The increase of the coverage Θ by a factor of 17 corresponds quite closely to a factor of 10 increase in island density ρ. Thus we are in the coverage regime of nucleation. In this regime, diffusing Ag atoms find a second mobile partner to create a new nucleus more probably than to attach to an existing island. The island density does not increase proportionally with Θ because in b) partial growth occurs. On the other hand, these images show that dimers are stable at 50K, therefore the critical nucleus is a single atom.

In general, the size of the critical nucleus can be deduced from STM data by dividing the coverage Θ by the island density ρ at the coverage regime of pure nucleation. Values of island densities versus coverage are shown in a logarithmic plot in Fig. 4.4 for various temperatures. For T = 50K and 60K, the island densities show a linear increase up to the highest coverage investigated. This implies that at these temperatures, for coverages up to 0.1 ML, nucleation is not yet terminated, and arriving Ag atoms form new islands rather than attach to existing ones. The average size of these islands is approximately two Ag atoms (as can be seen from comparison with the
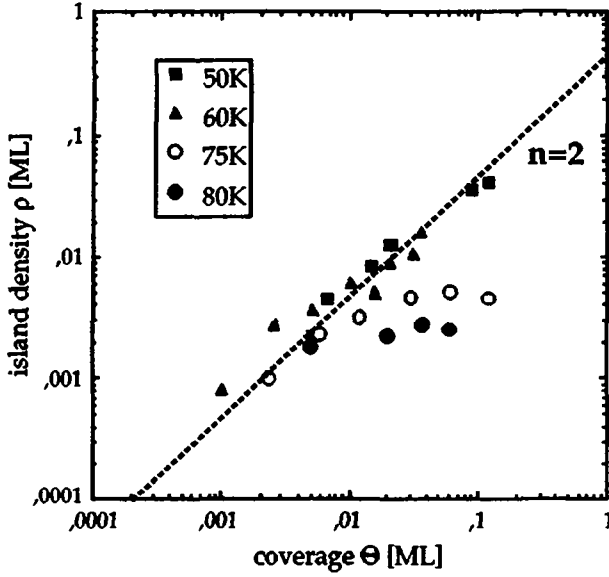
70

Fig. 4.4: Stable nucleus determination from island density versus coverage data for T = 50, 60, 75, and 80K. Details in text.

dashed line). At 75K, however, the data show that saturation starts at 0.6% of a monolayer; at 80K saturation occurs at coverages below 0.5% of a ML.

The island density ρ over the complete coverage regime from nucleation to growth was monitored at T = 75K. Four STM images are shown in Fig. 4.5 in order to illustrate how the island density as well as their shape changes from nucleation to growth. In a) and b), it is seen that on the average, the islands are still dimers (mean size $\bar{n}$ = 2.4±0.4 atoms and $\bar{n}$ = 2.6±0.5 atoms for a) and b), respectively), which means that they show the nucleation regime. The STM image in c), however, demonstrates the transition from nucleation to growth. Θ was increased by a factor of 5 with respect to b), which resulted in an increase in density by a factor of only 2 accompanied by an increase in the average island size to $\bar{n}$ = 6.4±1.1 atoms. Further increase
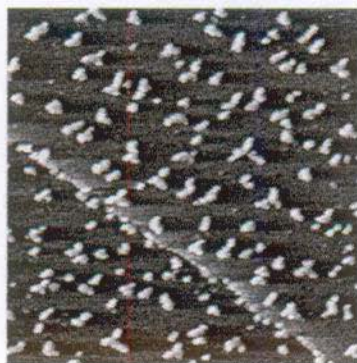
a) $\Theta = 0.0024$ ML

b) $\Theta = 0.006$ ML
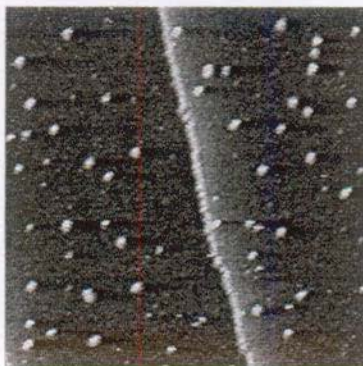
c) $\Theta = 0.03$ ML

d) $\Theta = 0.06$ ML

100 Å

Fig. 4.5: a)-d) Evolution of island shape, density ρ [ML] and average size $\bar{n}$ [atoms] as function of coverage at T = 75K. a) $\rho = 0.10\%$, $\bar{n} = $ **2.4±0.4**; b) $\rho = 0.23\%$, $\bar{n} = $ **2.6±0.5**; c) $\rho = 0.46\%$, $\bar{n} = $ **6.4±1.1**; d) $\rho = 0.50\%$, $\bar{n} = $ **11.9±2.0**. Image size: 420Åx420Å, used flux R = 1.1×10^{-3} ML/s.

of the coverage by a factor of 2 leads to exclusive island growth which results in $\bar{n} = 11.9 \pm 2.0$ atoms in d).

Thus, these images demonstrate the transition from pure nucleation, where the island density increases proportionally to coverage, to the transition

72

regime, where growth and nucleation occur simultaneously, and finally to the pure growth regime where the island density n_x has saturated. As can be seen from d), island growth leads to branching of the islands, caused by the low perimeter mobility for attaching atoms. This branching is not observed in c), which implies that it proceeds only if the islands have reached a certain size. This will be discussed in 4.3

4.2.2 Determination of the diffusion barrier E_D

The data in Fig. 4.4 showed that dimers are the stable nuclei for temperatures between 50K and 80K. From the cluster aggregation experiments described in 4.2.4 it turned out that dimers are indeed stable up to about 100-110K; only above this temperature the onset of diffusion and/or dissociation of Ag dimers is observed. It is therefore concluded that for the lowest temperatures dimers are the stable clusters and consequently monomers are the critical nuclei. This substantially simplifies the nucleation process to the encounter of two atoms and thus facilitates quantitative comparison with atomistic nucleation theories.

The main dependence of the saturation density n_x on the adatom diffusivity D and deposition flux R is understandable within an instructive "minimal model" [Vil 92]. A deposited adatom has a certain lifetime τ after which its diffusion is finished. The Einstein relation $\Lambda_D^2 \approx D \tau$ connects τ with the average lateral diffusion length Λ_D (defined in 4.1). The density ρ_1 of adatoms per adsorption site is the product of the incoming rate R by the lifetime τ. Thus, the order of magnitude for ρ_1 is given by $\rho_1 \approx R \Lambda_D^2 / D$. By means of ρ_1 the rate of pair formation, i.e. the nucleation rate $1/\tau_{nuc}$, can be estimated. Each adatom has a probability $\rho_1 \Lambda_D^2$ to meet another atom since it visits about Λ_D^2 sites during his 2D-random walk (Λ_D is measured in atomic distance). It follows that the nucleation rate $1/\tau_{nuc}$ is given by this

probability times the incoming rate R and therefore $1/\tau_{nuc} \approx R \rho_1 \Lambda_D^2 \approx R^2 \Lambda_D^4 / D$. This gives a first estimate of $1/\tau_{nuc}$.

Λ_D is also determined by the average separation distance between stable nuclei. Consequently, in the area Λ_D^2 only one pair of adatom nucleates which happens to first order during the time $1/R$ to complete one layer. Thus, the second rough estimate of the adatom lifetime is $1/R$ times the island density Λ_D^{-2} and therefore the nucleation rate results in $1/\tau_{nuc} \approx R/\Lambda_D^2$. Setting equal this formula with the first estimate of $1/\tau_{nuc}$ yields:

$$\frac{R^2 \Lambda_D^4}{D} \approx \frac{R}{\Lambda_D^2} \quad \Leftrightarrow \quad \Lambda_D^{-2} \approx n_x \approx \left(\frac{R}{D}\right)^{1/3}$$

In general, a scaling relationship $n_x \propto (R/D)^{\gamma}$ is obtained, where the exponent γ is a rational fraction whose value depends on the size and dimensionality of the critical nucleus and the presence or absence of desorption (see e.g. [Zan 93]). Thus, the saturation island density $n_x(R,T)$ contains direct information about the Ag adatom diffusion and should follow an Arrhenius law due to $D \propto \exp(-E_D/kT)$. The general formula (equation (2.15) in ref. [Ven 84]) gives for complete condensation (desorption is excluded at low temperature), for 2D islands and a critical nucleus size of i (binding energy E_i for the critical cluster):

$$n_x \propto \eta(\Theta) \, (R/v_0)^{i/i+2} \, \exp(\frac{E_i + iE_D}{i+2} / kT)$$

where $\eta(\Theta)$ is a slow varying function of the coverage (see also [Spi 83, Ven 87]). For Ag/Pt(111) and $T \leq 110K$ the simplest form of this equation is valid ($i = 1$, $E_i = 0$), i.e. $n_x(T) \propto (R v_0)^{1/3} \exp(E_D/3kT)$. Thus, in this case even the rough approximations in the above derivation leads to the proper exponent γ.
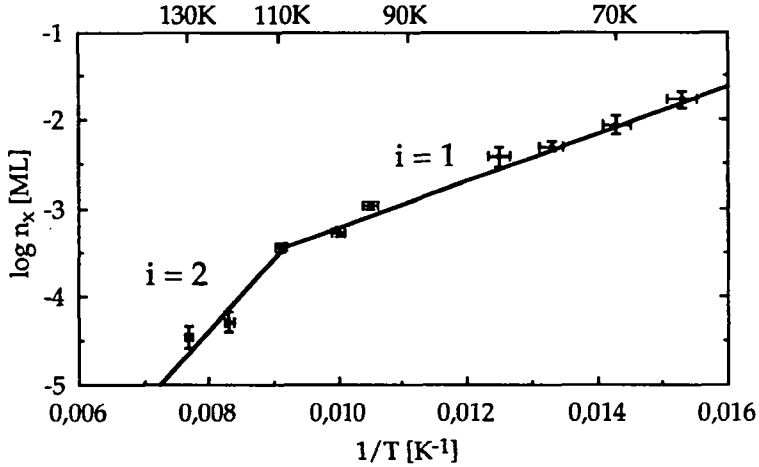
Fig. 4.6: Arrhenius plot of saturation island densities n_x obtained with a deposition flux of R = 1.1×10^{-3} ML/s. Up to T = 110K the critical nucleus is the adatom (i = 1) and the straight lines fitting the data allows to deduce the diffusion barrier E_D. The discontinuous change in the slope at T = 120K marks the transition to dimers (i = 2) as critical nuclei. Details in text.

Saturation island densities n_x versus the reciprocal of temperature are shown in Fig. 4.6 for the T range from 65K to 130K and for constant flux R = 1.1×10^{-3} ML/s. Between 65K and 110K the saturation island densities n_x lie on a straight line in the Arrhenius representation (labeled i = 1). This behavior allows one to determine rather precisely the migration barrier for Ag adatom diffusion on Pt(111). From the slope of the line that fits the STM data (65K $\leq$ T $\leq$ 110K) a migration barrier of E_D = 157±10 meV is obtained. From the intersection with the ordinate axis an attempt frequency 1×10^{13} Hz $\leq \nu_0 \leq 4 \times 10^{14}$ Hz is inferred. This number is in good agreement with the rate constant for the Ag desorption from Pt(111) (ν_0 = $1.5 \pm 0.5 \times 10^{14}$ Hz (see 2.3.7)), as expected [Lew 78].

The for i = 1 expected flux dependence $n_x \propto R^{1/3}$ has been verified for the two temperatures T = 80K and 110K as shown in Fig. 4.7. The measured
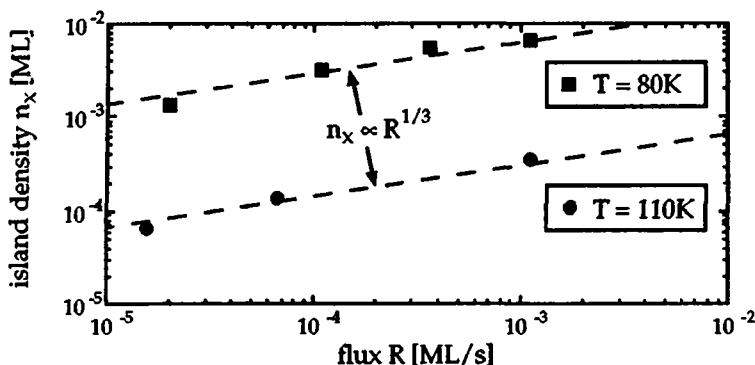
75

Fig. 4.7: Saturation island density n_x as a function of deposition flux R. The dashed lines have the theoretically expected slope for a critical cluster size i = 1.

migration barrier of E_D ≈ 157 meV is a rather reasonable value for diffusion of metal atoms on close-packed metal surfaces. Values of 156±22, 300, 269±4, and 150±100 meV have been obtained experimentally for self-diffusion on (111) surfaces of the fcc metals Rh, Ni, Ir [Ehr 91] and Ag [Jon 90], respectively.

The transition to the nucleation regime with trimers as stable nucleus is located between T = 110K and 120K. This is deduced by the facts that at T = 110K the data point in the Arrhenius-plot lies on the "dimer fit" line and the flux relation at this temperature is compatible to i = 1. Furthermore, at T = 120K the measured saturation island density n_x shows a substantial deviation to lower values. For T > 130K the increasing influence of the substrate steps and the low island densities avoided measurements of statistical relevant n_x-data. Thus, recording directly the Arrhenius behavior for i = 2 was not possible.

The "trimer fit" marked in Fig. 4.6 is obtained by estimation of the Ag-Ag binding energy on Pt(111) which enters as remaining unknown parameter

76

in the theoretical $n_x(R,T)$ curve for $i = 2$. The binding energy E_2 can be estimated to 320±30 meV from the assumption that at $T = 120K$ dimer dissociation becomes detectable at the time scale of the experiment (assuming an attempt frequency of $v_0 = 1 \times 10^{12}$ Hz). Using this E_2 value, the slope of the "trimer line" agrees with the remaining n_x-data points obtained at $T = 120K$ and $130K$. This dimer dissociation energy of Ag on Pt(111) compares to the values obtained for Ag on Ag(111) (0.25±0.05 eV experiment, 0.28 eV theory) [Jon 90]. On the other hand, $E_2 = 0.18$ eV has been calculated for Ag/Pt(111) by means of the embedded atom method (EAM) [Mas 93] (see Fig. 2.7 b)).

4.2.3 Simulation of the nucleation to growth transition

In the following the rate equations of nucleation are discussed and the results obtained by their numerical integration are compared with the experiment [Bru 941]. A linear plot of the island density n_x versus coverage at $T = 75K$ is shown in Fig. 4.8. The STM data are represented by dots with error bars, while continuous curves show the results from the calculations as discussed below.

In general, in a plot of island density versus coverage, the reciprocal of the initial slope directly reflects the size of the stable nucleus. For coverages below 0.006 ML, the densities (the first two data points) are on the initial slope of 0.5, indicating an average nucleus size of 2 (see dashed line). Above this coverage the gradual transition from nucleation to growth takes place up to 0.030 ML. At higher coverages, saturation sets in and island growth predominantly occurs.

The differential equations of nucleation, in this simple case where dimers are stable and desorption, as well as dimer migration, does not occur, are the following:

$$\frac{dn_1}{dt} = R - 2\sigma_1 Dn_1^2 - \sigma_x Dn_1 n_x - R(Rt - n_1) \qquad (1)$$

$$\frac{dn_x}{dt} = \sigma_1 Dn_1^2 - 2n_x(2\sigma_1 Dn_1^2 + \sigma_x Dn_1 n_x + R(Rt - n_1)) \qquad (2)$$

The terms in equation (1) describe the increase of the density of monomers due to the flux R, their decrease due to encounter of two diffusing atoms under creation of a dimer and disappearance of the two atoms, the decrease occurring when a monomer is captured by a stable island, and the decrease caused by atoms impinging on top of stable islands. In equation (2) the first term is the increase of density of stable islands n_x due to creation of dimers, whereas the second term in brackets represents its decrease due to coalescence (see eqns. (2.8), (2.9) and (2.11) in [Ven 84]). The diffusion is given by $D = \frac{1}{4}v_0 \exp(-E_D/kT)$ in unit cells per second. The lower curve in Fig. 4.8, labeled (i), shows the evolution of n_x as obtained from integrating eqns. (1) and (2) for Ag deposition onto the Pt(111) surface at T = 75K with the flux used in the experiments. The migration barrier of E_D = 157 meV derived from the STM data was used for the calculation. The attempt frequency has been set to $v_0 = 1.7 \times 10^{13}$ Hz in order to achieve the experimental saturation value for the island density n_x.

For curve (i), the capture rates σ have been interpreted in an atomistic model as cross sections for capture of diffusing atoms by islands or atoms. Their size-dependence was empirically determined to be $\sigma(n) := 2+n^{1/1.7}$, where n is the island size in number of atoms. Therefore monomers have σ_1 = 3 which comes from the fact that besides central impact also atoms approaching each other to one nearest neighbor distance are trapped. The cross section increases as the 1.7'th root of island size rather than the square root due to the fractal character of the islands (see 4.3). Accordingly in
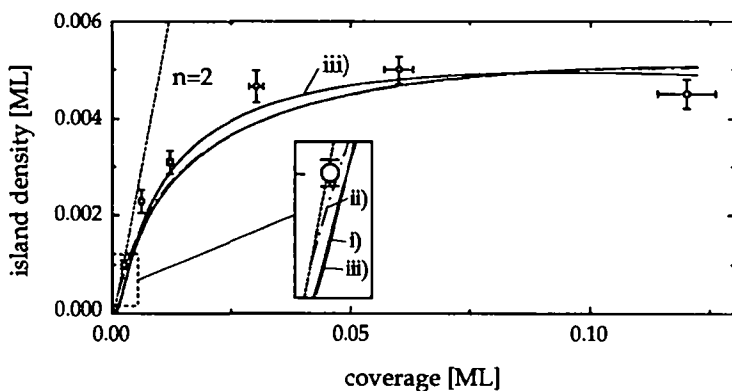
78

Fig. 4.8: Linear plot of the island density versus coverage at T = 75K compared with different solutions of the rate equations integration. Details in text [Bru 941].

equations (1) and (2), σ_x has been taken to be dependent on the average island size which is given by $n = (Rt-n_1)/n_x$.

The model simplifies the physical picture in so far as it assumes a homogeneous distribution of mobile monomers, which are then either trapped on their own or at condensed islands. However, it reproduces quite well the main features of the experiment. Curve (i) has an initial slope of 0.5 and it shows the gradual transition from nucleation to growth. This coincidence with experiment cannot be achieved if constant values for σ_x are used, hence the size dependence of σ_x is essential.

Compared to the experiment, however, curve (i) has a curvature which is too small. At the transition from nucleation to growth (0.01 - 0.03 ML) it lies below the experimental data and at the onset of coalescence, which was found between 0.06 and 0.12 ML, curve (i) continues to increase. The density of diffusing monomers has been assumed to be isotropic for the calculation. Actually, it decreases at the island edges due to capture there. For calculated

79

curve (iii) (upper curve in Fig. 4.8) this is taken into account and the capture rates are interpreted in the "classical" sense as the gradient of the monomer concentration at the island edges. These gradients were obtained by solving a 2D-diffusion equation in lattice approximation [Ven 73]. At the onset of nucleation, curve (iii) overlaps with curve (i). However, it raises more steeply and saturates earlier than curve (i), and thus shows better agreement with experiment.

For the very low coverages, it should be emphasized that this calculation gives the island densities during deposition, whereas the STM experiment samples the distribution a few minutes after deposition. It has been, therefore, calculated how the system develops if the flux is interrupted at given coverages and one waits until the island densities have reached their equilibrium value. At $T = 75K$ the system equilibrates in less than 10 s, and, therefore this equilibrium state is imaged with STM. The calculated equilibrium density of stable islands, n_x, which had developed 20 s after interrupting the flux, is shown in the dash-dotted curve (ii) as function of coverage. For this calculation, the choice between capture rates is of no importance because curve (i) and (iii) overlap at low coverages. Thus for simplicity, σ_x has been defined as in curve (i). Equilibration leads, for the smallest coverages, to a slightly higher island density, due to the initially high density of monomers which predominantly create new islands after the flux is interrupted. Correspondingly, curve (ii) is closer to the experiment for the very beginning of deposition. For coverages higher than 0.006 ML, however, it is seen that the island density imaged by STM is exactly that present during deposition (curves (i) and (ii) are in coincidence). This is due to the fact, that at coverages of 0.006 ML and higher, monomers remaining after deposition predominantly attach to existing islands rather than create new ones.
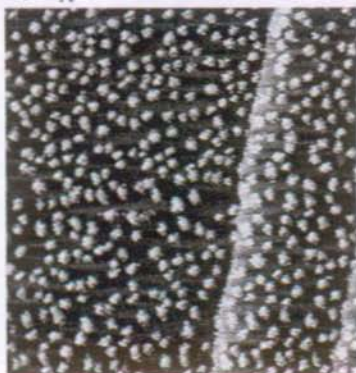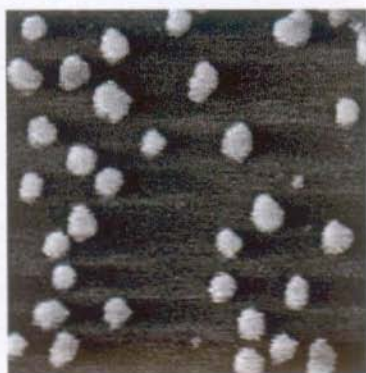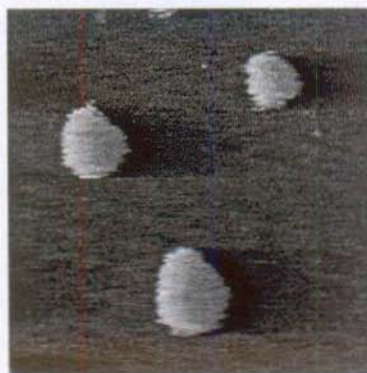
a) $T_A = 110$ K   b) $T_A = 140$ K
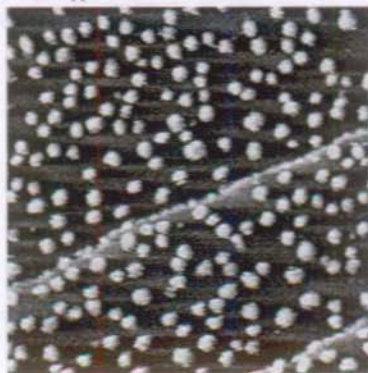
c) $T_A = 210$ K   d) $T_A = 250$ K

$\vdash$ 100 Å $\dashv$

Fig. 4.9:   a)-d) Cluster aggregation by annealing of low temperature
deposited Ag atoms and small clusters ($\bar{n}$ = 2-3 atoms). The total
coverage is always Θ = 0.1 ML and the deposition temperature is in a),
b) T = 35K and in c), d) T = 50K, respectively. a) $T_A = 110$K, $\bar{n}$ = 6.0±0.5;
b) $T_A = 140$K, $\bar{n}$ = 14±1.0; c) $T_A = 210$K, $\bar{n}$ = 120±10; d) $T_A = 250$K, $\bar{n}$ =
650±50. Image size: 400Åx400Å, used flux R = 1.1x10^{-3} ML/s.

The fact that the STM experiments show no difference in the densities

obtained during deposition, at least for saturation, in the whole temperature

81

range addressed in Fig. 4.6 is important to note. This is the condition to extract diffusion constants from saturation island densities, because the flux is the only parameter introducing time.

4.2.4 Cluster aggregation

The approximation that clusters are immobile and their diffusion does not contribute to the nucleation and growth process is no more suitable at higher temperatures. This is demonstrated by the cluster aggregation experiment illustrated in Fig. 4.9. Small clusters (as shown in Fig. 4.3 b)) are used to form larger clusters by thermally activated coalescence. In contrast to the direct growth experiment the islands have compact forms reflecting the substantially different formation process. For the images a) and b) also a narrow size distribution can be deduced from the STM imaging, while for the larger islands in c) and d) the size distribution is broader (see also Fig. 4.18 a), b)).

The aggregation process uses as initial condition Ag atoms or clusters formed by deposition of $\Theta = 0.1$ ML at $T = 35K$ ($\bar{n} \approx 1$ atom) and $T = 50K$ ($\bar{n} \approx$ 2-3 atoms), respectively. In the following growth step the film structure is annealed to and imaged at the temperature T_A to evaluate the island density ρ as a function of T_A. The obtained dependence $\bar{n}(T_A)$ is shown in Fig. 4.10 revealing an exponential increase of the average island size $\bar{n}$.

The data in Fig. 4.10 show hardly a difference between the two experiments. Only for $T_A < 100K$ the smaller initial cluster distribution ($T = 35K$) shows a more continuous increase with respect to the larger one ($T \approx 50K$) which stays nearly constant up to $T_A = 100K$ (from $\bar{n} = 2.8\pm0.4$ at 50K to $\bar{n} = 3.2\pm0.6$ at 100K). This indicates the stability of the dimer up to about 100-110K, even on the long time scale of this annealing experiment. This is in good
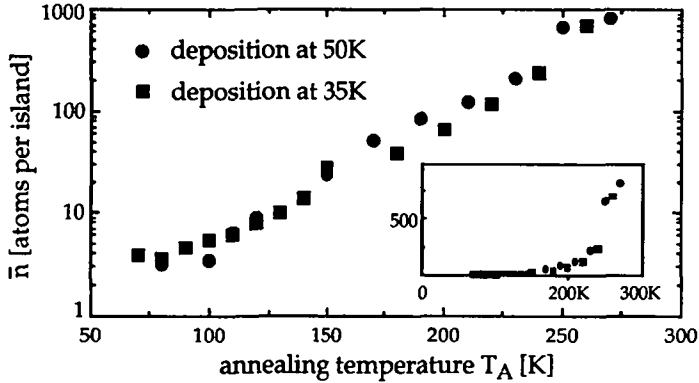
Fig. 4.10: Cluster aggregation: average number $\bar{n}$ of atoms per island versus T_A for Θ = 0.1 ML deposited at T = 35K and T = 50K, respectively. Inset: same plot, but with a linear vertical scale showing the exponential $\bar{n}$ increase. Details in text.

agreement with a critical cluster size i = 1 up to T = 110K, that was found in the direct growth experiments (see 4.2.2).

Two microscopic processes contribute to the aggregation dynamics in this annealing experiment:

1) the diffusion of small clusters

2) the thermal dissociation of clusters

The second process creates mobile adatoms or, again, small clusters leading to material exchange between the islands. The diffusion of clusters results in direct coalescence of the aggregates.

For Ir_x-clusters on Ir(111) the diffusion of clusters is observed prior to dissociation if the substrate temperature is increased. The measured diffusion barriers increase with the cluster size x and are about a factor 2-3 higher (for $x \leq 5$) than the Ir adatom barrier E_D [Wan 90]. Molecular

83

dynamics simulations for Ag/Pt(111) predict diffusion barriers for the dimer and trimer 1.5-2 times as high as for the adatom (E_D^1 = 60 meV, E_D^2 = 90 meV, E_D^3 = 130 meV) [Bla 92, Mas 931]. The calculated dissociation energies E_i (see Fig. 2.7 b)) are about twice as high as the corresponding diffusion barriers E_D^i.

Thus, it is likely to assume that at the onset of the cluster aggregation experiment the cluster diffusion dominates their dissociation. On the other hand, the dimer diffusion barrier E_D^2 can be estimated by scaling up of the measured adatom barrier of Ag, E_D^1 = 157 meV, with the ratios E_D^2/E_D^1. This leads to $E_D^2 \approx 250$ meV (measured Ir(111) ratio), $E_D^2 = 235$ meV (calculated Ag/Pt(111) ratio), and $E_D^2 \approx 335$ meV by using the calculated ratio E_D^2/E_D^1 for Ni/Ni(111) [Liu 92]. These values have to be compared with the above estimated dimer binding energy $E_2 = 320\pm30$ meV. Considering the uncertainty of the preexponential factors for the dimer diffusion /dissociation, a clear separation between the two processes is not possible.

The Arrhenius-plot of the island density data in Fig. 4.10, i.e. $\ln\rho(T_A)$ versus $1/T_A$, has a curved contour. Thus, by assuming $\rho(T_A) \propto \exp(-E_A/kT_A)$, the slopes in the different T_A ranges leads to activation energies E_A between $\approx$ 10 meV and 120 meV at the lowest and highest temperatures, respectively. Between $T_A \approx$ 100K-170K the average slope yields $E_A \approx 60$ meV. It demands further investigations, by variation of the total coverage Θ, finer temperature distances between the measured $\rho(T_A)$ values, and a better STM resolution to distinguish the different cluster sizes, to establish a relation between this values and the microscopic processes involved.

The inset in Fig. 4.10 shows a linear plot of $\bar{n}(T_A)$ revealing a drastic increase of the islands sizes around $T_A = 200$K. This indicates that from this temperature on a 2D-adatom gas of reasonable density exists between the

islands due to evaporation of atoms from the step edges. This Ostwald-ripening [Ost 00] is further discussed in 4.4.1. The reduction of the density of low temperature deposited Ag islands by coarsening effects starts also on the Ag(111) surface at about $T_A = 200K$ [Ros 93].

4.3 Fractal growth shapes

The word "fractal" has been introduced by Mandelbrot to represent shapes or phenomena having no characteristic length, i.e exhibiting the property of self-similarity [Man 82]. One characteristic of these objects is that their mathematical description demands the introduction of a fractional dimension in order to express their "infinite ramification" (see e.g. [Fal 902, Tak 90]). For fractal patterns observed in nature the fractional scaling is naturally limited: at small lengths by the finite size of the building matter, as well as at larger lengths by the finite size of the whole pattern [Sta 86, Vic 89].

Fractal growth forms in metal-on-metal epitaxy have been first reported by Hwang et al. [Hwa 91]. Au deposition at $T \approx 300K$ on the Ru(0001) surface produces irregular shaped islands exhibiting over two orders of magnitude a mass distribution described by a Hausdorff or fractal dimension of $D = 1.70\pm0.02$. Annealing of the film to $T = 650K$ smoothes the borders of the Au aggregates and compact shapes are formed, proving the kinetic origin of this phenomenon. Indeed, in the thermodynamic limit the length of the island border is minimized to reduce the free step energy, i.e trivial Euclidean dimension ($D = 2$) has to result.

The microscopic origin of fractal shapes in metal-on-metal epitaxy is the low mobility of atoms attached to the island perimeter. "Low" has to be seen in comparison with the lateral scale of the growing structures. The necessary

a) $\Theta = 0.037$ ML
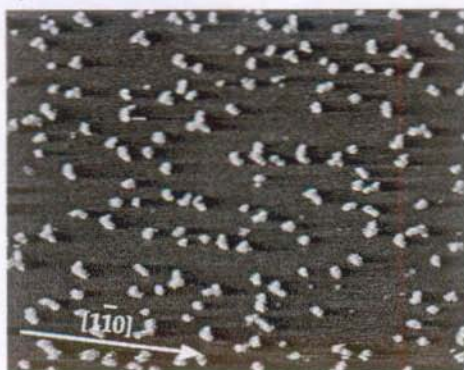
b) $\Theta = 0.12$ ML

Fig. 4.11: a), b) Shape of small Ag_n cluster grown at T = 80K. The average island size is $\bar{n} = 13\pm2.5$ in a) and $\bar{n} = 21\pm3.5$ in b). While in the upper image spherical and ramified clusters coexist, all islands in the lower image have a branched structure. Image sizes: a) 615Å x 480Å, b) 615Å x 195Å; used flux R: a) 3.7x10⁻⁴ML/s, b) R = 3.6x10⁻³ML/s.

requirement is therefore given by $\Lambda_P \ll \Lambda_D$, i.e. a large difference of the two relevant diffusion lengths determining the shape and size of growing islands (see 4.1). It seems to be a general phenomenon that this kinetic condition is fulfilled for metal atoms deposited on (111) surfaces of fcc-metals due to the substantially lower diffusion barrier E_D with respect to the step edge diffusion barriers $E_e^{A/B}$ (see e.g. [Ehr 91]).

4.3.1 Branching of small clusters

Already in Fig. 4.5 it has been shown that after reaching a certain size (between 6 to 12 atoms) the Ag islands exhibits a ramified shape. Fig. 4.11

displays in detail the initial branching of the clusters at $T = 80K$. The smaller islands in a) are imaged almost spherical and from their shape and the island size distribution ($\bar{n} = 13\pm2.5$) it can be concluded that those small islands are heptamers, i.e. they constitute the seed particles of branching. The largest islands are forming Y's with arms 120° apart. This anisotropy in growth is even better seen for somewhat larger clusters ($\bar{n} = 21\pm3.5$) as shown in b). At this larger average size all islands exhibit arms pointing perpendicularly to the close-packed $\langle 1\bar{1}0 \rangle$ directions of the substrate.

Ag atoms arrive from random directions at the seed-heptamers but the branching takes preferentially place in only 3 of the 6 $\langle 11\bar{2} \rangle$ directions, thus is linked to the trigonal symmetry of the Pt(111) surface. This result is not surprising since the perimeter diffusion governs the island shape and this anisotropy reflects therefore a difference between the step edge diffusion along A- and B-steps. This is further supported by the fact that all island arms in Fig. 4.11 point in the same direction. In Fig. 4.12 the growth directions of the Y's are compared with the known equilibrium form of vacancy island on the Pt(111) surface [Mic 912, Mic 911]. This calibration shows that growth of the Y-arms proceeds preferentially in the three $\langle 11\bar{2} \rangle$ directions which are perpendicular to the A-steps of the substrate.

To decide whether the A-step direction of the substrate coincides with the A-steps of the seed cluster requires the knowledge of the Ag adsorption site. i.e. if the heptamer is absorbed on the hcp- or fcc-sites. As mentioned in 2.2.1, at least for $T > 300K$ Ag adsorbs pseudomorphically on the Pt(111) surface, thus on fcc-sites [Ran 94]. A first hint that this is also valid for smaller Ag_n-clusters is given by the STM imaging of Ag attached to Pt-steps. In Fig. 4.12 even small islands are dislocation-free attached to the neighboring Pt-layer at ascending steps. The STM images would reveal an
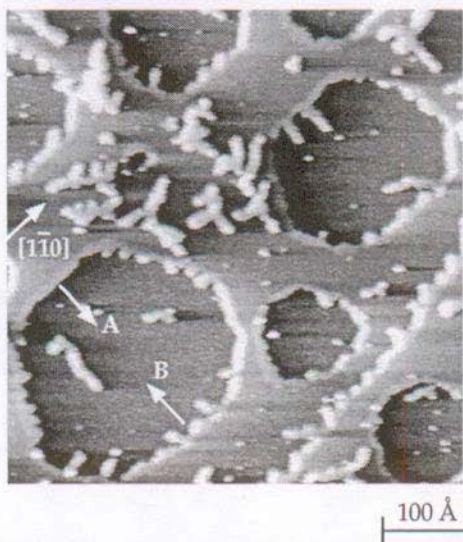
87

T = 100 K, Θ = 0.1 ML

100 Å

Fig. 4.12: Calibration of the branching directions. Sputtering of ≈ 0.5 ML at 600K and annealing to 700K for 10 min creates equilibrated vacancy islands on the Pt(111) surface. The short sides of the hexagons are A-steps, while the longer ones are B-steps [Mic 912, Mic 911]. Subsequent deposition of 0.1 ML Ag at T = 100K reveals that the Y-shaped Ag islands as well as Ag attached to Pt-steps grow preferentially perpendicularly to the A-steps. Image size: 520Åx520Å, used flux R = $1.4x10^{-3}$ ML/s.

undulation if there was a stacking fault. However, the fact that the Ag islands are imaged as a perfectly flat layer where they are connected to Pt-steps indicates the absence of a stacking fault and thus the fcc-adsorption site also for small Ag_n-clusters.

Two additional arguments already mentioned in 2.3.2 support the fcc site: in the two independent calculations of Ag diffusion on Pt(111) the fcc-site turns out as energetically preferred adatom adsorption site. For Ir/Ir(111) larger clusters (n≈7) exhibit the stacking of the complete monolayer (fcc) although the adatom occupies the "wrong" site (hcp). Since in the case of
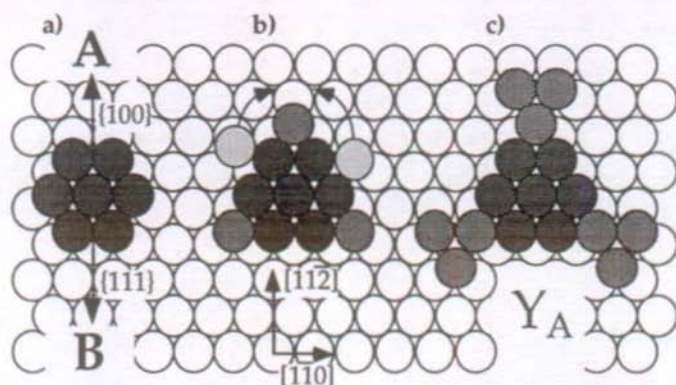
Fig. 4.13: Microscopic model of the initial branching mechanism. Details in text.

Ag/Pt(111) even the adatom seems not to occupy the hcp-site, it is thus very unlikely that small Ag structures grow with a stacking fault (hcp), while the complete monolayer at higher temperatures continues the substrate stacking (fcc).

In Fig. 4.13 the branching mechanism of the fcc Ag islands is illustrated. The explication is based on the requirements necessary for a preferred growth of the observed Y_A-clusters (sketched in c)). Y-branching of the heptamer is possible in two ways: by adding Ag adatoms to its A-steps or to its B-steps. Growth perpendicular to the A-steps demands that atoms which have condensed at the B-steps diffuse in the A-positions. The Ag_{10}-aggregate is then oriented in the A-directions and furthermore exclusively bound by B-steps as sketched in b). The second requirement to grow a stable expansion in A-direction is that two diffusing perimeter atoms have to meet each other at the aggregate's corners (as illustrated in b)). Such an event, however, becomes more probable the more diffusing atoms are present

similarly at the island perimeter. Their quantity is therefore directly related to the impinging flux on the Ag_{10}-aggregate.

The first requirement demands a faster step edge diffusion along the B-steps at least for the heptamer. The second step of the Y_A-branching is important to explain the flux dependence of the larger island shapes and is discussed below (see 4.3.3).

A faster step edge diffusion along the B-step is contrary to what is known for homoepitaxial systems. Pt/Pt(111), Rh/Rh(111) and Ni/Ni(111) all have lower diffusion barriers along A-steps [Ehr 91] and accordingly, for homoepitaxy of Pt, preferred growth is observed perpendicular to B-steps [Mic 93] (for the low temperatures in consideration here). This difference might be due to strain in the (1x1) Ag islands, which preferentially is relieved at steps where the atoms have lower coordination. This might shift their position apart from the ideal hollow site and/or modify the electronic structure at the step. Both are expected to have consequences on the migration of a Ag atom along a step.

4.3.2 Large fractal islands

The two STM images in Fig. 4.14 a), b) show large Ag islands grown at T = 110K and T = 130K, respectively. The insets display film morphologies grown at the same temperature but with a two orders of magnitude different deposition flux R. Thus, the comparison between a) and b) points out the flux dependence of the obtained structures. Since the island density n_x depends also on the flux R, the sizes of the islands in a) grown at 110K with the low flux is comparable to those in b) obtained at T = 130K with the high flux. The two diagrams in c) and d) show the evaluation of fractal dimensions and are discussed below.

a) T = 110 K   b) T = 130 K
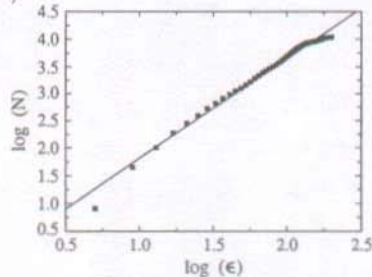
[1̄10]

[1̄10]

300 Å

c)
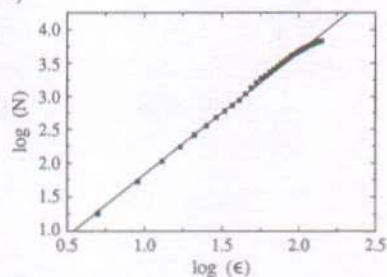
d)

Fig. 4.14: a), b) Transition between fractal (randomly ramified) in a) and dendritic shape in b) of large Ag islands obtained by **variation of the deposition flux R** by two orders of magnitude. Coverage: always Θ = 0.12 ML. Image sizes in a), b) 1230Åx1230Å, insets: 530Å x 330Å in a) and 830Å x 520Å in b).

a) T = 110K: **low flux** of 1.6×10^{-5} ML/s, inset: small dendritic islands obtained at high flux of 1.1×10^{-3} ML/s.

b) T = 130K: **high flux** of 1.1×10^{-3} ML/s, inset: large fractal island obtained at low flux of 1.6×10^{-5} ML/s.

c), d) Evaluation of the fractal dimension [Rom 93]. c) Ag aggregate ($\approx$ 4000 atoms) on the right bottom in a) obeys a fractal dimension of D = 1.78 for the straight line fitted to the data. ϵ is the border length of boxes in pixel (1 pixel corresponds to 2.3Å^2), N is the number of pixels where the surface is covered by Ag. d) Mass-length scaling of the biggest dendrite ($\approx$ 9000 atoms) in b).

91

In a) large clusters (~3000 Ag atoms) with an open ramified structure are formed by using a very low Ag flux of 1.6×10^{-5} ML/s. The branches of the clusters frequently alter their direction of growth and thus show no long range correlation with the trigonal substrate symmetry. The arms thickness is almost constant over the entire aggregate being only 3 ± 1 atoms as determined from the total branch length observed and the total amount of deposited material. The branches are imaged 14 ± 3Å wide which is consistent with their actual width if the finite curvature of the STM-tip is taken into account.

A drastic change of the aggregate patterns is observed upon the use of a by two orders of magnitude increased flux. This is demonstrated in b) showing Ag-clusters (the biggest consists of ~9000 atoms) grown at T = 130K with the increased flux. A nice dendritic pattern is observed with the characteristic back-bones, whose orientation is determined by the crystalline anisotropy of the substrate. In snow-flake terminology this dendrite is of the P2a type (plane P, with irregular number of branches 2, three branched a) [Nak 54] The three axes of preferred growth of the dendrite are oriented along the crystallographic $\langle 11\bar{2} \rangle$ directions of the substrate, as seen for the small Ag clusters. The arm thickness (imaged width 18 ± 5Å) has slightly increased to 4 ± 1 atoms with respect to a)

The insets in a) and b) show that also at T = 130K randomly ramified patterns with no preferred orientation result through application of the low flux used in a). On the other hand, dendrites also grow at T = 110K upon deposition with the high flux used in b). Therefore the parameter that drives the crossover from ramified to dendritic patterns is the deposition flux, i.e. the growth speed of the aggregate.

In order to prove the fractal nature of the grown Ag structures in a) and b) their fractal dimension has been evaluated [Rom 93]. For this purpose the box-counting method has been used, i.e. the mass-length scaling is measured by dividing the pattern of the clusters into boxes of size ε. The log-log plots of the occupancy number $N(\varepsilon)$ as a function of ε shown in c) and d) measure the mass fractal dimension D, i.e. $N(\varepsilon) \propto \varepsilon^{-D}$ (see e.g. [Mea 86, Tak 90, Fal 902]). The investigation of the fractal character yields scaling over two orders of magnitude. While the qualitative growth form has changed drastically due to the different used flux R in a) and b) the fractal dimension is nearly unaffected. The randomly ramified aggregates have an average fractal dimension of $D = 1.76 \pm 0.07$, while for the biggest cluster in b) $D = 1.77 \pm 0.05$ is obtained.

The classical diffusion limited aggregation (DLA) model [Wit 81, Wit 83] is the direct theoretical counterpart to metal-on-metal epitaxy in the case where the growth kinetics includes the relation $\Lambda_P \ll \Lambda_D$ [Hwa 91]. DLA models generate fractal clusters by depositing randomly on a lattice diffusing particles which stick irreversibly to the perimeter of the growing aggregate. Fig. 4.15 shows an example where the screening effect of this computer code is illustrated. To produce fractal structures the 2D-random walk of the particles towards clusters and therefore the growth dynamics are essential. The growing tips collect all material coming from outside and screen by this mechanism the center of the cluster. In the simpler Eden model, on the other hand, particles are randomly placed on the non-occupied neighbor sites of a growing cluster without a preceding diffusion. This mechanism creates compact aggregates with a fractal dimension equal to the dimension of the investigated space [Jul 85].
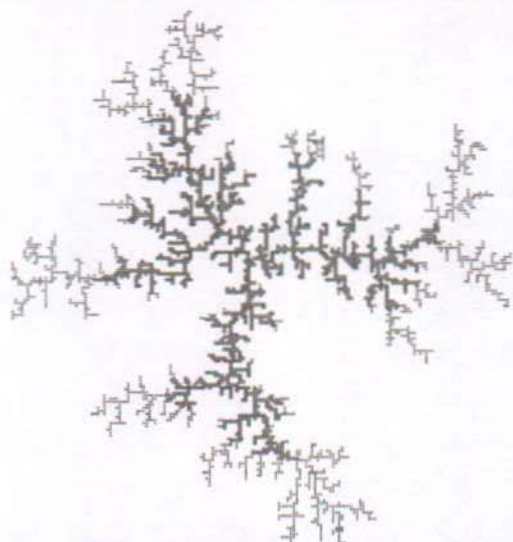
Fig. 4.15: Screening effect of the diffusion-limited aggregation (DLA) model. In the image of the DLA cluster (3000 particles) the first 1500 particles to attach to the aggregate are open circles, the rest are dots. The cluster had been simulated on a square lattice (from [Wit 83]).

The comparison of the theoretical cluster in Fig. 4.15 and the low flux grown Ag aggregates at $T = 110K$ in Fig. 4.14 a) indicates already that the experiment is close to the hit and stick mechanism of the DLA model. Quantitatively it turns out that both measured D values are in good agreement with the DLA simulations for the relatively small cluster sizes under consideration here. The simulated values for dendritic and fractal objects is $D = 1.7$ in two dimensions. Only at very large sizes of more than 10^4 particles the asymptotic limit is $D = 1.5$ for dendrites with large anisotropy whereas it remains $D = 1.7$ for the classical DLA fractals [Mea 86, Nit 86, Mea 88]. Thus, the fractal dimension D is an insensitive number concerning the observed transition between randomly ramified fractals at low flux and the dendrites at high flux.

4.3.3 Anisotropy and growth speed

The classical DLA algorithm always produce ramified fractal patterns, no matter whether they are carried out on a lattice or on a flat surface (off-lattice-DLA) [Mea 83, Eck 90]. Dendritic structures are obtained in DLA-like models by different methods of "noise reduction" (e.g. reduction of the sticking probability) and the resulting cluster shapes reflect therefore the symmetry of the underlying lattice [Mea 86]. Accordingly, also transitions between fractal and dendritic patterns are observed by "tuning" of these mechanism, e.g. by increasing the "noise-reduction" [Mea 87] or the curvature dependent sticking probabilities of the arriving particles [Vic 89]. A direct relation of these models to the experiment in order to reveal the microscopic mechanism which amplifies the lattice symmetry to the global shape of the growing clusters is hardly to obtain.

Comparison with experimental work on fractal growth phenomena shows that similar transitions of fractal pattern have been observed: increasing the growth speed (Zn^{2+} concentration and voltage) in electrochemical deposition resulted in transition from fractal to dendritic patterns [Saw 86, Gri 86]. In the propagation of a low viscous medium into a high viscous one in a Hele-Shaw cell [Hel 98], from certain propagation speeds on, viscous fingering occurs (Saffman-Taylor instability [Saf 58]). The dynamics is dominated by tip bifurcations which lead to randomly branched structures. When anisotropy is introduced into these systems, either by scratching a lattice into one of the glass plates of the Hele-Shaw [Ben 85, Hor 87] or by use of a liquid crystal as high viscous medium [Buk 86] a transition from randomly ramified to dendritic patterns is found. This transition takes place upon increase of the expansion rate, which, again is in accordance with the results presented above. The hydrodynamic experiments, however,

demonstrate that anisotropy is a necessary condition for dendritic growth, a result which has also been found in statistical mechanics simulations of these experiments [Nit 86, Nit 87]. Therefore, a transition from fractal to dendritic patterns is obtained when anisotropy dominates the noise.

The microscopic mechanism that establishes anisotropy in the case of Ag/Pt(111) is given by the different step edge diffusion parameters for A- and B-steps. Two experimental observations enable a connection between the above discussed Y_A branching mechanism of small Ag_n-clusters with the pattern transition of the large islands obtained by variation of the growth rates:

1) The directional anisotropy is equal for the large dendrites and the small Y_A's. Both grow perpendicularly to the A-steps.

2) The arm widths of the large A islands in the T range between 110K and 130K are comparable (within a factor 1.5-2.0) with the branch size of the Y_A's.

From both observations a mechanism similar to the one illustrated in Fig. 4.13 has to be responsible for the oriented shape of large islands by using a high flux. After the "orientation" of the small clusters due to the anisotropy of the step edge diffusion the further step of the Y_A-formation was the growth of a stable extension by meeting of atoms at corners pointing in the $\langle 11\bar{2} \rangle$ directions. These corners are formed by two close-packed steps running along a $\langle 1\bar{1}0 \rangle$ direction. The number of atoms present at both steps determines the probability of such a "meeting event" and therefore increases for higher impinging flux. On the other hand, the mean free path of a diffusing perimeter atom increases only with the square root of the diffusion time (Einstein-relation). Thus, even when each diffusing step atom has more time to grow an extension (low flux) the probability of a

96

"meeting event" is to first order determined by the linear time dependence of the step atom "production rate", i.e. is directly related to the impinging flux.

At the high flux used for the morphologies in Fig. 4.14 there are on the average about 100 atoms arriving per second at the aggregate's perimeter, whereas there is only about one per second at the low flux. Therefore the probability for two atoms to meet at a corner is larger at increased flux, and, due to faster migration along B-steps, also much more probable at those corners pointing in A-direction. Thus dendrites with trigonal growth perpendicular to A-steps are formed for high flux. At low flux, on the other hand, interaction of two diffusing particles at the island corner is less probable and predominantly single non interacting mobile atoms are present at the step. Therefore the anisotropy looses more of its importance in favor of noise and the aggregate grows randomly.

This kinetic growth effect caused by variation of the deposition flux is only obtained in a small temperature range. Growing small clusters at T = 80K produces even for the low flux preferred directions. This is in accordance with the expectation that a kinetic difference between A- and B-steps becomes more pronounced at lower temperature. On the other hand, higher temperatures suppress the anisotropy since a globally higher mobility covers the difference between the two step orientations. This can be seen in the inset of Fig. 4.18 a) showing a fractal Ag island grown at T = 160K using the high flux. Thicker island branches have developed (8±1.5 atoms wide) and the global morphology of the aggregates does no more reflect the symmetry of the substrate.

97

4.3.4 Estimation of the step edge diffusion barriers

Fig. 4.16 displays the island branch width as a function of growth temperature. The average branch width $\overline{w}$ increases obviously with T (note the different lateral scale in a) with respect to b)-d)). At T = 300K on substrate terraces as wide as Λ_S = 2000Å no homogeneous nucleation occurs and Ag grows from the ascending steps. The STM image in d) shows that also in the "step flow" regime the ramified shape of the deposit remains recognizable up to Θ = 0.4 ML. The average branch width at room temperature and Θ = 0.1 ML is $\overline{w}$ = 37±6 atoms and increases only by a factor of 2 for the four times higher coverage in d) ($\overline{w}$ ≈ 75±10). This non-linear behavior of $\overline{w}(\Theta)$ can be related to the screening effect of fractal growth and shows that also at higher temperature (with active step edge diffusion) the aggregate edges are partially screened by the growing tips.

It is instructive to compare the room temperature aggregation of the systems Ag/Pt(111) and Au/Ru(0001). In the latter case, fractal islands (also not correlated to the orientation of the substrate) could be grown on Λ_S > ≈ 1500Å wide terraces by homogeneous nucleation (favored by a factor 27 higher deposition flux with respect to Fig. 4.16). The observed thickness of the Au branches is about 100Å - 150Å (≈ 37- 56 atoms) at Θ = 0.15 ML (see Fig. 1 (b) in ref. [Hwa 91]) and thus within the error margin comparable to Ag/Pt(111). This suggests that also for Au/Ru(0001) fractal aggregates with a branch thickness of only a few atoms should grow at lower temperatures ("atomic" DLA).

In the following the measured function $\overline{w}(T)$ (at constant deposition flux R and coverage Θ) is quantitatively compared with two fractal growth models of Pimpinelli et al. [Pim 93] and Bartelt and Evans [Bar 941].

a) T = 160 K   b) T = 200 K

800 Å

c) T = 240 K   d) T = 300 K

1600 Å
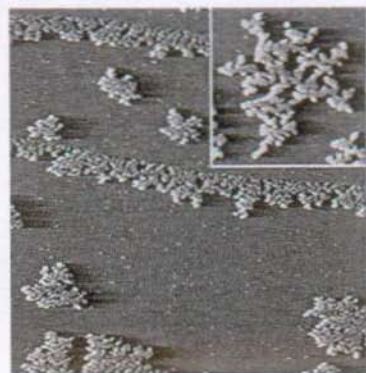
Fig. 4.16: a)-d): Island branch widths as a function of growth temperature T (constant deposition flux R = 1.1x10^{-3} ML/s). The coverage is in a)-c) Θ = 0.1 ML and in d) Θ = 0.4 ML. The inset in a) shows an enlargement of an Ag aggregate grown at T = 160K. Average arm width [atoms] a) $\overline{w}$ = 8±1.5, b) $\overline{w}$ = 13±2.5, c) $\overline{w}$ = 18.5±2.5, d) $\overline{w}$ = 75±10 for Θ =0.4 ML. Image sizes: a) 2450Åx2450Å, Inset: 460Åx460Å , b)-d) 4900Åx4900Å.

Both theories are based on the Mullins-Sekerka shape instability for diffusion mediated processes [Mul 63]. Unlike classical DLA-models the

99

perimeter mobility of the attaching particles is not frozen but permitted by a finite step edge diffusion. Atoms adsorbed at the island perimeter can either "scan" the step edge and attach to a kink site, or can meet another mobile edge adatom nucleating new kinks (see also 2.3.5). The relative probability of these events depends on the lateral size L of the step and the impinging flux I on the island.

The basic idea of both models is to connect the hop rate $h_e = \frac{v_e}{2} \exp(-E_e/kT)$ of mobile edge atoms, i.e. the diffusion constant D_e in atomic units, with the parameters I and L to determine the critical step length L_{cri} where a shape instability of the growing islands occurs. This is the case, when nucleation events dominate the slow edge diffusion and the step grows perpendicularly. Bartelt and Evans [Bar 941] propose the instability criterion: $\tau_i \approx \tau_e$ where τ_i is average time between two impinging events, i.e. $\tau_i = 1/I$, and τ_e is the average time for an atom to "scan" the step length L. Using the Einstein relation $L^2 \approx h_e \tau_e$ it follows $\tau_e \sim L^2/h_e$ and so, for the critical length L_{cri}:

$$\tau_i \approx \frac{1}{I} \approx \frac{L_{cri}^2}{h_e} \approx \tau_e \quad \Leftrightarrow \quad L_{cri} \approx \sqrt{\frac{h_e}{I}}$$

This result is supported by numerical simulations performed by Bartelt and Evans [Bar 941] leading to the empirical formula $L_{cri} L_w \approx 1.7\sqrt{h_e/I}$, where L_w is the average branch width of the computer generated fractals. Thus, the branch width of the fractal islands reflects directly the size of the "fractal grain" for the island ramification. Pimpinelli et al. [Pim 93] predict a different dependence $L_{cri} L_w \approx \sqrt[3]{h_e/I}$ by introducing a density ρ of atoms at the step length L and calculation of the pair formation probability (the derivation is similar to the one presented in 4.2.2).

The average branch width $\overline{w}(T)$ has been evaluated from the STM images by measuring the total branch length and dividing by the number of atoms deposited on the corresponding area. It turns out that for small widths the STM tip images the arms about 6Å larger than their actual size. For the higher temperatures the imaged branch widths have been corrected by this offset. The flux I, i.e. the number of atoms arriving per second at the island perimeter of an aggregate can be estimated as follows: every island has an "active" area related to it, i.e. all atoms arriving onto this area, will, on average, perform their random walk towards the island. This "active" area is given by the inverse saturation island density, i.e $n_x \approx \Lambda_D^{-2}$ (same argument as used in 4.1). The impinging flux I onto the islands is therefore I $= R/n_x$ [Pim 93, Bar 941] (the accommodation probability is assumed to be unity, which is likely at the low temperatures of the experiment).

Since most islands nucleate for T > 130K at preexisting Pt-steps no n_x data are available for the higher temperatures (see 4.2.2). The flux I has therefore been evaluated by the introduction of an "active" area of a substrate step. This "active" area of a substrate step was defined as the product $\Lambda_{cri} \Lambda_{emp}$. Λ_{cri} is the largest substrate terrace width where no homogeneous nucleation occurs. Λ_{emp}, then, served as a fit parameter and was set to 300Å in order to archive correspondence with an extrapolation of the values obtained in the island growth case. Since a substrate step collects about twice as much atoms per unit time than an island (angle 2π) it follows I ≈ 2 R $(\Lambda_{cri} \times 300 \text{Å})^{-1}$. These I-values match at T = 130K within 10% with the one obtained by I $= R/n_x$.

Fig. 4.17 shows the Arrhenius plot of the measured $(\overline{w}\sqrt[n]{I})$ values (100K $\leq$ T $\leq$ 300K; n=2, 3) and compares the data with the above theoretical predictions. The expected Arrhenius behavior $(\overline{w}\sqrt[n]{I}) \propto \sqrt[n]{h_e} \approx \sqrt[n]{v_e/2} \exp(-E_e/nkT)$ is obviously for both models. The two data sets lie on straight lines. From the slope of the fitting lines a surprisingly low diffusion barrier E_e is calculated:
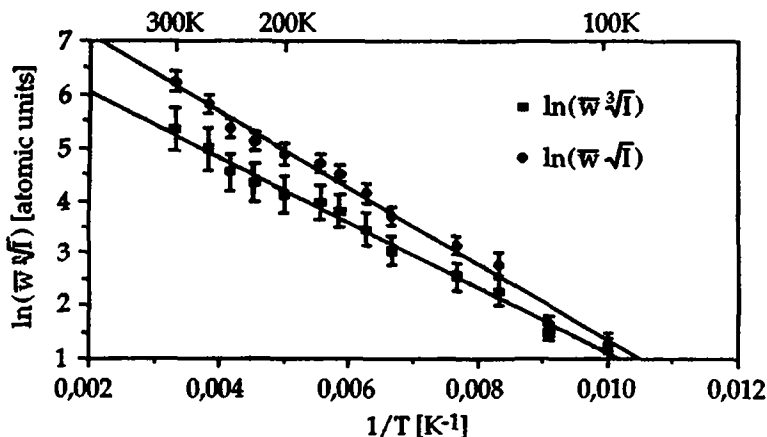
Fig. 4.17: Arrhenius behavior of the average branch width $\overline{w}$ evaluated according to the fractal growth theories of Pimpinelli et al. [Pim 93] and Bartelt et al. [Bar 941]. Details in text.

n = 2   (Bartelt and Evans): E_e = 125±10 meV

n = 3   (Pimpinelli et al.): E_e = 160±20 meV

Thus, the obtained step edge diffusion barriers are comparable with the lateral diffusion barrier E_D = 157 meV. If only the high temperature data (above T = 200K) are evaluated (in this region the mean width of the branches is $\overline{w} \geq 13\pm2.5$ which fulfills surely the assumptions of the models) one gets E_e = 145±20 meV for n = 2 and E_e = 200±30 meV for n = 3. Consequently, the intuitive requirement $E_D \ll E_e$ of fractal island growth (see beginning of 4.3) is strongly violated.

The natural explanation for the failure of this criterion is given by the evaluation of the attempt frequencies ν_e from the Arrhenius plots and the recognition that the condition $E_D \ll E_e$ is only valid for $\nu_D \approx \nu_e$, i.e. if the attempt frequencies of terrace and edge diffusion are comparable. Using the empirical formula $L_{cri} L_w \approx 1.7\sqrt{h_e/I}$ (from the simulations of Bartelt et Evans [Bar 941]) it can be concluded that the proportionality constant is of

the order one (in atomic units). From the intersection of the two data sets with the ordinate axis a step edge preexponential 2×10^5 Hz $< v_e < 2 \times 10^{10}$ Hz is inferred. Thus, the correct criterion for fractal growth reads $D_D \gg D_e$, i.e. a large difference between the lateral and step edge diffusion coefficients, which is fulfilled in the present case due to the inequation $v_D \approx 10^{13\pm1}$ Hz $\gg$ $v_e \approx 10^{8\pm2}$ Hz. Thus, the fractal growth in the heteroepitaxial system Ag/Pt(111) is to first order triggered by a slow step edge diffusion mechanism associated with a low preexponential factor of the order $D_0^{edge} \approx$ $4 \times 10^{-8\pm2}$ cm^2/s. As mentioned in 2.3.1, this suggests a deviation from the random walk model of diffusion. The low attempt frequency v_e indicates an exchange diffusion mechanism.

The attempt for an explanation of this effect refers to the statements given in 4.3.1. The anisotropy between A- and B-steps that showed to be different for hetero- and homoepitaxial systems was attributed to relaxation effects at the step edges. The similar behavior of Au/Ru(0001) concerning the branch widths at T = 300K suggests that indeed the 4.3% strain of the Ag islands is relieved at steps. Also Au grows pseudomorphically on Ru(0001), i.e. is by 6.3% compressed with respect to its bulk structure. So it is likely to assume that also in this strained system fractal growth is caused by a low preexponential factor D_0^{edge}.

In the homoepitaxial case of Pt/Pt(111), on the other hand, the difference between the lateral and the step edge diffusion coefficients is probably smaller than for Ag/Pt(111). At T = 200K the island edges are atomically rough but the island density is about a factor 30 higher than for Ag/Pt(111) at T = 130K, thus smaller fractal islands develop (see Fig. 1 (a) in ref. [Mic 93]). Step edge diffusion barriers $E_e^{A/B}$ and the terrace diffusion barrier E_D for Pt/Pt(111) have been measured by Field Ion Microscopy. The lateral barrier $E_D \approx 0.25$ eV [Fei 942] has been found to be a factor of 3 smaller than the edge

barriers $E_e^{A/B} \approx 0.7\text{-}0.8$ eV [Bas 78]. The preexponential factors for both diffusion mechanisms have about the same order of magnitude $D_0 \approx 10^{-3\pm1}$ cm^2/s, [Bas 78, Fei 942] (al least for the B-steps). Thus, the temperature dependence of the ratio D_e/D_D is governed by the Boltzmann-factor $\approx \exp(-2E_D/kT)$, i.e. decreases strongly with increasing temperature. In the heteroepitaxial case of Ag/Pt(111) (and probably Au/Ru(0001)), however, $E_D \approx E_e$ and therefore the ratio $D_e/D_D \approx \nu_e/\nu_D \approx 10^{-5\pm2}$ is to first order independent of deposition temperature due to the constant ratio of the attempt frequencies. This behavior favors also at higher temperatures limited step edge diffusion while already high lateral mobility is present to grow large islands.

4.4 Thermodynamics of Ag monolayers

Annealing of low temperature grown fractal islands to $T > 200K$ leads to conversion into much more compact forms. On the long time scale of such an annealing experiment step edge diffusion sets massively in and finally Ag atoms evaporate from the island edges, i.e. a two-dimensional adatom gas establishes. By further increase of temperature morphological changes of the Ag film become **reversible** in temperature, i.e. thermodynamic principles determine the adlayer structure.

The lateral Ag-Ag interaction is predominantly attractive. Due to the relatively small electronegativity difference between Ag and Pt (Pauling electronegativity Ag: 1.9, Pt: 2.2 [Pau 60]) the dipole-dipole repulsion is dominated by the attractive direct electronic interaction between the adsorbate atoms. As a consequence, at elevated temperatures phase separation into a dilute 2D-vapor and a dense 2D-condensate occurs (see e.g. [Bau 87]). The appearance of the vapor-condensate coexistence region has already been displayed in Fig. 4.1 d). At $\Theta = 0.1$ ML and $T = 400K$ a 2D-gas

phase composed of small Ag-clusters and (very probably) Ag-adatoms is imaged. On the other hand, a 2D-solid Ag phase attached to the substrate steps is formed. The 2D-vapor pressure of the condensate assures the equilibrium between both phases. Atoms from the perimeter of the condensed islands evaporate continuously onto the substrate terraces and readsorb from them.

4.4.1 Fragmentation of compact Ag islands

The STM topographies in Fig. 4.18 show on a large lateral scale the further thermal evolution of cluster aggregated Ag islands, i.e. the continuation of the annealing experiment discussed in 4.2.4 (see Fig. 4.9). The transition towards the thermodynamic equilibrium state of the morphology proceeds via three stages:

1) Ostwald ripening of the Ag island between $T = 230K$ and $T = 280K$ characterized by a broadened island size distribution and an increased average size $\bar{n}$ in b) with respect to a).

2) Roughening of the island edges visible by comparison of the insets in Fig. 4.18 b) and c). This is accompanied by a decreased average island size $\bar{n}$ in c) which is deducible from the smaller imaging size of the surviving larger islands (quantitative evaluation of $\bar{n}$ is hindered by the large amount of Ag attached at the substrate steps). Furthermore, small clusters are in coexistence with the remaining large islands.

3) Finally, the fragmentation of the Ag islands. The STM image in d) shows that even on terraces as wide as $\Lambda_S = 2000\text{Å}$ eventually all large islands are disintegrated and mainly the 2D-vapor phase is present on the terraces.

105

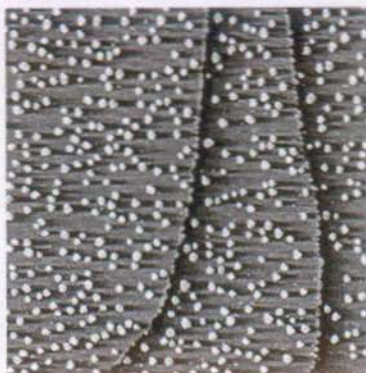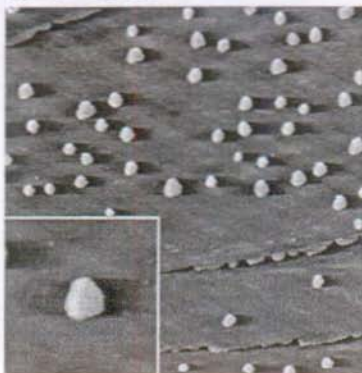a) T = 230 K   b) T = 280 K

c) T = 350 K   d) T = 400 K

800 Å

Fig. 4.18: a)-d) Ostwald-ripening, roughening and fragmentation of cluster aggregated Ag islands with increasing temperature. The total coverage is in a)-d) $\Theta = 0.1$ ML and the average island size is $\bar{n} = 230\pm30$ in a) and $\bar{n} = 680\pm70$ in b). Image sizes: 2300Åx2300Å, Insets in b) and c): 450Åx450Å, used flux $R = 1.1x10^{-3}$ ML/s.

Ostwald coarsening [Ost 00] is a well known process in the case of crystal growth from the melt (see e.g. [Mye 93]). In the thermodynamic limit the vapor pressure $P(r)$ of a crystallite is described by the Gibbs-Thomson

equation, i.e. P(r) increases as the size r decreases (see e.g. [Ker 82, Voo 92, Zin 92]). At elevated temperatures diffusional mass transfer from regions of high curvature to regions of low curvature takes place which reduces the total interfacial area of the crystalline phase. Smaller crystallites have a higher 2D-vapor pressure than larger ones, hence the exchange of atoms leads to growth of the larger sizes while the neighboring smaller crystallites decompose to maintain the concentration gradient toward the larger ones. Consequently, the average size $\bar{n}$ increases and the size distribution becomes broader.

Both effects are observed in the annealing experiment of low temperature deposited Ag. While at low temperatures ($T < 150K$, $\bar{n} < \approx 30$) a solely thermodynamic description is not appropriate (see 4.2.4), at higher temperature the evaporation of atoms establishes an adatom gas between the islands and the ripening of the island population proceeds by a two-dimensional Ostwald coarsening process. Also for $T > 200K$ a more detailed understanding of the microscopic processes enabling the growth of size-selected clusters demands further investigations, as already mentioned in 4.2.4.

The larger islands in Fig. 4.18 b) are close to their 2D-equilibrium form as indicated by their hexagonal shape (see inset). From the observed length ratio between A- and B-steps $1^A/1^B = 0.5\pm0.10$ and by applying the Wulff-construction (shown in Fig. 2.9 c)) to a 2D-hexagon, i.e. by using the relation:

$$\frac{\gamma_B}{\gamma_A} \;=\; \frac{\left|\bar{r}_B\right|}{\left|\bar{r}_A\right|} \;=\; \frac{1/2 + 1^A/1^B}{1^A/1^B + 1}$$

the ratio $\gamma_B/\gamma_A = 0.8\pm0.05$ between the step free energies of A- and B-steps is obtained. Thus, the B steps which form closed-packed $\{111\}$ facets with

107

the layers below have the lower step energy, as expected. The same is observed for Pt vacancy and adatom islands on Pt(111) ($\gamma_B/\gamma_A = 0.87\pm0.02$ [Mic 912, Mic 93]). Consequently, the step energetics of Ag/Pt(111) is comparable with the homoepitaxial case, i.e the ratio γ_B/γ_A is not inverted due to the strain in the (1x1) Ag islands, in contrast to the observed relation between the two step edge diffusion barriers $E_e^{A/B}$ and the low attempt frequencies v_e.

It is important to note that compact islands cannot be obtained by a direct growth experiment at a certain temperature due to the fractal growth kinetics of Ag/Pt(111) (see 4.3.4). The step edge diffusion which is necessary to equilibrate the island shape sets in at temperatures where Ag grows in the "step flow" mode, i.e. where no more homogeneous nucleation occurs. Hence, only by annealing of low temperature deposited Ag the thermodynamic properties of Ag islands are observable.

At T = 350K the decay of the equilibrium form starts and is completed at T = 400K as shown in Fig. 4.18 c) and d). In c) the step edges of the larger Ag islands are imaged very rough (see inset), demonstrating that the fragmentation is driven via kink excitation (edge roughening) and subsequent evaporation of less coordinated edge atoms onto terraces. Closer inspection of the STM images reveals that at T = 350K the condensate phase (Ag attached to the substrate steps) exhibits no "frizzy" appearance. This is in contrast to d) (at the 50K higher temperature) where on the same lateral scale the condensate steps are imaged as rough as the edges of the islands in c).

108

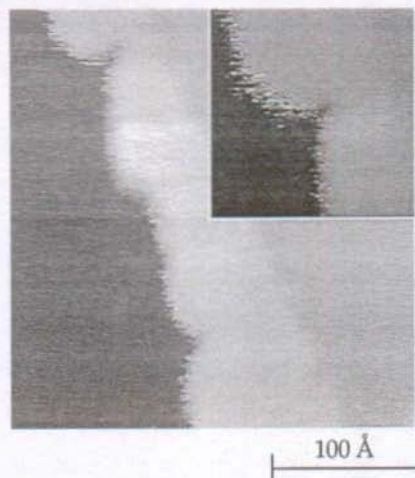T = 400 K, Θ = 0.3 ML

100 Å

Fig. 4.19: Rough imaged step edges of the condensate phase. The "frizzes" are caused by kink motion being rapid on the STM time scale. The inset shows a subsequent recorded (time interval ≈ 3 min) enlargement of the upper left corner. The "frizzy" appearance of the step has no correlation with the previously recorded image. Image sizes: 280Åx280Å, Inset: 92Åx92Å, used flux R = 1.1×10^{-3} ML/s.

A detailed STM image of the "frizzes" is shown in Fig. 4.19 for the condensate at T = 400K. The imaged ruggedness of monatomic steps is attributed to kink motion at the steps being much faster than the scanning of the tip which finds, therefore, the step in each scanning line at a different position (see e.g. [Wol 90, Poe 92, Gir 94]). The time dependence of the position fluctuations is also directly observable by using faster or modified STM scanning techniques (see e.g.[Kui 93, Gie 93]). In these cases the step dynamics can be determined quantitatively by STM, e.g. by measuring the temperature dependence of the "frizzes" to deduce the activation energies for the emission of atoms from kink sites [Gie 93].

The different onset temperatures of the edge roughening of isolated Ag islands with respect to Ag condensed at the steps can be attributed to a stabilization effect of the substrate steps. Indeed, half of the condensate boundary is "locked in" the substrate structure while for an isolated island the whole perimeter consists of strained steps (without lateral "support"). This interpretation is in good qualitative agreement with static and molecular dynamics computations using embedded atom potentials by Blandin et al. [Bla 941, Bla 942]. The static computation of the contour energy of monatomic Ag on Pt(111) leads to a factor 2.5 lower value than the calculation for Ag adsorbed on an artificially strained Pt substrate with Ag lattice constant. This indicates that the 4.3% misfit strain plays a crucial role for the edge roughening and therefore for the fragmentation of the islands.

The behavior of the computed slab (930 adsorption sites) in the molecular dynamics simulations of Blandin et al. changes drastically by removing the strain without altering the Ag-Ag interaction potential in a significant way. The population of the artificial relaxed Ag layer (230 adsorbed atoms) collapses after a few nsec into a unique aggregate. At the same simulation temperature strained Ag, on the other hand, consists of a dilute vapor in local equilibrium with a population of larger clusters (n ≈ 30-40). Thus, the essential experimental feature -the appearance of a 2D-vapor phase- is well reproduced even on this short time scale. Also the predicted step-adsorbate interaction (attractive for the ascending and slightly repulsive for the descending substrate steps) is in good agreement with the STM experiment [Bla 942].

4.4.2 2D-gas in equilibrium with a 2D-solid

In the following the real space observation of a two-dimensional thermodynamic equilibrium state and the 2D-gas-condensate phase
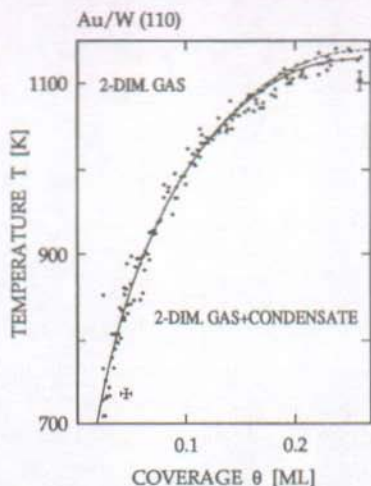
Fig. 4.20: Coexistence curve between single-phase (2D-gas) and two-phase region (2D-gas + condensate) in the (Θ,T)-plane of Au/W(110). The data points are derived from the reversible work function change $\Delta\phi(\Theta,T)$ of the gold film. The curve is the van der Waals coexistence curve for $T_c = 1130K$ and $\Theta_c = 0.26$ ML. Details in text (from [Kol 84]).

transition of the Ag monolayer is compared with the experimental results of Kolaczkiewicz and Bauer [Kol 84, Kol 851, Kol 87]. They observed 2D-gas-condensate phase transitions for (similar strained) metallic submonolayers (Ag, Au, Cu, etc.) on the W(110) and Mo(001) surface.

Fig. 4.20 shows the (Θ,T) phase diagram derived from the **reversible** work function change $\Delta\phi$ of Au submonolayers on W(110) with temperature. The evaluation of the $\Delta\phi$ data is based on the dependence of the dipole moment of an atom on its neighborhood. An isolated atom has a large dipole moment p while the same atoms incorporated into a 2D-crystal have a much smaller value. This change allows, therefore, to determine the number density and fractional coverage of the two phases.

111

The coexistence curve between gas and condensate in Fig. 4.20 is calculated from the two-dimensional van der Waals equation which, just as in the 3D case, serves as an interpolation formula to describe the behavior of 2D-gases in the region of high density n (see e.g. [Das 75]). Two experimental observations on Ag/Pt(111) can be compared with the 2D-gas-condensate coexistence curve derived for Au/W(110) and similar heteroepitaxial systems:

1. At low coverages solely the 2D-gas phase should be formed before the condensation of large Ag islands should take place.

2. At constant coverage the density of the 2D-gas phase should increase with increasing temperature.

For the first point the influence of the substrate step has to be taken into account. The STM images in Fig. 4.21 show the morphology at $T = 500K$ which seems to be dominated by the gas phase at the low coverage of $\Theta = 0.05$ ML but the substrate steps are wetted with a narrow Ag seam (≈ 30-35Å wide). Evaluation of coverage ratio between condensate and gas (from the known total coverage) shows that about 65% of the Ag is condensed at the steps. Hence, the comparison with the ideal thermodynamic behavior is hindered by this stabilized condensate. The second point, however, is confirmed by the real space observations on Ag/Pt(111) as shown in the two STM images in Fig. 4.22. The 2D-gas phase increases with increasing temperature at constant coverage Θ.

Kolaczkiewicz and Bauer applied, furthermore, the two-dimensional Clausius-Clapeyron equation to deduce the 2D-heat of evaporation versus temperature [Kol 852, Kol 851, Kol 87]. From their analysis they concluded that a two-dimensional roughening transition of Ag island edges on W(110) should take place at $T = 500K$ [Kol 851]. Although this result is compatible
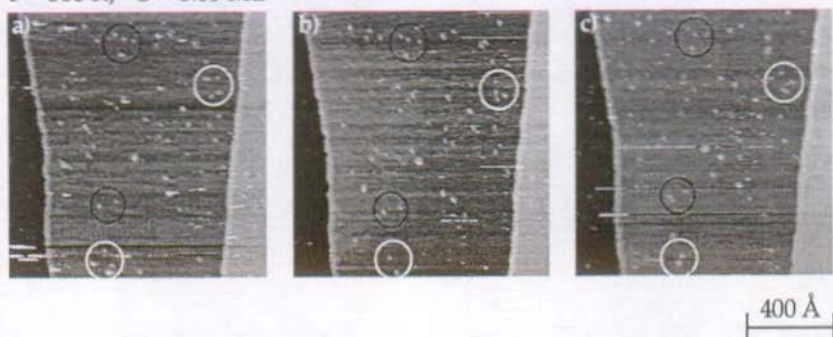
$T = 500 \text{ K}, \quad \Theta = 0.05 \text{ ML}$

400 Å

Fig. 4.21: a)-c) Mobility of gas-phase clusters on the STM time scale at T = 500K. The time distance between each image is about 3 min. The black encircled cluster groups remain basically constant, while clusters in the white encircled areas change their positions with respect to each other. Image size: 1180Åx1180Å, used flux R = 1.1×10^{-3} ML/s.

with the observations on Ag/Pt(111) the main approximation to extract the relevant data is the assumption of a perfect monatomic gas, i.e. the 2D-spreading pressure has been taken to $\pi = nRT$ where n is the atomic density of the gas phase.

This approximation is surely not fulfilled for Ag/Pt(111) because the 2D-gas is imaged by STM and adatoms are invisible. From the derived diffusion constants it can be calculated that at T = 400K an Ag atom makes about 10^{10} hops per sec which is orders of magnitudes faster than the tip scanning motion. Thus the observed 2D-gas contains small clusters. Their mobility on the STM time scale is displayed in Fig. 4.21. In the molecular dynamics simulations of Blandin et al. stability peaks in the cluster size distributions (at the "magic" sizes n = 7, 10, etc.) appear for low simulation temperatures while at higher T the clusters are observed to be "fluidlike" without preference for a certain size [Bla 942]. It is likely to assume that the imaged small clusters in the T range from 350K to 500K are "magic" and have

a) T = 400 K   b) T = 500 K

500 Å

Fig. 4.22: a), b) Decrease of the condensate-phase with increasing temperature for Θ = 0.6 ML. Image size: 2450Åx2450Å, used flux R = $1.1x10^{-3}$ ML/s.

threefold coordinated perimeter atoms, but unfortunately no experimental evidence exists for this.

In summary, the microscopic picture given from the STM study is that the 2D-gas phase is highly non-ideal (which may be labeled as "real" gas) with a strong tendency to form small clusters. Secondly, the substrate steps stabilize the 2D-solid phase. Both results require sophisticated theoretical models to extract quantitative thermodynamic parameters from the data.

5. Monolayer confined Ag/Pt alloy

Deposition at, as well as annealing to T > 620K leads to interfacial alloy formation. Since the second layer grows layerwise on top of the completed first Ag layer (up to the desorption temperature) alloy formation is only observed for submonolayer coverages (Θ < 1 ML). Thus, the intermixing of the two metals is confined to the topmost surface layer. In 5.1 the two-dimensional intermixing process and the global morphology of the Ag/Pt alloy surface are discussed. The microscopic structure of the mixed phase is outlined in 5.2.

5.1 Two-dimensional intermixing

Exchange processes between chemical different atoms are frequently observed in heteroepitaxial systems. For example: diffusion mechanisms on metallic fcc (110) surfaces often involve that a adsorbate atom takes the position of a surface atom, i.e. the adsorbate becomes part of the substrate (e.g. in the system Cu/Pd(110) [Hah 94]).

Alloy formation in metal-on-metal heteroepitaxy is a well known phenomenon, e.g. for Au and Cu [Pal 682, Pal 681]. Since these two metals form a well-ordered bulk alloy, this result is not surprising. On the other hand, also metals which are not miscible in the bulk, intermix at surfaces (e.g. Au/Ni(110) [Nie 93], Rh/Au(111) [Alt 94]). Here, the miscibility of a certain material combination can be substantially differ from the bulk behavior. Surface segregation, i.e. the enrichment of one component in the topmost layers of a bulk alloy (see e.g. [Buc 82]) has its origin in this difference between surface and bulk miscibility. 3D-crystals of Ag and Pt are known to be miscible at elevated temperatures (T > 700K) forming a substitutional bulk alloy [Kar 87].

5.1.1 Incomplete mixtures

Fig. 5.1 a) and b) show the Ag film morphology at $\Theta = 0.5$ ML after annealing to, as well as, after direct growth at $T = 630K$. Both structures have been quenched to $T = 400K$ for the recording of the STM images. Hence, they display the frozen-in structure of the alloy. In the annealing case, the intermixing process is visualized by the line scan in c). The global alloy morphology in the direct growth case is shown in d). The origin of the chemical Ag/Pt contrast in the STM images has already been discussed in 3.3.2.

The Pt-terraces in the STM topography in a) appear spotted with small protrusions of an approximate diameter of 10Å. In contrast, the Ag islands are distorted by indentations of comparable width. Their apparent height in the STM images is about that of the former Pt steps. On the other hand, the height of the protrusions inside the Pt terraces ($\Delta h = 0.6$-0.7Å relative to surrounding Pt) is equivalent to the height of the adsorbed Ag islands, visible in the line scan in c). Hence, it is straightforward to identify the inclusions inside the Pt terraces with small two-dimensional Ag clusters which have diffused into the Pt terraces, whereas the indentations in the Ag islands must be associated with Pt clusters which mixed into the Ag islands.

The obvious roughening of the one-dimensional interface between Ag islands and Pt-steps and the increase of the density of the clusters towards the former step edges indicate that the interdiffusion of Ag into the first Pt layer proceeds from the lower step edge side, and that of Pt into the Ag islands on the lower terrace through the wetted Ag-Pt interface. Also in the vicinity of separated Ag islands (in the middle of the Pt terraces) an increased cluster density is remarkable.
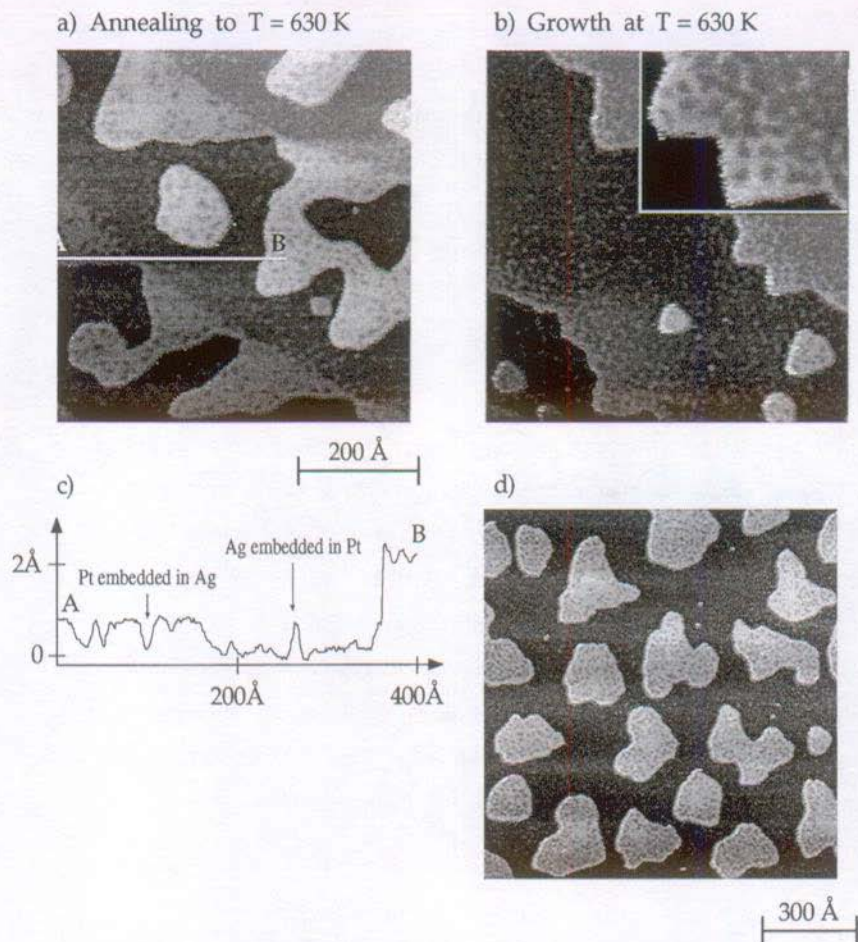
116

a) Annealing to T = 630 K   b) Growth at T = 630 K

200 Å

c)

2Å
Pt embedded in Ag
A
Ag embedded in Pt
B
0
200Å   400Å

d)

300 Å

Fig. 5.1: a), b) Formation of the monolayer confined Ag/Pt alloy. In a) the coverage $\Theta = 0.5$ ML has been annealed to T = 630K for 100s, while in b) the same amount of Ag has been directly deposited at T = 630K. Both STM images show the frozen-in structure of the film at T = 400K. In b) the contrast on each terrace has been separately adjusted.

c) Line scan along the bar AB marked in the absolute STM image in a) showing the interdiffusion of Ag clusters in the Pt-terrace and Pt clusters in the Ag-layer.

d) Morphology on a larger Pt-terrace in the direct growth experiment. Image sizes: a), b) 600Åx600Å, d) 1150Åx1150Å, inset in b): 160Åx120Å, used flux $R = 1.1 \times 10^{-3}$ ML/s.

117

In the annealing case, the steps present at the surface (predominantly the Ag-wetted Pt-steps) are, therefore, the active sites for the mixing process. In the direct growth experiment, on the other hand, the crucial role of the substrate steps is further supported. In b) on terrace widths $\Lambda_S \approx 300$Å, the uniformly impinging Ag atoms have mixed into Pt solely at substrate step edges, which is obvious from the decreasing local Ag coverage with increasing distance from the step. In the inset an enlargement is shown where the local Ag coverage has reduced by 40%, when going from 60Å to 120Å away from the former Pt-step.

The morphology on a large substrate terrace, as the one shown in d) ($\Lambda_S >$ 1200Å), reveals that in absence of steps Ag-enriched islands are formed. This is a further indication that mixing processes are restricted to step edges and alloying does not occur on terraces. A molecular dynamics simulation supports the observation that alloy formation dynamics can be triggered by the step edges. Raeker and DePristo observed in their simulations of Ni/Cu(111) that Ni atoms are incorporated on the upper substrate terrace near the step edge through displacement of the edge outwards [Rae 92]. Mixing on the terrace was not observed by the authors.

The conclusion that the Ag/Pt intermixing is confined to the topmost layer has been derived from the following two observations:

1) The apparent Ag concentration in the topmost layer, derived from the height distribution on the terraces, agrees within errors with the deposited amount of Ag.

2) The coverage region close to the complete Ag monolayer was carefully examined revealing that mixing occurs only for $\Theta < 1$ ML. At the crystal locations where the local coverage was slightly
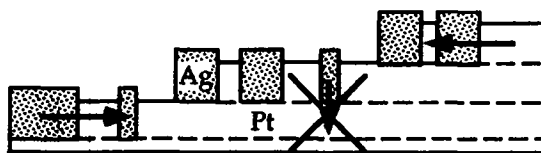
Fig. 5.2: Illustration of the lateral Ag/Pt mixing process leading to the monolayer confined alloy surface. Ag diffusion into deeper layers is kinetically hindered by an activation energy which cannot be overcome before thermal desorption sets in.

higher than 1 ML, the first layer was completed with second layer island on top.

Fig. 5.2 illustrates the essential requirement for a restriction of the Ag/Pt mixing process to two dimensions: Diffusion into deeper layers must be kinetically hindered by an activation energy for interlayer mass transport which cannot be overcome before thermal desorption sets in. The latter starts at $T \approx 900K$ (see Fig. 2.10). This holds true for all Ag coverages $\Theta < 1$ ML and all temperatures up to the desorption threshold. Since in heteroepitaxial growth the Ag adsorbate is never covered by Pt atoms, it is likely to assume that also bulk alloying of Ag and Pt proceeds not via {111} facets.

The formation of the monolayer confined Ag/Pt alloy has first been detected by He scattering. During the alloy formation Becker et al. [Bec 93] observed a decrease of the He-reflectivity which they attributed to adsorbed Ag fragmented in small clusters, although this decay of the specular He signal is caused by the enhanced diffuse scattering of embedded Ag and Pt clusters. The fragmentation hypothesis of Becker et al. was supported by LEED measurements suggesting that the height of the diffuse scattering clusters is 2.3Å. Since for the quantitative evaluation of the LEED data kinematic

119

a) T = 630 K, 10 min

b) T = 640 K, 1 min

c) T = 700 K, 1 min

d) T = 630 K, 100 min

300 Å

Fig. 5.3:   a)-d): Influence of annealing time and temperature on the two-dimensional Ag/Pt intermixing process at $\Theta = 0.5$ ML. The alloy surface in a) has been further annealed in b) and c) up to the indicated temperatures. The morphology in d), on the other hand, was only annealed for 100 min at T = 630K. The images show the frozen-in structure at T = 400K. Image size: 1150Å×1150Å, used flux R = 10^{-3} ML/s.

diffraction theory has been applied it seems that the latter is not adequate for the analysis of the Ag/Pt alloy surface.

The subatomic STM imaging height of the alloy structures has been additionally confirmed by recent He diffraction measurements [Krz 94]. The intensity of the corresponding He diffraction peak changes as a function of the He-energy ("rocking curves") in such a way that the "step height" of the clusters is smaller than 0.2Å.

5.1.2 Alloy formation kinetics

The same inhomogeneous cluster distribution, as shown in Fig 5.1, can be obtained by annealing to slightly lower temperatures with subsequently longer annealing times. This gives support to the interpretation of a quenched, incomplete mixing of Ag and Pt which is observed after cooling to T = 400K. The influence of annealing temperature and time on the intermixing process is displayed in Fig. 5.3. The four STM images show alloy morphologies at Θ = 0.5 ML on substrate terrace widths Λ_S = 400-700Å. In the series from a) to c), the annealing time and temperature have been subsequently increased.

The start morphology in a) is six times longer annealed at T = 630K than the mixture in Fig. 5.1 a). Ag-rich and Pt-rich areas are still visible. Also in b) this remains valid, but here the "global" chemical contrast between Ag-rich and Pt-rich regions is only recognizable near the former substrate steps. This changes drastically in c), the surface is now a complete mixture of Ag and Pt since the terraces are homogeneous spotted with the 10Å wide protrusions corresponding to embedded Ag. All step edges of the complete mixed alloy surface are wetted with a about 10Å wide Ag seam.

The influence of the annealing time is displayed in d). Annealing the same Ag coverage for 100 min at T = 630K leads to the same homogeneous mixture than the one additional minute at T = 700K in the transition from

T = 700 K,   Θ = 0.5 ML

500 Å

Fig. 5.4: Two-dimensional "frozen drops" of the quenched alloy surface after annealing of Θ = 0.5 ML for 100s at T = 700K. Image size: 2200Åx2200Å, used flux R = 1.1x10^{-3} ML/s.

b) to c). Thus, the outcome of the alloy formation kinetics is a function of annealing time **and** temperature, as expected for temperature dependent rate processes controlling the mixing of the two metals. Annealing to T > 650K for more than 100s leads to the completion of the mixing process.

Surprisingly, the dissolution of Ag into the Pt(111) surface is not complete, i.e continues not to an atomic mixture. Further increasing of the annealing temperature (and time) leads only to modifications of the global alloy morphology. The microscopic surface composition and the size of the Ag clusters, however, remain unchanged up to the onset of thermal desorption. The Ag dissolution comes to a standstill at a finite cluster size imaged by STM with a width of about 10Å. The origin of the microscopic alloy structure and its dependence on the Ag coverage is discussed in 5.2.
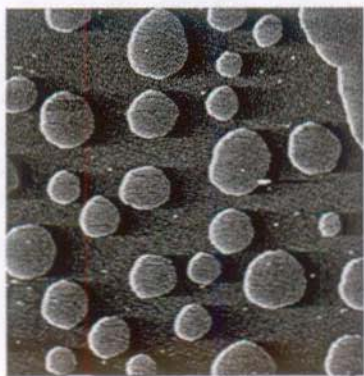
122

a) T = 550 K　　　　　　　　　　b) T = 600 K

c) T = 850 K　　　　　　　　　　a) T = 900 K

500 Å

Fig. 5.5:　a)-d) Morphological transitions in the beginning of the alloy formation in a), b) and at the end of the high temperature treatment in c), d). The coverage of the "frozen-in" structures is always Θ = 0.5 ML The film in a) (100s at T =550K) has been annealed a further 100s at T = 600K, shown in b). The transition between c) (100s at T =850K) and d) is caused by a subsequent anneal for 100s at T = 900K. Image size: 2300ÅX2300Å, used flux R = 1.1×10^{-3} ML/s.

Alloy morphologies of the coverage Θ = 0.5 ML are displayed in the figures 5.4 and 5.5. The STM topography in Fig. 5.4 shows the completely mixed

123

a) T = 600 K

b) T = 700 K

500 Å
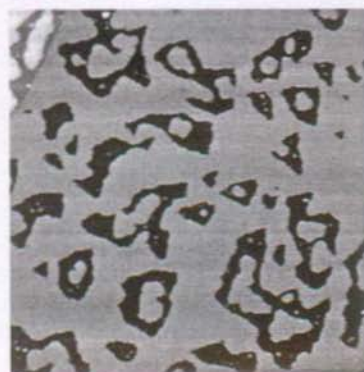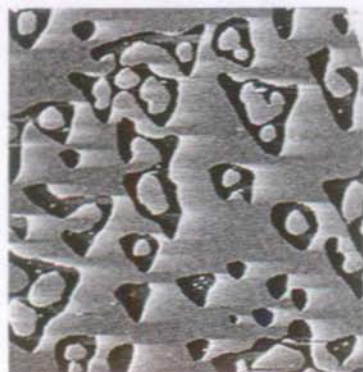
Fig. 5.6: a) b) Morphological features of the quenched Ag-rich alloy surface with a coverage Θ = 0.75 ML. Round alloy islands are isolated in holes of the mixture network. a) 100s anneal at T = 550 and 600K, b) subsequent anneal for 100s at T = 650K and 700K. Image size: 2300Åx2300Å, used flux R = 10^{-3} ML/s.

alloy surface after annealing for 100s at T = 700K. "Drop-like" structures attached to the former substrate steps are formed. Fig. 5.5 shows in a) and b) on a large lateral scale the fragmentation of the annealed Ag, when the two-dimensional intermixing sets in. Between c) and d) the same morphological transition takes place on substrate terrace widths of $\Lambda_S \approx$ 1500-2000Å, as displayed in Fig. 5.3 c) and d) on smaller terraces.

The increasing of the product "annealing time x temperature" leads to a "cut off" process of the two-dimensional "liquid-like" drops attached to the substrate steps. At the end, one remains only with round shaped alloy islands on the terraces. This is shown in Fig. 5.5 d) for a large terrace and in Fig. 5.3 d) for smaller terraces and an accordingly lower product "annealing time x temperature". In Fig. 5.6 a similar morphological effect is displayed for the Ag-rich alloy surface (Θ = 0.75 ML). In this case, the mixing process

124

leads to isolated alloy islands located in the holes of an alloy network attached to the substrate steps.

The border length of isolated alloy islands seems to be minimized, whereas islands connected to a substrate step appear to maximize their perimeter length. The kinetic effects producing these "drop"-structures have their origin in the constitution of the second layer of the crystal, which is pure Pt, and its consequence on the lateral mobility of the alloy layer. If, for instance, an alloy island changes its size or shape, Ag has to be transferred to the topmost layer at the alloy step edges in order to "create" new second layer area. Thus, exchange processes cannot be restricted to two dimensions.

Morphological changes are determined by the lateral mass transport at the former substrate steps, as well as by vertical exchange processes taking place at the Ag-wetted alloy step edges. The shape and size of isolated alloy islands are solely governed by this (isotropic) interlayer mass transport. "Drop"-structures, on the other hand, have in addition intralayer mass transport via the former substrate steps. At intermediate annealing temperatures, this additional (and anisotropic) material exchange causes a roughening of the one-dimensional border of those alloy structures which are connected to substrate steps. This kinetic effect vanishes for high annealing temperatures (or long annealing times). Then, the equilibrium surface morphology exhibits even on large terraces no alloy islands and the Ag-wetted alloy step edges minimize their border length.

5.2 Microscopic alloy structure

### 5.2.1 Disk and stripe patterns

Fig. 5.7 displays the coverage dependence of the microscopic alloy structure. For $\Theta < 0.25$ ML small dissolved Ag-islands ("disks") are homogeneously

a) $\Theta = 0.08$ ML

b) $\Theta = 0.22$ ML

c) $\Theta = 0.30$ ML
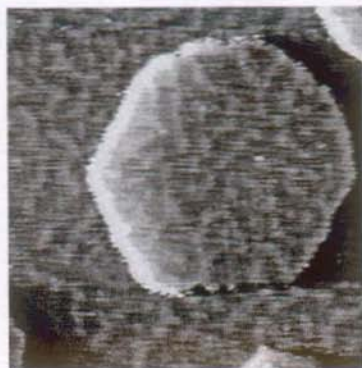
d) $\Theta = 0.55$ ML

100 Å

Fig. 5.7: a)-d) Disk to stripe transition of embedded Ag clusters with increasing coverage. The average size of the disks is $\bar{n} = 9.0 \pm 2$ in a) and $\bar{n} = 9.5 \pm 1$ in b). Image size: 225Åx225Å, Annealing temperatures: a) T = 700K, c) T = 800K, b), d) T = 850K; used flux R = 1.1×10^{-3} ML/s.

distributed over the terraces. The clusters reveal a narrow distribution of the imaging size, centered at approximately 10-13Å. The average cluster size $\bar{n}$ has been determined by the cluster density and the calibrated coverage, and turns out to $\bar{n} = 9.5 \pm 1.0$ atoms which is in accordance with the imaging size.

126
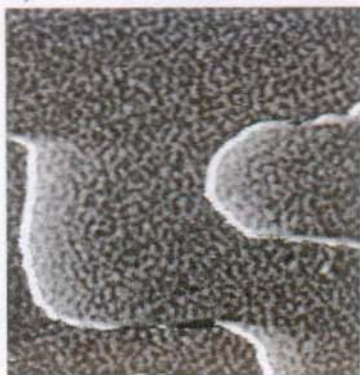
a) T = 850 K   b) T = 900 K
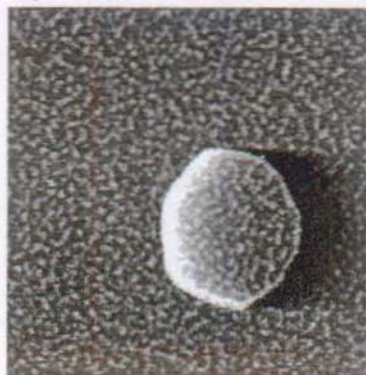
c) T = 1000 K   d) T = 1050 K
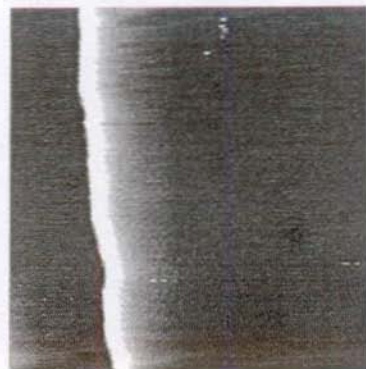
200 Å

Fig. 5.8:   a)-d) Stripe to disk transition by thermal desorption. The coverage $\Theta = 0.5$ ML is from a) to d) subsequently desorbed by annealing for 100s to the indicated temperatures. In d) no more Ag can be detected in the Pt-terraces, while the defect in the right side of the image is clearly resolved. Image size: 615Åx615Å; used flux R = 1.1×10^{-3} ML/s.

At coverages $\Theta \geq 0.3$ ML, displayed in Fig. 5.7 c) and d), the clusters touch each other which leads to a striped pattern. The width of this fingerlike agglomerations of clusters is again about 10-13Å which supports the

127

a) Θ = 0.70 ML b) Θ = 0.80 ML
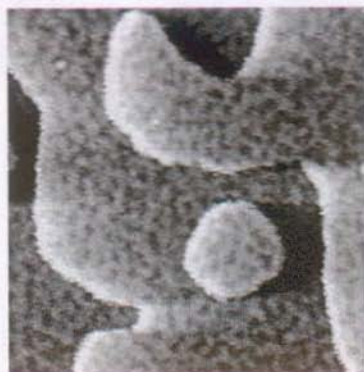
c) Θ = 0.90 ML d) Θ = 0.95 ML

|——| 100 Å

Fig. 5.9: a)-d) Stripe to disk transition of embedded Pt with increasing Ag coverage. The coverages in these images is estimated. Details in text. The average size of the disks is $\bar{n} = 10$ in d) Image size: 420Åx420Å, Annealing temperatures: a)-c) T =750K, d) T = 650K; used flux R = 1.1×10^{-3} ML/s.

interpretation of random agglomerations of single clusters. Fig. 5.8 shows the "reverse" transition from stripes to disks by thermal desorption of the coverage Θ = 0.5 ML.

The inverted situation is displayed in Fig. 5.9 at Ag coverages $\Theta \geq 0.7$ ML. The coverage of these STM images is estimated since they were recorded at the border of the Pt-crystal where a coverage gradient was present. Small Pt clusters are dissolved in the topmost Ag layer. The apparent width of these embedded Pt clusters equals to that of the embedded Ag clusters in the Pt surface. From their imaging width, the cluster density and the estimated coverage it can be concluded $\bar{n} \approx 10$ atoms. Thus, again agglomerations of 7 to 12 Pt-atoms are involved in the formation of the monolayer confined Ag/Pt alloy surface for $\Theta > 0.75$ ML. This symmetry of the alloy structure for low and high Ag coverages is consistent with the symmetric enthalpy of mixing found for the liquid silver-platinum solution [Kar 87].

5.2.2 Thermodynamics of the mixed Ag/Pt phase

In a model binary mixture, including interaction between the particles, the thermodynamic equilibrium cluster size is determined by the minimum of the free energy of the system, i.e. the competition of the boundary energy, which in this case is the energy of the one-dimensional Ag/Pt-interface, and the mixing entropy, which is proportional to the number of clusters. The variation of the boundary energy is supposed to be linear with the length of the boundary, or the width of the clusters, whereas the mixing entropy or the number of clusters is indirect proportional to the squared cluster size. When this simple concept of a potential energy, only depending on the length of the boundary, would be applicable in the Ag/Pt case, strong variations of the cluster size on the entropy term of the free energy, or the temperature, respectively, would have to be expected.

A series of annealing experiments for $\Theta = 0.2$ ML (up to the desorption threshold) showed any dependence of the cluster size on the annealing temperature. Hence, the simple concept of the internal energy of the

129

clusters, depending simply on the boundary length does not apply here. There must exist an important contribution to this internal energy, strongly varying with the cluster size and providing a local minimum at a cluster size of about 7 to 12 atoms. This term overrides the variation of the entropy with temperature. This is further supported by the observation that the Ag-($\Theta < 0.25$ ML) and the Pt- ($\Theta > 0.75$ ML) cluster sizes are independent of the coverage.

The occurrence of "magic" numbers in the stability of small adsorbed two-dimensional clusters on hexagonal close-packed surfaces has been already mentioned in 2.3.6. In particular the clusters of n = 7, 10 and 12 atoms, the smallest structures with at least threefold coordinations at the entire cluster perimeter, are found to be substantially stabilized. With respect to dimers, adsorbed $Ag_{7,10,12}$ -clusters are energetically favored by 0.20 - 0.22 eV/atom, as calculated with the embedded atom method [Mas 93] (see Fig. 2.7 b)). This high dissociation energy clearly overrides the entropy term, i.e. $\Delta E \gg kT$.

In contrast to adsorbed clusters, perimeter atoms of embedded Ag clusters exhibit three additional bonds. Nevertheless, the observed medium size $\bar{n} = 9.5 \pm 1.0$ atoms at low and high Ag coverages, as well as the STM imaging size are in good agreement with a distribution of embedded Ag_n- and Pt_n-clusters with n = 7, 10, 12. Thus, to first order, also the "frozen-in" structure (T < 500K) of the two-dimensional Ag/Pt alloy appears to be governed by the high internal energy of symmetric cluster structures. At higher temperatures (T > 600K), however, entropy effects leads to a reversible transformation into a truly disordered 2D alloy, as revealed by He scattering and high temperature STM [Zep 94].
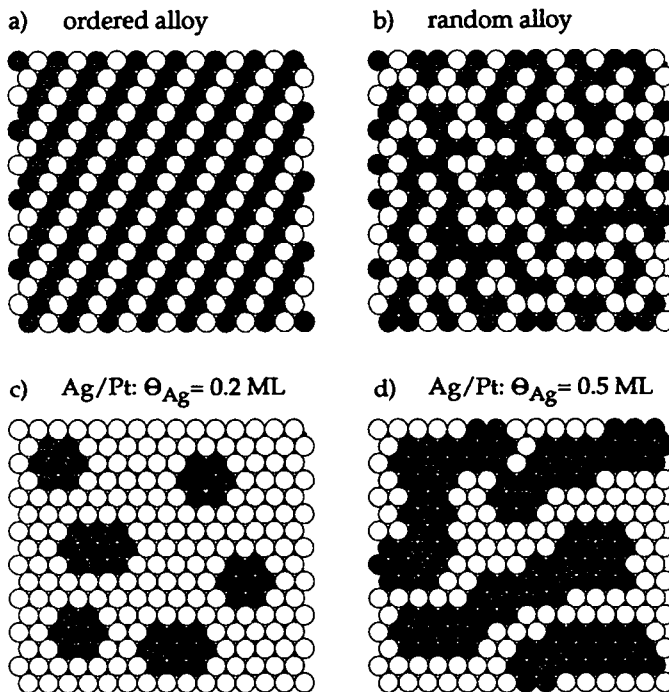
a)   ordered alloy   b)   random alloy

c)   Ag/Pt: Θ_{Ag}= 0.2 ML   d)   Ag/Pt: Θ_{Ag}= 0.5 ML

Fig. 5.10: a)-d) Illustration of different types of alloy structures described in the text.

The chemical order of the frozen-in alloy structure is determined by the mixing enthalpy ΔH_{mix} representing the difference in internal energy before and after mixing (at constant pressure) (see e.g. [Por 81]). For ΔH_{mix} = 0 (ideal solution), a random arrangement of atoms is the equilibrium state (random alloy). For $\Delta H_{mix} \neq 0$, the actual arrangement will be a compromise that gives the lowest internal energy consistent with sufficient entropy, or randomness, to achieve the minimum free energy G = H -TS of the alloy. In the quasi-chemical model it is assumed that ΔH_{mix} is only given by the bond energies between adjacent atoms. Mixed phases are known as regular

solutions, when their ΔH_{mix} dependence on temperature and composition is closely described by this approximation. In this case, it can be shown: $\Delta H_{mix} \propto z \varepsilon\, X_A\, X_B$, where z is the number of bonds per A-and B-atom of the A/B binary solid solution (concentrations X_A, X_B) [Por 81]. ε is the difference between the A-B bond energy ε_{AB} and the average of the A-A and B-B bond energies ε_{AA} and ε_{BB}, i.e. $\varepsilon = \varepsilon_{AB} - \frac{1}{2}(\varepsilon_{AA} + \varepsilon_{BB})$, by considering zero energy to be the state where the atoms are separated to infinity ($\varepsilon_{ij} < 0$).

The ideal solution ($\varepsilon = 0$) shows no chemical ordering, while for $\varepsilon < 0$ the atoms will prefer to be surrounded by atoms of the opposite type since the internal energy is reduced by increasing the number of A-B bonds (ordered alloy). The frozen-in Ag/Pt alloy surface, on the other hand, is an example for $\varepsilon < 0$ since clustering occurs, i.e. the internal energy can be reduced by increasing the number of Ag-Ag and Pt-Pt bonds. However, the degree of ordering will decrease as temperature increases due to the increasing importance of entropy, as observed for the monolayer confined alloy at T > 600K [Zep 942].

If the mixed atoms exhibit a size difference, an additional energetic contribution is the elastic strain field which introduce a strain energy term into ΔH_{mix}. Zeppenfeld et al. [Zep 941] showed that strained layers and, more generally, surface systems governed by effective long-range interactions decaying as $1/r^2$ exhibit periodically ordered domain structures. From the minimization of the free energy the authors could deduce a firm relation between the size l of a single domain (at low concentration Θ) and the minimum separation D_{min} between them at intermediate concentration Θ. This size ratio is about 1 : 3, i.e.

$$\frac{\text{size } l_0 = l(\Theta \to 0)}{\text{periodicity } D_{min} = D(\Theta = 0.5)} \approx \frac{1}{3}$$

The above relation is independent of the symmetry (striped or various two-dimensional arrangements) of the domain pattern and is observed for a variety of different systems.

He diffraction measurements show that the frozen-in Ag/Pt mixture at Ag coverages 0.1 ML $\leq \Theta \leq$ 0.75 ML exhibits superstructure features corresponding to a characteristic lateral distance in real space of D $\approx$ 30Å [Zep 942]. This is in good agreement with the mean separation D (which varies slowly with the coverage Θ) of the embedded Ag and Pt clusters (size l $\approx$ 10Å), as resolved by STM. The experimental confirmation of the above size relation reveals the strong influence of the strain relief on the energetics of the monolayer confined alloy. Furthermore, the observation of the disk to stripe transition with increasing coverage (illustrated in Fig. 5.10 c) and d)) is an additional confirmation that the strain field stabilizes the Ag/Pt alloy structure, since both symmetries are compatible with the model of Zeppenfeld et al..

The spectroscopic confirmation of the monolayer confined mixing has been given by Strüber et al. [Star 93]. Their main results are shown in Fig. 5.7 and are in very good agreement with the STM results. Similar mixing effects as observed for Ag/Pt(111) seem to occur for Ag growth on the other two low-index Pt surfaces (100) and (110) [Star 94]. Unfortunately, Rodriguez et al. did not anneal Ag submonolayer coverages on Pt(111) high enough (T < 600K) to observe a change of their infrared spectra due to the monolayer confined mixing [Rod 92]. In their FT-IRAS-study of adsorbed CO on the Ag covered Pt(111) surface the authors focused on the "screening" effect of CO adsorbed on Ag layers. Even at coverages Θ_{Ag} < 0.7 ML CO molecules adsorbed on Pt(111) are "invisible" for the infrared spectroscopy.
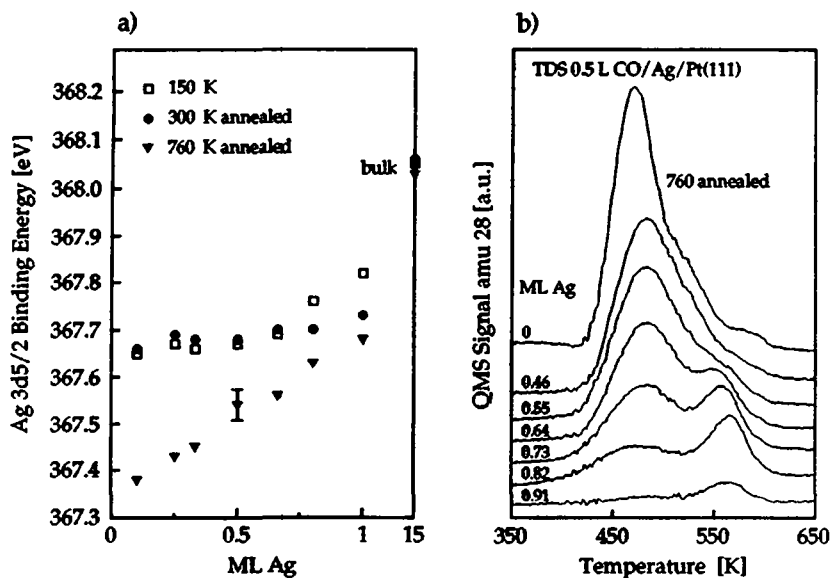
133

Fig. 5.11: a), b) Spectroscopic confirmation of the monolayer confined Ag/Pt alloy by XPS and CO-TDS.

a) Position of the XPS peak maxima of the $3d_{5/2}$ Ag core level for $\Theta < 1$ ML after deposition at T = 150K and subsequent annealing to T = 300K and 760K, respectively. A peak shift for embedded with respect to adsorbed Ag is visible.

b) Desorption spectra of CO from the Ag/Pt alloy surface (0.5 Langmuir CO exposure) as a function of Ag coverage. For $\Theta > 0.5$ ML a second desorption peak develops referring to a Pt-cluster adsorption site of the CO. a), b) from [Strü 93].

6. Multilayer structure and mass transport between growing layers

In this chapter the restriction to two dimensions is lifted and the structure and growth kinetics of the higher Ag layers are analyzed. The presentation of the results is divided in two parts. In 6.1 the strain relief mechanism of the second and higher layers is discussed. Thus, this section focuses on structural aspects, i.e. the kinetics and energetics of misfit dislocations. The atomistic processes and the kinetic barriers involved in multilayer growth are analyzed in 6.2.

6.1 Strain relief by domain wall formation

From the structural point of view there is one main question: how can the pseudomorphically, i.e. by 8.3% (in density) compressed Ag monolayer, develop into a strain-free multilayer film with Ag bulk structure ?

In general, the lattice mismatch is locally relieved by the introduction of misfit dislocations, as mentioned in 2.2. Thus, in the intermediate thickness range the Ag layers consist of large areas which are nearly commensurate, separated by relatively narrow domain walls or discommensurations.

6.1.1 Weakly incommensurate phases at hexagonal close-packed interfaces

Apart from mismatched heteroepitaxial films, weakly incommensurate layers are also observed on reconstructed close-packed metal surfaces, which are up to present knowledge the (111)-oriented surfaces of Au [Per 74, Tan 81] and Pt [San 92, Bot 93]. These reconstructions are driven by the considerable tensile stress in the outermost layer (see e.g. [Man 90, Nee 91] and they consist in the introduction of a certain density of domain walls between alternating fcc and hcp stacking regions. For Au(111) the 4%

compression of the first layer is achieved by two domain-walls per $(\sqrt{3}\times22)$-unit cell, each inserting one half extra atom, thus leading to 23 atoms adsorbed on 22 second layer atoms along the close packed $[1\bar{1}0]$-direction [Har 85, Bar 90]. Due to the difference in energy more fcc- than hcp-sites are populated giving rise to a pairwise arrangement of the $[11\bar{2}]$-oriented domain-walls. Locally the compression is unidirectional, however on larger terraces a mesoscopic order of the domain walls is established: The domain walls bend by $\pm120°$ with a period of 250Å [Bar 90] forming the so called herringbone structure which reduces the anisotropy of the surface stress tensor [Bar 90, Nar 92].

6.1.2 Second layer strain relief: T < 700K

The structure of the second Ag monolayer grown at T = 340K is characterized by the STM image in Fig 6.1 a). The structural model in b) will be discussed below [Bru 942].

The lower left part and a few holes one monolayer deep in the upper part of the STM topography still show the first Ag monolayer which is imaged flat due to its (1x1) structure. In contrast the second monolayer terrace covering most of the image reveals two domains of a striped structure rotated by 120°. Localized stripes, imaged dark, are pairwise arranged and separate brighter imaged areas with two different widths. These stripes are running along the $[11\bar{2}]$-direction and are bended to U's in the vicinity of the descending Ag step preventing that the narrower ones of the bright areas touch the step. The orientation and the pairwise arrangement as well as the U-turns of these stripes are very similar to the domain walls on Au(111) [Bar 90]. Thus, an interpretation of these lines as diluted walls separating fcc- and hcp-stacking regions is straight-forward. Their dark imaging has already been discussed in 3.3.2.

a) Θ = 1.5 ML

100 Å

b)

Fig. 6.1: a) Growth at T = 340K: unidirectional relaxed phase of the second Ag layer. Image size: 520Åx520Å, used flux R = 1.1x10^{-3} ML/s. b) Atomic model for the striped incommensurate (SI) phase. Black dots: 1st layer atoms , bright and dark filled circles: 2nd layer atoms on fcc- and hcp-positions, respectively.

Those bright areas which face the descending steps are assumed to be fcc regions because it is reasonable to assume bulk stacking in the vicinity of the steps [Bar 90]. In accordance with this interpretation, these areas are by a factor of 2 larger than those corresponding to the less favorable hcp-stacking. The period of this striped phase varies around 37±3Å, and can thus be characterized by a ($\sqrt{3}$ xp) unit cell with p = (14±1).

In the known examples of linear incommensurate phases, as Au(111) and Cu/Ru(0001) [Pöt 91], the topmost layers are unidirectional compressed relative to the underlying ones, whereas the second Ag layer adsorbed on Pt(111) is unidirectional expanded. The model in b) for the $(\sqrt{3} \times p)$ unit cell therefore consists of (p-1) second layer atoms adsorbed on p atoms of the first Ag (1x1)-layer. At the domain walls the stacking transition from fcc to hcp and vice versa takes place by stretching the Ag-Ag bond along the close packed $[1\bar{1}0]$ direction corresponding to half an atom missing. Thus, for p = 14 this yields 8 atoms adsorbed on fcc sites and 5 atoms have to reside on hcp sites, corresponding to an average relaxation by 7.1% along $[1\bar{1}0]$.

The small width of the dark lines (5±1Å) indicates that the domain walls are rather narrow. Hence, the dilution of the second Ag layer must be rather localized to the immediate vicinity of the domain walls. To take account for this, it is assumed that only three Ag-Ag bonds around the domain wall are stretched along $[1\bar{1}0]$ and further on, that most of this stretching is localized to the bond directly at the domain wall. Therefore the two adjacent atoms to the left and right from the domain wall are shifted only slightly from their hollow position towards each other. Any more homogeneous stretching would result in broader domain walls than the observed one.

This rather localized dilution, i.e. one relatively stretched Ag-Ag bond in favor of a more homogeneous distributed strain relief, is energetically preferred for two reasons. First, the disadvantageous bridge sites are not populated in these domain walls. The second argument for a localized stretching of bonds is the unsymmetry of the atomic interaction potential around its minimum: For compressed layers one deals with the steep ascending repulsive part of the lateral interaction potential which makes the layer stiff and rectifies the population of unfavorable sites as bridge- and

138

a) T = 500 K, Θ = 1.5 ML   b) T = 600 K, Θ = 1.5 ML

[1$\bar{1}$0]

100 Å

Fig. 6.2: a), b) Annealing to T = 500K and 600K: Transition of unidirectional to isotropic strain relief of the second layer by crossing of the misfit dislocation lines. Image sizes: 540Åx540Å, used flux R = 1.1x10^{-3} ML/s

almost on top-sites in U's and stars on Au and Pt(111), respectively [Bar 90, Bot 93]. However, for diluted layers as in the present case, the soft attractive branch of the potential allows for rather localized stretching of bonds which causes more abrupt changes between the two stacking types.

Fig. 6.2 displays the Ag bilayer after annealing to T = 500 and 600K, respectively. These STM images, as well as the in the following presented topographies of relaxation structures, has been recorded at T ≤ 400K. Due to the slow misfit dislocation kinetics this quenching has no influence on the interpretation of kinetic effects.

In a) the coexistence of the striped incommensurable (SI) phase with a network of crossing domain walls is visible. The different atomic structure of these walls is already indicated by the fact that they are running along the close packed [1$\bar{1}$0] direction, thus rotated by 30° against the SI-phase. In b), after annealing to T = 600K, the second layer island exhibits a more regular

139

domain wall network with a hexagonal arrangement of the crossing regions.

In general, the energy of a dislocation network consists of three contributions: wall, wall-repulsion-, and wall-crossing energy. By annealing of the SI-phase to $T = 500K$ the kinetic barrier to nucleate areas where domain walls can cross can be overcome. Since the distances between the walls remain approximately constant mainly the energy cost for wall crossing is overbalanced by the more isotropic strain relief. For $T < 700K$, all the created patterns are rather irregular and depend on the terrace width Λ_S and the island shape, respectively. Both networks shown in the STM images of Fig. 6.2, as well as the SI-phase, are kinetically determined structures, i.e. intermediate "solutions" of the second layer to relieve the strain.

6.1.3 Equilibrium structure of the second layer

Annealed to $T > 700K$, the Ag bilayer forms its equilibrium structure consisting of a trigonal network of domain walls, as shown in Fig. 6.3 a). An atomic model for the trigonal structure is sketched in b) [Bru 942].

The STM image shows two subsequent atomic terraces, both covered with two Ag monolayers. A small area on the right hand side still shows the commensurate first layer and the position of the former substrate step (see also the description of Fig. 3.9 in 3.3.2). On the second layer two almost parallel sets of domain walls rotated by 120° are clearly visible. They are crossing each other enclosing rhombi of slightly elevated imaged areas separated by the dark imaged domain walls. In addition each rhombus has a small triangle inscribed on top. Two borders of these triangles consist of the two sets of domain walls, the third borders running almost horizontally are formed by a third set of parallel domain walls.
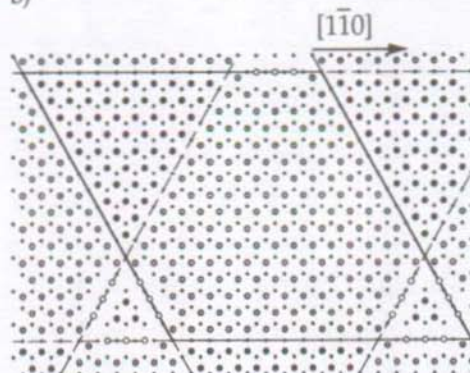
140

a) $\Theta = 1.5\,\text{ML}$

100 Å
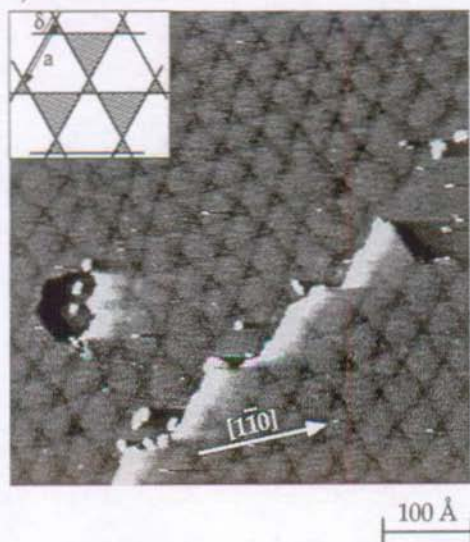
b)

Fig. 6.3: a) Annealing to T = 800K: trigonal network constituting the equilibrium structure of the second Ag layer. Inset: Model for the trigonal network, where domain walls (dark lines) separate fcc- and hcp- (hatched) areas. Image size: 520Åx520Å, used flux R = 1.1×10^{-3} ML/s.

b) Atomic model of the trigonal incommensurate phase. Black dots: 1st layer atoms, bright and dark filled circles: 2nd layer atoms on fcc- and hcp-positions, respectively, unfilled circles: 2nd layer atoms on bridge positions.

141

These domain walls are clearly visible in the vicinity of these triangles, but they are harder to identify in the areas between adjacent triangles where they are crossing the rhombi. The lower contrast for the third set of domain walls is due to recording of the $\partial z/\partial x$-signal, which is less sensitive to features that are oriented to the horizontal x direction.

A model for this trigonal incommensurate (TI) phase is shown in the inset of a). The three classes of parallel domain walls don't cross in one point, i. e. one set has an offset δ with respect to the crossing point of the other two sets. This generates the small triangles characterizing the structure and allows for a higher amount of fcc- than hcp- stacking. The measured value for the offset δ is 0.3 times the period of the network. As evident from the STM image this network is also not very regular and reveals many defects. The average period as deduced from STM is 44.8±1.4Å. It thus can approximately be described by a (16x16) unit cell, as sketched in Fig. 6.3 b).

Inside one unit cell there are a smaller and a bigger triangle, both of which are hcp-stacked, and an fcc-stacked hexagon with 3 longer and three shorter borders. The borders are formed by the $[1\overline{1}0]$-oriented domain walls. Resulting from symmetry there are two different types for these domain walls. The longer borders of the hexagon which incline also the larger triangles are simply stacking transitions from ideal fcc- to hcp- positions. The Ag atoms at the domain wall have only five bonds, the one which crosses the domain wall is stretched by 15%. In the shorter borders, inclining the small triangles, the atoms populate bridge sites. Evidently, the latter type of domain walls reveals a higher dilution (bonds are stretched by 26%). Hence, it should appear lower than the first type, due to the total "charge density imaging". This is indeed found in Fig. 6.3 a). The higher geometry of the bridge site is assumed to be overbalanced by the charge density effect.

142

a) Θ = 1.5 ML

500 Å
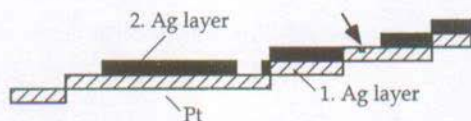
b)

2. Ag layer

Pt

1. Ag layer
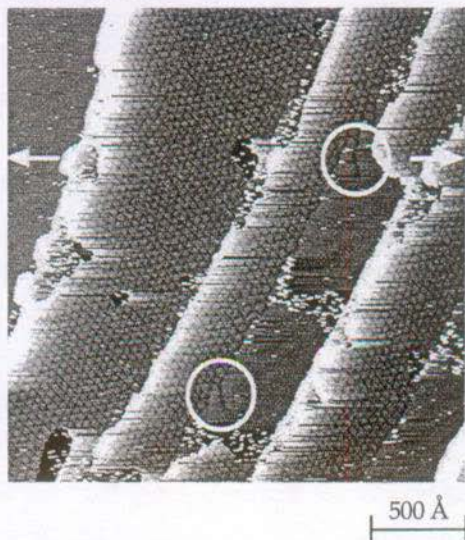
Fig. 6.4: a) Large scale topography of the trigonal network. The flat imaged (1x1) first layer terrace is disturbed by dark imaged linear stripes (white encircled). These local dilutions are induced by the domain wall network touching the first layer at the ascending substrate step. Image size: 2450Åx2450Å, used flux R = 1.1x10⁻³ ML/s.

b) Schematic profile showing the stacking of atomic layers in a horizontal cut along the white arrows in a).

In agreement with the STM data, the threefold symmetry of the annealed second layer has also been seen in helium diffraction measurements [Poe 93, Rom 94]. It results from the unequal size of the two hcp stacked triangles and from the stacking transitions inside the unit cell. According to the atomic model in b) the density of the second layer is reduced by 7.0%, i.e. 238 second layer atoms are adsorbed on 256 atoms of the first layer. The ratio of

143

fcc- to hcp- sites is 2.8, which lies in between the value of 2.0 for Au(111) [Bar 90] and of 3.8 for Pt(111) [San 92].

Fig. 6.4 shows a large scale STM image of several atomic terraces partly covered by the second layer. The second layer domain wall network is in coexistence with terraces covered by the flat imaged first layer. In the middle of the image there is a Ag (1x1) terrace that exhibits two worm-shaped depletions. They extend more than 100Å into the first layer terrace. Comparison with the orientation of the domain walls shows that they run along the $[11\bar{2}]$-direction. These linear depletions are never found for submonolayer coverages and are always restricted to the area where the first and the second layer terrace touch each other. They can be considered as a localized restructuring of the first layer which has been induced by the presence of the second layer. Due to the equal imaging height of these linear depletions and domain walls from the network, they have to be areas of locally reduced Ag atom density. However, their structure can not be the one of simple domain walls, because they do not separate fcc and hcp stacking areas. Presumably, the structure inside these stripes is similar to two adjacent domain walls from the SI phase described above.

6.1.4 Structure of the third and higher layers

The kinetics of the third layer strain relief is displayed in Fig. 6.5. Crossing of domain walls is already observed for T ≈ 250K, as shown in a). At T ≈ 310K, where the second layer exhibits the kinetic SI-phase, the third layer is already in its hexagonal equilibrium structure (visible by the two small third layer regions in b)). Thus, the symmetry of the equilibrium pattern changes between the second and third layer from trigonal to hexagonal which is in accordance with observations from He diffraction [Poe 93, Rom 94].

a) T = 250 K, Θ = 3 ML   b) T = 310 K, Θ = 2.5 ML
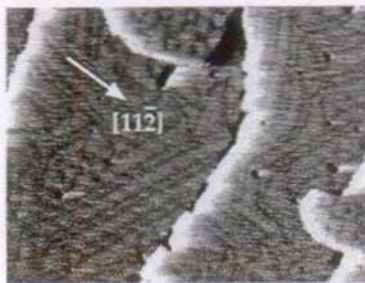
⊢ 200 Å ⊣

Fig. 6.5:   a) b) Misfit dislocation kinetics of the third Ag layer. The striped pattern in a) transforms to a hexagonal pattern already by a slight temperature increase of 60K, as shown in b). The main part of the STM image in b) is covered with the SI-phase of the second layer. Two small areas in the upper part and at the right hand side show the hexagonal equilibrium structure of the third layer. Image size: 615Åx465Å, used flux R = 1.1x10^{-3} ML/s.

If annealed to T ≥ 500K, the third layer structure does not undergo any more structural changes. The STM images in Fig. 6.6 reveal a periodic structure consisting of hexagonally arranged protruding areas surrounded by darker lines which separate them from a homogeneously protruding area. The orientation of the unit cell characterizing this structure is parallel to the SI-phase and therefore rotated by 30° against the equilibrium structure of the second layer. The periodicity of the third layer has been determined by STM to 23.5±3Å as nearest neighbor distance of the hexagonal areas. The pattern remains irregular even after annealing just below the desorption threshold, as shown in b).

The equilibrium structure of the fourth and higher layers is displayed in Fig. 6.7. A modulation of the film surface is resolvable by STM up to 15 ML. The imaging features are similar to the third layer structure and even the period of the protruding areas hardly changes (n=4: 24.5±3Å, n=5: 23.4±3Å, n=10:

145

a) T = 500 K, Θ = 2.7 ML   b) T = 800 K, Θ = 3 ML

$[11\bar{2}]$

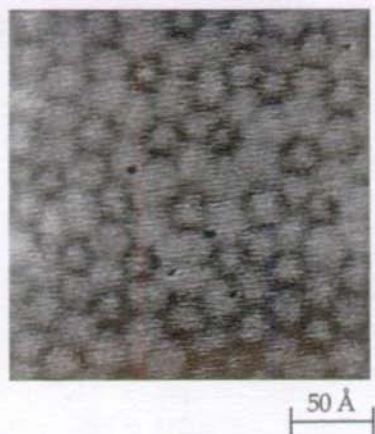|100 Å| |50 Å|

Fig. 6.6: a) b) Hexagonal domain wall pattern of the third layer. The close-packed direction runs along the $[11\bar{2}]$ direction, i.e. parallel to the second layer SI-phase second visible in the upper part of the STM image. The hexagonally arranged protruding areas remains irregular even after annealing to T = 800K. Image sizes: a) 520Å×520Å, b) 220Å×220Å, used flux 1.1×10^{-3} ML/s.

25.5±3Å). However, the STM topographies in Fig. 6.6 and 6.7 show that the third and higher layers still are incommensurate and have a non isotropic stress tensor. The strain relief of the Ag film has finished after 25 ML as revealed by He diffraction measurements [Rom 94] which is in good agreement with the STM results.

6.1.5 Ag layer stacking on Pt(111)

The metastable SI-phase formed by the non annealed second Ag layer is similar to the Au(111) reconstruction and the striped phase for the Cu/Ru(0001) system [Pöt 91]. The Pt(111) reconstruction is also an example for a pairwise arrangement of domain walls [Bot 93]. Thus, this symmetry is found for many weakly incommensurate phases on hexagonal close-packed metal surfaces.

146

a) 4 ML   b) 5 ML

c) 10 ML   d) 15 ML

50 Å

100 Å

Fig. 6.7:   a)- d) Equilibrium structure of the higher Ag layers after annealing to T = 800K. Image sizes: a), b) 250Åx250Å; c), d) 365Åx365Å, used flux R = 1.1x10^{-3} ML/s.

In contrast to the Ag bilayer on Pt(111), in all these examples the topmost layers reveal a higher density compared to the underlying bulk. This involves domain walls with a locally increased density. For the second Ag layer, the atomic density is locally reduced at the domain walls. This has the

structural consequence that they are narrower (imaged 5±1Å) and offer a lower quantity of unfavorable adsorption sites. The small width of the domain walls is confirmed by the He diffraction data (2-5Å [Rom 94]).

The fact that the SI-phase is metastable is due to its restriction to locally unidirectional strain relief. In the case of Au, Pt and Cu/Ru(0001) this handicap is overcome by alteration of the domain walls. For these systems this seems to be the only way to a more isotropic strain relief. The SI-phase is stable for Cu/Ru(0001) upon annealing to 1000K, Au(111) reveals this phase up to 880K [San 912], and the Pt(111) structure imaged by STM at low temperatures [Bot 93] is considered to be very similar to the reconstruction appearing for T > 1300K [San 92]. Thus, the domain wall interaction energy in these three examples seems to be too high to allow the crossing of domain walls. This could be caused by the on-top adsorption sites which would have to be occupied in these crossing points. For the Ag bilayer on Pt(111) domain walls are diluted zones which apparently have a lower interaction energy. Especially, they do not involve unfavorable sites at their crossing points. This makes it reasonable that a trigonal domain wall network can establish upon annealing which allows for an isotropic strain relief on a more local scale.

Networks which are similar to the TI-phase have been observed in surfactant mediated growth of Ge on Si(111) [Hor 93] and for Na adsorption on Au(111) [Bar 942]. These systems try to increase their fraction of ideal stacking with respect to the faulted one. For Na/Au(111) the domain walls are crossing in one point and incline alternating smaller (hcp) and bigger (fcc) triangles. In the Ag/Pt(111) case, the introduction of a phase shift δ (see Fig. 6.3) allows for every fraction of fcc- to hcp-stacking between 1 (offset δ = 0) and 3 (δ = 0.5a). The further advantage of this phase shift is that crossing

148

of all three domain walls is avoided. The value $\delta = 0.3$ deduced from the STM data is compatible with the one that fits the He diffraction spectra [Rom 94].

Although the symmetry of the dislocation networks for the second and higher Ag layers derived from STM agree well with the results of surface integrating methods, there exist two disagreements. First, the periodicitys are too low in comparison with the He diffraction and SPA-LEED (Spot profile analyzing LEED) data ($\approx$ (25x25) for the second and $\approx$ (22x22) for the third layer [Poe 93, Rom 94] against $\approx$ (16x16) and $\approx$ (8x8) derived from the STM imaging). This difference is beyond a calibration error of the STM tube scanner regarding all the other data derived from the deflection characteristic of the piezoceramic tube which are compatible with surface integrating methods. One explanation may be the irregularity of the domain wall networks. Their symmetry and therefore the essential physics is not touched by this non resolved difference.

The second point concerns the relation between fcc and hcp areas of the kinetic SI-phase. In the photoelectron forward scattering study of Rangelov et al. [Ran 94] a majority of hcp-sites has been determined for the room temperature grown Ag bilayer. The argumentation in 6.1.2 used a thermodynamic argument to distinguish both types of occupation sites, i.e. energetically preferred bulk stacking near the descending step edges of the second Ag layer islands has been assumed to relate the wider stripes of the SI-phase to fcc-sites. Since this domain wall network is determined by the relaxation kinetics this disagreement is not major. After annealing the majority of second layer atoms are on fcc-sites [Ran 94], as energetically expected and used in the modeling of the TI-phase.

149

The relaxation of the Ag film depends on the annealing history. Rangelov et al. [Ran 94] revealed that multilayer films grown at T = 300K conserve the stacking fault (hcp) between the first and second layer even after annealing. On the other hand, a fcc-oriented Ag film is produced by stopping the deposition after Θ = 2 ML, annealing the second monolayer, i.e. converting the SI- to the TI-phase, and continue the growth of the higher multilayers. The epitaxial orientation of the film depends, therefore, on the fact if the second layer is covered during the anneal or not. This effect is a consequence of the vertical film relaxation which is also neglected in the atomic models of the SI- and TI-phase, i.e. it has been assumed that the pseudomorphic first layer doesn't relieve its strain by adsorption of the second layer. In the present case, this approximation is likely and is furthermore justified by the fact that the atomic models of the SI- and TI-phase reflect many experimental observations. On the other hand, a detailed modeling of the third and higher layer structures without the consideration of the relaxation of the layers below is unrealistic.

6.2 Multilayer growth kinetics

The thermodynamic FM-growth mode of Ag/Pt(111) (see 2.1.2) is obtained for deposition temperatures above T = 500K. At lower temperatures, the interlayer mass transport is hindered by kinetic barriers, i.e. atoms deposited on higher layers cannot diffuse to the not yet completed lower layers. Consequently, high coverage films grown at T < 500K exhibit morphologies where several layers are simultaneously exposed.

The analysis of the multilayer growth kinetics has to separate two main factors determining the effectiveness of the interlayer mass transport:

- The form of the adsorption potential near a descending step.

- The transport of atoms to the step edge sites.

A film atom has to overcome the "Schwoebel"-barrier V_e to descend one layer level (see 2.3.4). Assuming that these jump down processes are thermally activated the interlayer diffusion may be in addition hindered by a blocked transport to the step edge sites. Before atoms can reach a step to jump down they may be captured by nucleation and successive growth of "on top islands". Whether this happens depends on the morphology of the uncompleted layer (density, size and shape of adlayer islands), the deposition rate and the on top diffusivity. In heteroepitaxial systems all these factors vary furthermore with the layer number n which complicates substantially the analysis in comparison with homoepitaxial systems.

6.2.1 Step down diffusion from monatomic thick islands

A nonequilibrium film morphology will be smooth if atoms can leave the tops of islands fast enough that their density ρ (on top of an island) remains always below a critical nucleation threshold. If this stays valid until the completion of the growing layer, i.e. even for large islands after the beginning of coalescence, the multilayer growth proceeds layer-by-layer wise.

Zhang et al. [Zha 94] introduced a determinant factor F discriminating the different contributions to the adatom density ρ on top of a monatomic high island of lateral size L (see Fig. 6.8). The adlayer island is characterized by its ratio N_{per}/N_{tot}, where N_{per} is the number of perimeter sites and N_{tot} is the total number of adsorption sites on the island. Since a deposited atom is randomly situated the ratio N_{per}/N_{tot} can be interpreted as the fraction of hop attempts to jump down from the island perimeter. The latter is
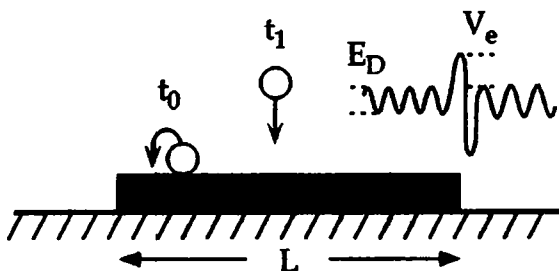
Fig. 6.8 Illustration of the main contributions to the adatom density ρ on top of a monatomic adlayer island of size L:

ρ increases with the rate $(t_1)^{-1}$, where t_1 is the average time between two landing events on the island. The probability that an adatom can reach a perimeter site and jumps down to the lower level is determined by the on top diffusion rate $(t_0)^{-1} = v_0 \exp\{-E_D/kT\}$ and the "Schwoebel"- barrier V_e at the descending step edges.

successful with a probability $\propto \exp\{-V_e/kT\}$. The lower limit for the number of hops before a meeting event with another atom can occur is given by the time ratio t_1/t_0, where t_1 is the average time interval between two landing events on the island and t_0 is the residence time spent at each adsorption site, i.e. $(t_0)^{-1} = v_0 \exp\{-E_D/kT\}$, where v_0 and E_D are the attempt frequency and the barrier for diffusion on top of the island. In summary, the factor F is composed of the three terms described above:

$$F \propto t_1/t_0 \times N_{per}/N_{tot} \times \exp\left\{-V_e/kT\right\}$$

F is to a good approximation proportional to the probability that an adatom can hop to the lower layer before being joined by a second deposited atom landing on the same island. If the critical cluster size on top of the island is the adatom (i = 1), then F measures directly the probability of a nucleation event. Also for i ≥ 2 the factor F remains to first order applicable since the building of larger nucleus sizes requires the formation of critical (i = 2) or

152

sub critical (i > 2) dimers. Since large F implies a low adatom density ρ one expects to observe improved layer-by-layer growth behavior whenever the value of F is quantitatively enlarged.

At constant deposition flux R and temperature T the interlayer mass transport depends on the island properties, i.e. its size and shape determine t_1 and N_{per}/N_{tot}, while V_e is given by its step edge structure. Assuming a compact shaped island ($N_{per}/N_{tot} \ll 1$) of size L, then $t_1 \propto 1/RL^2$ and $N_{per}/N_{tot} \propto 1/L$, thus F decreases with $1/L^3$ as the island grows laterally. Finally, at the critical size L_{cr}, the adatom density ρ becomes high enough that nucleation on top sets in. If $L_{cr}(R,T)$ is smaller than the average island spacing of the layer, then the next layer nucleates before the growing layer has completed and 3D-growth occurs [Ter 941]. Rosenfeld et al. [Ros 93] have experimentally verified this island size effect for Ag deposition on Ag(111). An enhanced interlayer mass transport has been monitored as the size of the compact shaped Ag islands was artificially decreased.

Fractal islands exhibit a ratio N_{per}/N_{tot} of the order one which implies a larger F with respect to compact shaped islands. Two additional factors which are not contained in the above derivation of the determinant factor F favor the interlayer mass transport in this case. First, FIM studies suggest a reduction of the potential barrier V_e with decreasing lateral size up to a break down around 20Å [Fin 84]. Second, step edges of ramified islands exhibit an increased number of kink sites. Here, the barrier V_e is predicted to be considerable lower with respect to straight step edges running along close-packed directions [Jac 94, Vil 942].

The most prominent example in which fractal shape effects play an important role for the multilayer growth kinetics is the reentrant 2D-growth behavior of Pt/Pt(111) [Kun 90]. In this system, 2D-growth occurs at high

temperature, while for $T \leq 620K$ the Pt film grows three-dimensionally rough. Surprisingly, an enhanced interlayer mass transport is observed at even lower temperatures ($T \leq 275K$). Since in this temperature range the aggregated Pt islands are small and have a branched shape [Bot 92], the above discussed additional effects on the factor F seem to cause this unexpected interlayer diffusion [Jac 94, Poe 91, Bot 92, Wan 94, Vil 941, Vil 942].

In the following the main factors hindering the interlayer mass transport of Ag/Pt(111) are qualitatively deduced for three different temperature ranges. In the last section a consistent picture of the multilayer growth kinetics as a function of coverage and temperature is proposed.

6.2.2 Mass transport from the second to the first layer: $T < 150K$

Two STM images in Fig. 6.9 show the atomically rough morphology of a Ag film grown at $T = 40K$. At this temperature lateral as well as vertical diffusion is completely frozen in. This result is in accordance with He-diffraction measurements [Krz 94].

The growth scenario at $T = 80K$ is displayed in Fig. 6.10 as a function of coverage. After deposition of $\Theta = 0.05$ ML the average island size is $\bar{n} = 16\pm2$ as shown in a). Subsequent Ag-deposition leads exclusively to the growth of the existing islands. Atoms landing on top are incorporated up to about 0.5 ML at the perimeter of the two-dimensional islands, thus interlayer mass transport occurs. The coalescence of the islands does not promote the second layer nucleation which can be seen in b). At $\Theta = 0.6$ ML only a few second layer islands are visible while the first layer is connected in a coalescence network.
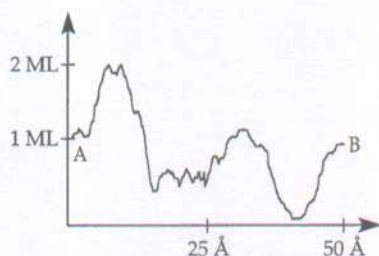
154

i

a) Θ = 0.45 ML

b) Θ = 1.3 ML

|20 Å|

|50 Å|
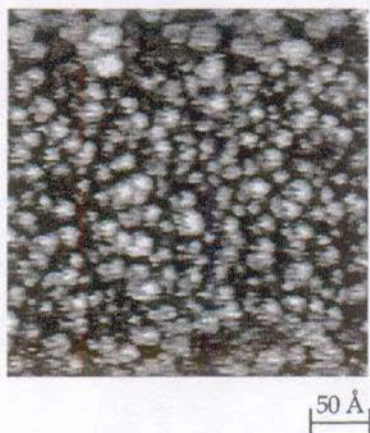
c)

Fig. 6.9: a)-c) Three-dimensional growth at T = 40K. The film morphology is atomically rough at Θ = 0.45 ML as revealed by the line scan in c). The imaging width of the second layer atom is 7±1Å. In b) only in the middle part of the STM image the topography of the Ag film (4 exposed layers) could be resolved. Image sizes: a), 125Åx125Å b) 300Åx300Å, used flux R = 1.1x10⁻³ ML/s.

At Θ = 1.1 ML the second layer is formed on nearly every former first layer island and the nucleation of the third layer has already started. In d), at the highest coverage investigated (Θ = 1.6 ML), the morphology is rough on a lateral scale of 20Å to 40Å within 5 exposed layers. Due to the finite curvature of the STM tip the substrate height level is no more resolvable in d), which was still possible in c) at the 0.5 ML lower Ag coverage (see line

a) Θ = 0.05 ML

b) Θ = 0.6 ML

c) Θ = 1.1 ML

d) Θ = 1.6 ML

100 Å

e)

f)

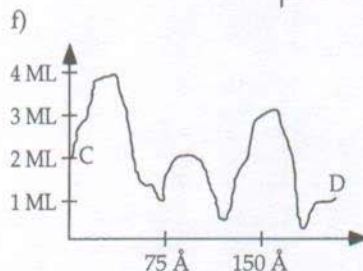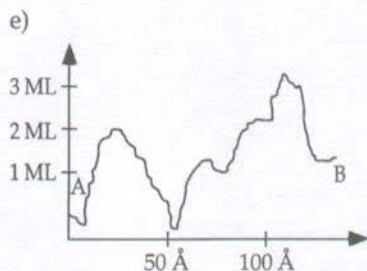**Fig. 6.10:** a)-d) Morphology as a function of coverage at T = 80K. Image size: 400Åx180Å, used flux R = 5x10⁻⁴ ML/s.

e), f) Line scans along the bars AB, CD marked in the absolute STM images c) and d) showing the different Ag layer heights.

scans in e) and f)). Thus, the multilayer growth kinetics at T = 80K is characterized by an activate interlayer diffusion from the top of the first layer islands. The mass transport between the higher layer levels, however, is strongly hindered.

Increasing of the temperatures leads to large fractal islands at low coverages, as demonstrated in Fig. 6.11 a) and b). Further deposition results in filling of

a) Θ = 0.2 ML

b) Θ = 0.5 ML

c) Θ = 0.1 ML

d) Θ = 0.5 ML

200 Å

400 Å

Fig. 6.11: a)-d) Densification of fractal islands with increasing coverage.
a), b) T = 95K and c), d) T = 130K. Image sizes: 615Åx615Å in a), b) and
1230Åx1230Å in c), d), used flux R = 1.1x10⁻³ ML/s.

the spacing between the island branches, as becomes evident by inspection
of c) and d).

As the radial extent of the aggregates is even at low coverages comparable to
the average separation between them, deposition events in-between and

157

directly onto the arms are the dominant processes for the island densification. The increase of the average branch width $\overline{W}$ with Θ is in full agreement to the coverage dependence of fractal Au islands grown on Ru(0001) at T = 300K [Hwa 91].

The following two figures focus on the interlayer diffusion at T = 130K as a function of island shape. Fig. 6.12 and 6.13 display the qualitative results for the first two Ag layers on Pt(111) and Ag homoepitaxy on Ag(111), respectively. As discussed above, an enhanced layer-by-layer growth behavior is expected for fractal islands with respect to compact ones. In the following it is demonstrated that fractal island shapes not always imply 2D-growth behavior (second Ag layer on Pt(111) and Ag/Ag(111)). On the other hand, the first Ag layer on Pt(111) gives an example that the fractal island shape is not always the responsible factor for an activated interlayer mass transport.

For the experiment shown in Fig. 6.12, first compact islands of several hundred atoms in size have been cluster aggregated, as described in 4.2.4. In a next step, further 0.1 ML have been deposited at T = 130K, i.e. with the same adatom mobility on top of the islands as present during the growth of the morphologies displayed in Fig. 6.11 c) and d). The produced hybrid islands are shown in Fig. 6.12 b). Due to the restricted step edge mobility of the subsequent deposited Ag the predeposited compact nucleus is surrounded by fractal extensions. Surprisingly, no nucleation on top of the islands occurs, although with respect to Fig. 6.11 c) the "branch width" has increased by a factor 4. Consequently, the low nucleation probability on top of the first layer islands is not promoted by the ramified shape. Within the "compact shape" terminology this can be expressed by a critical island size $L_{cr}(R = 1.1 \times 10^{-3} \text{ ML/s}, T = 130K) > 100\text{Å}$.

a) $\Theta = 0.1$ ML   b) $\Theta = 0.2$ ML
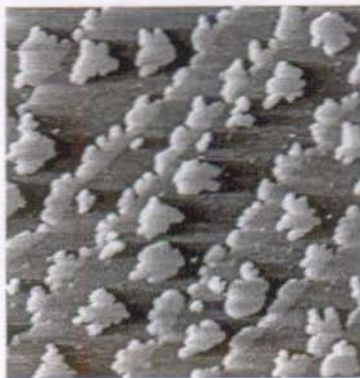
|— 300 Å —|

Fig. 6.12: a), b) Island shape independence of the interlayer diffusion for the first layer. a) Compact Ag islands produced by annealing of $\Theta = 0.1$ ML deposited at T = 50K to T = 280K. b) Subsequent growth of 0.1 ML Ag at T = 130K showing that no nucleation on top of the compact islands in a) occurs. Image sizes: 765Åx765Å, used flux R = 1.1×10^{-3} ML/s.

Hence, the loss of adatoms from the top of first Ag layer islands is independent of the island shape at T = 130K. A repetition of the same experiment at T = 80K shows that even a further reduction of the adatom mobility on top of the islands is not sufficient to nucleate the second layer on each of the compact islands. The strongly activated interlayer mass transport results either from a low "Schwoebel"- barrier $V_e^{n=1}$, a low on top diffusion barrier $E_D^{n=1}$, or a combination of both (here n denotes the number of Ag layers). For T $\geq$ 80K (and R= 1.1×10^{-3} ML/s), one cannot distinguish if the 2D growth of the first layer is mainly caused by a fast transport to the perimeter sizes or by the low energetic barrier for jump down processes.

a) Θ = 1.3 ML   b) Θ = 40 ML + 0.1 ML

├────── 400 Å ──────┤

Fig. 6.13: a), b) Hindered interlayer mass transport from the top of branched Ag islands. a) second layer island on Pt(111), b) unstrained Ag island on Ag(111).

a) Growth at T =130K of Θ = 1.3 ML: the first layer islands have coalesced and, on top of the branched second layer islands, third layer nucleation takes place.

b) Growth at T = 110K of Θ = 0.1 ML on an annealed Ag film of 40 ML: Dendritic islands obtained in Ag/Ag(111) homoepitaxy show the same effect. The interlayer diffusion from the top of the small island arms is strongly hindered. Image sizes: 1230Åx1230Å, used flux R = 1.1x10^{-3} ML/s.

Fig. 6.13 displays the opposite behavior which is found for n > 1. The two STM images show fractal islands exhibiting a low interlayer mass transport which is seen on hand of the nuclei on top of the small island branches (w ≈ 20-50Å). In a), the coverage Θ = 1.3 ML has been deposited at T = 130K leading to an almost complete first layer and ramified second layer islands. The latter have a largest branch width of about 50Å. In b) 0.1 ML has been deposited at T = 110K on an annealed 40 ML thick Ag film, i.e. this experiment is the direct comparison with the homoepitaxial system Ag/Ag(111). Again, 3D-growth is observed on branch widths w ≈ 20-30Å.

160

Thus, in this temperature range the behavior of the second layer islands on Pt(111) is qualitatively comparable with Ag/Ag(111). In both cases, the fractal island shape doesn't hinder the 3D-growth, i.e. the shape independent factors influencing the interlayer mass transport dominate. It is likely to assume that the second Ag layer on Pt(111), when grown at low temperatures, behaves "Ag(111)-like", i.e. its interlayer mass transport is governed by the same kinetic parameters. This will be discussed in further detail in 6.2.6.

In summary, for T < 150K the second and higher layers show strong hindered interlayer diffusion, while atoms deposited on top of the first Ag layer have even at $T = 80K$ a negligible kinetic barrier to step down. This difference is responsible for the kinetically caused "SK-morphology" with a critical layer number of $n^* = 1$.

6.2.3 Transition from 2D to 3D-growth with $n^* = 2$ at $170K \leq T \leq 200K$

The coverage series in Fig. 6.14 shows the growth scenario at $T = 170K$. Lateral mobility of atoms deposited on the substrate is high, leading to "step flow" growth of the first layer. In b) at $\Theta = 1.1$ ML, the first layer is nearly completed. Large second layer islands grow from the transition line between the upper substrate terrace and the first Ag layer attached to it at the ascending step. In c) at $\Theta = 2.1$ ML, the second layer is complete to 85% and homogeneous nucleation of third and forth layer islands occurs.

Atoms deposited on the first layer of the lower terrace can not overcome a repulsive potential barrier at the transition line where Ag is attached to Pt substrate steps. Its existence is proved by the fact that, without a barrier, the first layer of the upper terraces in b) would have been completed to 100%. The repulsive potential at the other side of the transition line has already

161

a) Θ = 0.6 ML

b) Θ = 1.1 ML

|— 400 Å —|

c) Θ = 2.1 ML
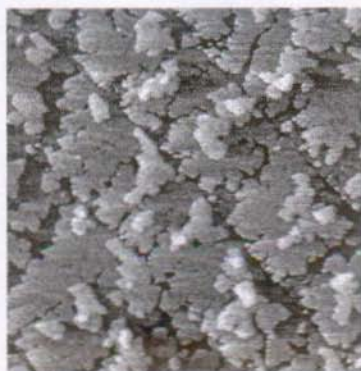
d) Θ = 2.1 ML
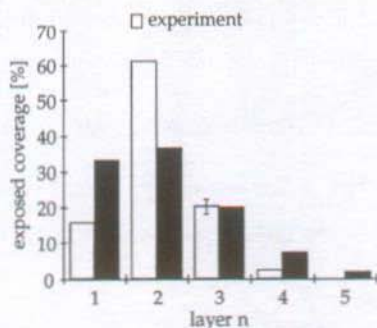
■ poisson distribution starting at Θ =1.0ML

□ experiment

Fig. 6.14: a)-c) Growth scenario at T = 170K as a function of coverage. The images show in a): the step-flow growth of the first layer, in b): the formation of second layer islands at the transition line of lower terrace Ag and higher terrace Pt and in c) the homogeneous nucleation of the third and fourth layer at further deposition. Image sizes: 1230Åx1230Å, used flux R = 1.1x10^{-3} ML/s.

d): Exposed coverages $\Theta_n - \Theta_{n+1}$ for Θ = 2.1 ML as a function of n and its comparison with the Poisson distribution for 1.1 ML on top of the first layer.

been deduced in 4.1, i.e. atoms deposited on the upper Pt-terrace cannot migrate on the lower level Ag.

162

There exist two possible reasons for the heterogeneous nucleation of the second layer islands. First, a high adatom density can only be reached far away from the first layer descending step edges, since atoms can easily overcome $V_e^{n=1}$ to step down on the substrate. The second possibility is that the potential at the Ag/Pt transition line exhibits additionally to the repulsive barrier also a small potential minimum on the lower terrace side which increases the adatom density in its proximity [Gün 93]. Independent of these two possibilities is the following conclusion: the appearance of the "step flow" growth for the layer number $n = 2$ at the same temperature as observed for $n = 1$, implies that the lateral mobilities on the substrate and on the first layer are at least comparable, i.e. $E_D^{n=1} \leq E_D^{n=0}$.

The film morphology at $\Theta = 2.1$ ML in Fig. 6.14 c) shows on relatively narrow substrate terraces ($\Lambda_S = 300$-600Å) compact third and forth layer islands of a size $L \geq 100$Å. This allows the evaluation of the different layer coverages Θ_n by simple integration of island areas without errors due to STM imaging effects at the island borderlines. In d) the exposed coverage of the nth layer, i.e. $\Theta_n - \Theta_{n+1}$, is plotted as a function of the layer number n for the STM topography in c). This form of data presentation is suitable, because ideal 3D-growth behavior (each atom stays on the level where it has been deposited) results in a simple poisson distribution of $\Theta_n - \Theta_{n-1}$ (n) (see e.g. [Coh 89]). Since the first layer grows layer-by-layer wise, the experimental data are compared with the poisson distribution starting at 1 ML, i.e. Θ_1 is set to 1 ML.

Obviously, there exists a large deviation between the ideal 3D-growth and the observed layer coverages Θ_n. Especially, the ratio Θ_3/Θ_2 is measured to 0.27, while forbidden interlayer mass transport demands $\Theta_3/\Theta_2 = 0.45$. Thus, there is a large flow of third layer atoms downward to the second

layer, which also causes the differences between the poisson and experimental values of the higher n. At T = 200K and Θ = 1.7 ML this misalignment is even worse. This is shown in the STM image in Fig. 6.15 b). The corresponding layer occupation statistic is displayed in Fig. 6.17 a), further below. The experimental ratio Θ_3/Θ_2 is only 0.05 while the ideal 3D-growth demands 0.32.

The coverage series shown in Fig. 6.15 reveals that the 2D-growth behavior at T = 200K is restricted to the second layer. At Θ = 3.9 ML 3D-pyramids on top of the smooth film structure in b) have developed (7 layers are found to be exposed simultaneously). By taking the experimental Θ_n distribution at Θ = 1.7 ML in b) as starting condition for subsequent ideal 3D-growth a reasonable agreement is obtained (see Fig. 6.15 e) and f)) between the simulated (poisson) and the observed exposed coverages Θ_n - Θ_{n-1} (n).

Therefore, the common feature of the coverage series at T = 170K and 200K is the abrupt transition from ideal 2D- to kinetic 3D-growth after completion of the second layer. Thus, in analogy to T < 150K with n* = 1, a kinetic "SK-growth scenario" with n* = 2 is observed which is caused by the activated interlayer mass transport between the third and second layer and the hindered step down diffusion for the higher layers. In the following, the phenomenon is analyzed in terms of the two kinetic barriers $E_D^{n=2}$ and $V_e^{n=2}$.

a) Θ = 1.1 ML

b) Θ = 1.7 ML

c) Θ = 2.7 ML

d) Θ = 3.9 ML

400 Å

e) Θ = 2.7 ML

f) Θ = 3.9 ML

layer n

exposed coverage of the n-th layer [%]

layer n

exposed coverage of the n-th layer [%]
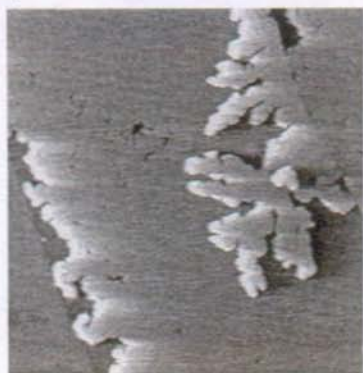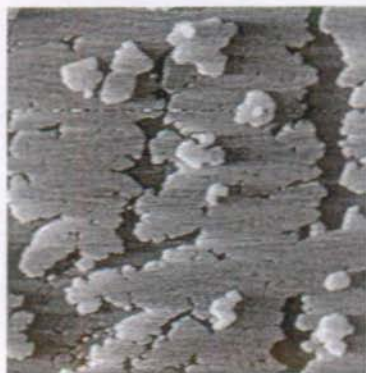
□ experiment   ■ poisson distribution starting at Θ = 1.7 ML
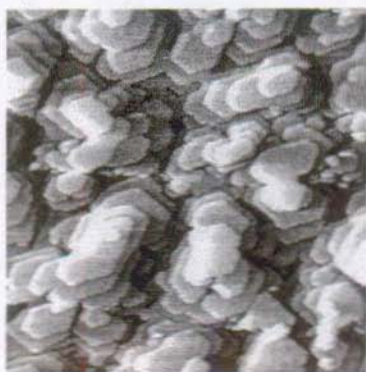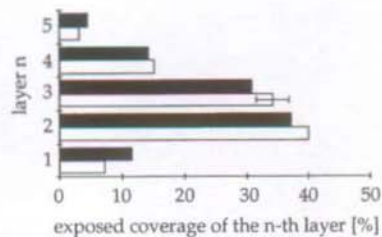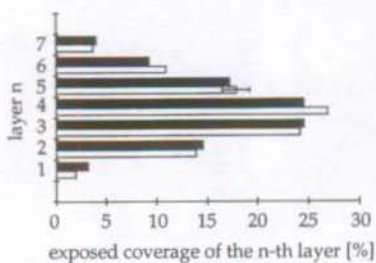
165

The lateral mobility on top of the compact second layer islands can be estimated by the average separation of the third layer islands. At T = 170K the islands are about 150Å to 200Å apart (see Fig. 6.14 c)), while at T = 200K their density is roughly a factor two smaller, leading to island separations of about 250Å to 350Å (see Fig. 6.15 b)). Close inspection of these two STM images reveals the presence of second layer step edges always between and also very close to the third layer islands. Atoms which are deposited on the exposed coverage $\Theta_2 - \Theta_3$ have, therefore, a high probability to meet a step. Thus, for 170K ≤ T ≤ 200K the adatom mobility on the second layer is high enough to ensure an effective transport to the perimeter sites. This leads to the conclusion that the interlayer diffusion is mainly governed by the "Schwoebel"-barrier $V_e^{n=2}$.

6.2.4 Simulation of the 2D to 3D-growth transition (n* = 2)

In the following, a linear interlayer transport model in the formulation of van der Vegt et al. [Veg 92] is used to simulate the kinetic SK-growth scenario with a critical film thickness of two layers (n* =2) grown at 170K ≤ T ≤ 200K. The interpretation of the simulation leads to an estimate of the barrier $V_e^{n=2}$ for a Ag atom to step down from the second layer.

On the exposed coverage of the level n $R(\Theta_n - \Theta_{n+1})$ atoms are deposited per unit time (R is the incoming flux). The fraction λ_n of these atoms jumps down to level n increasing Θ_n while the similarly expressed flux towards level n-1 decreases Θ_n. This yields the following set of coupled differential equations describing the interlayer mass transport:

$$\frac{d\Theta_n}{dt} = (1 - \lambda_{n-1}) R (\Theta_{n-1} - \Theta_n) + \lambda_n R (\Theta_n - \Theta_{n+1})$$
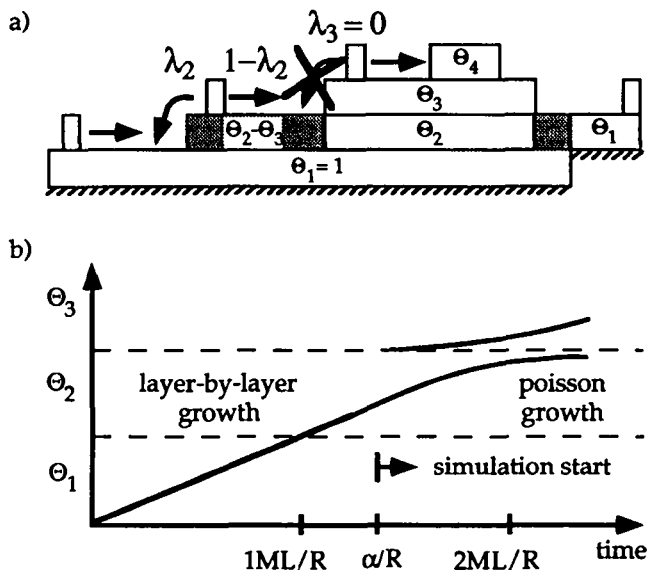
Fig. 6.16: a) Illustration of the simulation model that provides the step down diffusion barrier of the second layer. An atom landing on the exposed coverage Θ_2-Θ_3 jumps down with a probability λ_2 or attaches to a third layer island with a probability 1-λ_2. Mass transport from the higher layer levels is forbidden, i.e. $\lambda_i = 0$ for i $\geq$ 3.

b) Qualitative plot of the simulated functions $\Theta_1(t)$, $\Theta_2(t)$ and $\Theta_3(t)$ during the transition from 2D- to 3D-growth. The simulation starts after layerwise growth of the coverage $\Theta = 1$ ML + α.

The experimental situation for Ag growth on Pt(111) between T = 170K and 200K is described by $\Theta_1 \equiv 1$, $\lambda_1 = 1$ and $\lambda_n = 0$ for n = 0 and n > 2, i.e. layer-by-layer growth of the first layer and ideal 3D-growth on top of the third and higher layers. Thus, the only free parameter is λ_2, i.e. the fraction of atoms incorporated in the second layer while deposited on top. The analytical solution of the differential equations with the initial conditions $\Theta_2(t=0) = \alpha$, $\Theta_3(t=0) = \beta$, $\Theta_4(t=0) = 0$ has been calculated up to n = 4, i.e. up to the highest occupied level observed for total coverages $\Theta < 2.1$ ML:

167

$$\Theta_2(t) = 1 + A e^{(\sigma + i\kappa)t} + \overline{A} e^{(\sigma - i\kappa)t}$$

$$\Theta_3(t) = 1 + i\frac{\sigma}{\kappa} A e^{(\sigma + i\kappa)t} - i\frac{\sigma}{\kappa} \overline{A} e^{(\sigma - i\kappa)t}$$

$$\Theta_4(t) = 1 + C e^{-Rt} + (\frac{\sigma}{R\lambda} + i\frac{\sigma}{\kappa}) A e^{(\sigma + i\kappa)t} - (\frac{\sigma}{R\lambda} - i\frac{\sigma}{\kappa}) \overline{A} e^{(\sigma - i\kappa)t}$$

with $\quad \sigma = -R(1 - \lambda); \quad \kappa = R\sqrt{\lambda(1 - \lambda)};$

$$A = \frac{1}{2}\left(\alpha - 1 + i\frac{\kappa}{\sigma}(\beta - 1)\right); \quad C = \left(\frac{1-\lambda}{\lambda}(\alpha - 1) - \beta\right)$$

The qualitative form of these functions is sketched in Fig. 6.16 b). The parameter α is introduced to account for the start of the third layer nucleation at $\Theta_2 \approx 0.1$ ML (see Fig. 6.13 b) and 6.14 a)), β has been set 0. Fig. 6.17 b) shows the resulting $\lambda_2(\alpha)$ dependence yielding for each data point reasonable agreement (see Fig. 6.17 a)) with the experimental Θ_n distributions. Up to $\alpha = 0.3$ ML, the influence of the layer-by-layer growth parameter α is very weak indicating the strong dependence of the model on λ_2. The λ_2 values for $\alpha = 0.1$ ML turn out to be $\lambda_2^{170K} = 45.5\%$ and $\lambda_2^{200K} = 86.3\%$. Thus, the simulation predicts that the transport coefficients λ_2 differ between T = 170K and 200K by about a factor two.

The interpretation of this result is as follows: during its random walk an atom jumps down to the second layer with a probability $p_2 = \overline{n} \exp\{-V_e^{n=2}/kT\}$, where $\overline{n}$ is the average number of step down attempts on its trajectory. As discussed above, the adatom mobility on top of the second layer is high and sufficient perimeter sites are present. Consequently, an atom can make many attempts to overcome the step down barrier $V_e^{n=2}$. Thus, $\overline{n}$ is large enough that to a good approximation all atoms deposited on the exposed coverage $\Theta_2 - \Theta_3$ form a statistical ensemble characterized by the two parameters p_2 and $\overline{n}$.
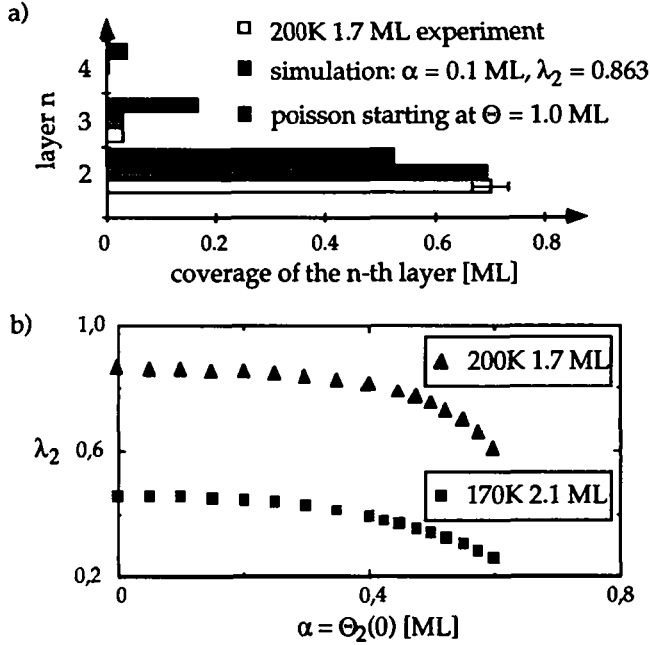
Fig. 6.17: a) Layer occupation statistic for $\Theta = 1.7$ ML at T = 200K in comparison with the ideal 3D-growth and the simulation result discussed in the text. b): Plot of the λ versus α dependence yielding a good fit of the experimental data for 1.7 ML at T = 200K and 2.1 ML at T = 170K, respectively.

Consequently, the fraction λ_2 simulated in the model is a realistic estimate of the probability p_2. Thus, $p_2 \propto \lambda_2$, with a proportionality constant close to one having a weak temperature dependence. Also $\bar{n}$ is to first order a slow varying function of T since the film morphologies at T = 170K and 200K differ only slightly and thus an adatom visits on average the same number of perimeter sites at both temperatures. By setting $\bar{n}^{170K} \approx \bar{n}^{200K}$, the ratio $\lambda_2^{170K} / \lambda_2^{200K}$ is therefore a direct measure of the step down barrier, and, by inserting the two simulated numbers, $V_e^{n=2}$ turns out to 62 meV.

169

Assuming an error interval from 0.2 to 5 for the ratio $\bar{n}^{170K}/\bar{n}^{200K}$ the $V_e^{n=2}$ estimate lies between 22 and 95 meV. A higher error assumption has to take into account compensating effects of the used approximations. While for T = 170K the higher third layer island density indicates $\bar{n}^{170K} < \bar{n}^{200K}$, the second layer step density leads to the opposite direction. At T = 200K the second layer grows more perfectly and thus $\bar{n}^{200K}$ should be smaller than $\bar{n}^{170K}$.

The estimated "Schwoebel"-barrier" $V_e^{n=2}$ of the second Ag layer on Pt(111) grown at 170K ≤ T ≤ 200K can be compared with $V_e^{Ag(111)}$ = 150±30 meV which has been derived for Ag/Ag(111) [Vri 94]. The value $V_e^{n=2}$ from the simulation is about a factor 2.5 lower than $V_e^{Ag(111)}$. This is in agreement with the observed 2D-growth behavior of the second Ag layer on Pt(111), whereas Ag/Ag(111) grows in this temperature range three-dimensionally rough [Veg 92, Ros 93, Vri 94, Amm 94].

6.2.5 High temperature growth kinetics: T > 200K

Fig. 6.18 displays the Ag film morphology grown at T = 220K. This is the lowest temperature at which relaxation patterns on the exposed Ag layers could be resolved by STM. In a) slight indentations and protrusions on the third layer islands are visible. In b) at Θ = 5 ML, the film morphology is smoother than the one for Θ = 3.9 ML at T = 200K (see Fig. 6.15 d)). Although one ML more has been deposited, the same amount of exposed layers are visible (thus one "wetting" layer more is present). As expected, at a higher temperature the interlayer mass transport is increased. This is also visible by inspection of Fig. 6.5 a) showing the relaxed film morphology at Θ = 3 ML grown at T = 250K. At his slightly higher temperature, three "wetting" layers are formed which can be compared with Fig. 6.18 a) at the same coverage.
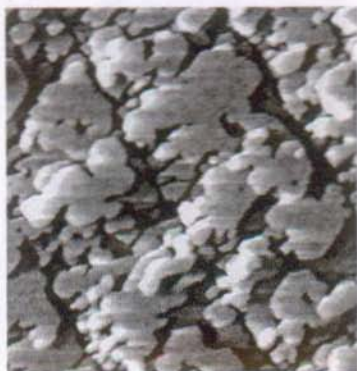
a) $\Theta = 3$ ML   b) $\Theta = 5$ ML
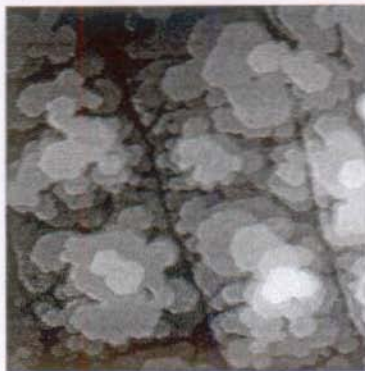
200 Å

Fig. 6.18: a), b) Film morphology at T = 220K revealing in a) the thermal onset of the strain relief in the film and in b) the pyramidal growth on top of three completed layers. Image sizes: 770Åx770Å, used flux R = 3.5×10^{-3} ML/s.

Fig. 6.19 shows film morphology grown at room temperature as a function of increasing coverage. Heterogeneous nucleation at the step edges takes place even on large terraces ($\Lambda_S > 2000$Å) up to about 10 ML. The Ag film reflects therefore the substrate step structure, i.e. "step flow" growth of the higher layers occur. The growth is not perfect as revealed by the line scan in e) showing that up to 5 ML deep holes are produced for the 9 ML thick film in c). Thus, at T = 300K the evaporation of atoms from the step edges is not yet thermally activated to close these holes. This is in accordance with SPA-LEED observations on Ag/Ag(111) [Amm 94].

Fig. 6.19: (next page) a)-d) SK-growth scenario of room temperature deposited Ag resulting in a critical layer number of $n^* \approx 10$. Image sizes: a)-c) 2460Åx2460Å, d) 3880Åx3880Å; used flux R = 1.1×10^{-3} ML/s. e), f): Line scans along the bars AB, CD marked in the absolute STM images c) and d) showing up to 5 layer deep holes at $\Theta = 9$ ML and up to 10 layer high 3D-pyramids at $\Theta = 25$ ML.

171

a) Θ = 3.0 ML

b) Θ = 6.0 ML

c) Θ = 9.0 ML

d) Θ = 25.5 ML

A ————————→ B

D

C

800 Å

800 Å

e)

1 ML

A

6 ML

B

300 Å   600 Å

f)

1 ML

C

11 ML

D

500 Å   1000 Å

172
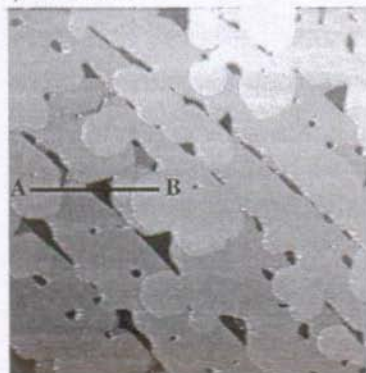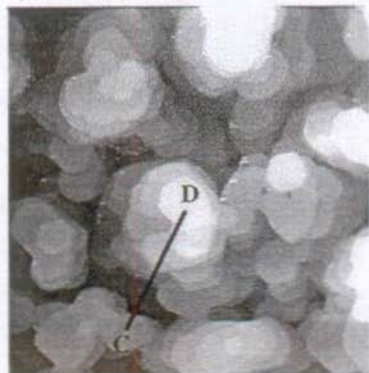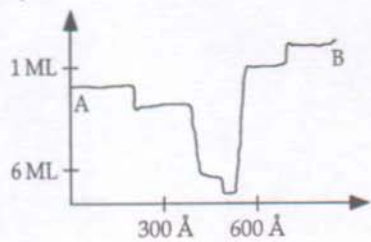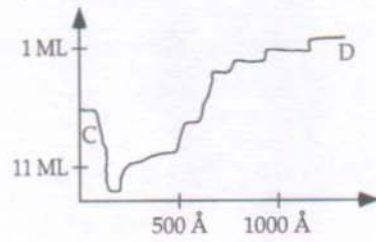
500 Å   200 Å

Fig. 6.20: a), b) Morphology of a 25 ML Ag film grown at 450K in a) and annealed to 600K on a highly stepped area in b). The inset in b) shows the enlargement of some screw dislocations and stacking faults. Image sizes: 2000Åx2000Å, inset in b) 430Åx430Å, used flux R: a) 1.6x10^{-2} ML/s b) 3.5x10^{-2} ML/s.

In the STM image in Fig. 6.19 d) the "SK-growth scenario" reappears at Θ = 25 ML. The line scan in f) reveals 10 layer high growth pyramids. The transition to homogeneous nucleation and hindered interlayer mass transport depends on the terrace width Λ_S. The critical layer number is roughly $n^*(T= 300K) = 10$ for $\Lambda_S \approx 500$Å.

In Fig. 6.20 the transition to the thermodynamic FM-growth mode is shown. The 25 ML thick film in a) has been grown at T = 450K and is smooth with respect to the room temperature experiment (see Fig. 6.19 d)). After annealing to T = 600K, the in a) remaining imperfections of the deposit vanish, even on highly stepped areas like those shown in b). Evaporation from the step edges fills holes and leads to a "wetting" multilayer film. The shown screw dislocations and stacking faults seem to be typically for Ag and have also been observed on a vicinal Ag (111) surface [Wol 90, Wol 91] and

173

on a Ag film grown on Si(111) at T = 80K with a further anneal to 300K-400K [Mey 94].

6.2.6 Strain relief mediated two-dimensional growth

The STM results derived in the sections 6.2.2 to 6.2.5 give a consistent picture of the Ag/Pt(111) multilayer growth kinetics when compared with the well-studied growth kinetics of Ag/Ag(111) [Veg 92, Ros 93, Vri 94, Amm 94]. Its interlayer mass transport is strongly hindered leading to a transition from 3D-growth behavior to "step flow" growth with increasing temperature (threshold temperature ≈ 400K). The interlayer diffusion is governed by a large "Schwoebel"-barrier" $V_e^{Ag(111)}$ = 150±30 meV as deduced in a recent STM-study by Vrijmoeth et al. [Vri 94]. Indeed, the lateral mobility of a Ag atom on Ag(111) is higher than on Pt(111) ($E_D^{Ag(111)}$ ≤ 100 meV < $E_D^{Pt(111)}$ = 157 meV [Bro 94]). Thus, the transport of atoms to the perimeter sites seems not to be the hindering factor.

As derived in 6.2.3, the mobility on top of the strained first Ag layer is at least comparable to the one on Pt(111) [Bro 94]. This corroborates the intuitive picture that the compression of the Ag layer should decrease the corrugation of the adsorption potential, thus increase the adatom mobility. Furthermore, it has been deduced that the mobility on top of the second Ag layer grown at 170K ≤ T ≤ 200K influences not substantially the interlayer mass transport. Thus, it is likely to assume that the adatom mobility plays only a minor role for the interlayer diffusion of Ag/Pt(111), as it is the case for unstrained Ag layers in Ag/Ag(111) homoepitaxy.

For T > 200K the Ag layers are relaxed and the diffusivity may decrease due to the domain walls separating the areas of compressed Ag. On the other hand, this "negative" mobility effect on the interlayer diffusion has not to

174

be the dominating factor of the interlayer diffusion. As will be seen in the following, the higher temperature morphologies fit well in a picture which focuses solely on the "Schwoebel"-barrier as the dominating factor governing the interlayer mass transport.

The observations in the three temperature ranges treated above propose the following relations explaining the $n^*(T)$ dependence:

$$T < 150K: \qquad n^* = 1 \qquad V_e^{n=2} \approx V_e^{Ag(111)}$$

$$170K < T < 200K: \qquad n^* = 2 \qquad V_e^{n=2} \approx 60\,meV < V_e^{n \geq 3} \approx V_e^{Ag(111)}$$

$$T > 200K: \qquad n^* \geq 3 \qquad V_e^{n=n^*} \approx V_e^{Ag(111)} \approx 150\,meV$$

Thus, the multilayer growth kinetics can be explained by the simple relation that hindered mass transport is attributed to "strain-free" Ag, while strained Ag is connected with a small or vanishing "Schwoebel"-barrier. Changes of the step down barriers V_e^n with temperatures are caused by the temperature (and film thickness) dependence of the strain relieve mechanism leading to different layer structures.

The proposed scenario justifies the name "kinetic SK-mechanism", since the obtained nonequilibrium morphologies are caused by the strain present in the film layers. This kinetic effect is therefore in close analogy to the main reason for the thermodynamic film instability leading to the SK-growth mode (see 2.2.2).

For $T < 150K$, the fractal island shape has no influence on the interlayer diffusion of the first and second Ag layer, as discussed in 6.2.2. The direct comparison with Ag homoepitaxy in Fig. 6.13 suggests that the fractal branches of the second layer islands are too small to completely adapt the

lattice of the pseudomorphic first layer, i.e lateral Ag-Ag interaction may dominate and therefore Ag(111) behavior establishes, i.e. $V_e^{n=2} \approx V_e^{Ag(111)}$.

The correlation between the change in growth behavior and the transition in film structure is most pronounced around T = 200K. For T > 200K the stored misfit strain is relieved as resolved by STM. On the other hand, for 170K ≤ T ≤ 200K no relaxation patterns could be detected. Thus, basically the second Ag layer is in registry with the Pt(111) surface but stays at the threshold to relax laterally. The growth kinetics can be interpreted that at the step edges the strain is already partially relieved which may facilitate exchange processes to step down (see Fig. 2.8 b)) resulting in a lower barrier $V_e^{n=2} < V_e^{Ag(111)}$.

On the other hand, the third and higher layer islands exhibit a "Ag(111)-like" behavior, i.e. $V_e^{n \geq 3} \approx V_e^{Ag(111)}$, since the substrate influence decays with increasing film height. This argumentation is supported by the pyramidal shape of the 3D-overgrowth on top of the two "wetting" layers (see Fig. 6.14 d)). To grow these pyramids demands a low island density at the bottom and the nucleation of the higher layers while the former ones are still small [Gün 93]. Thus, the growth of the 3D-pyramids occurs presumably because successive layers in these pyramids grow from one single nucleus each. Consequently, for n ≥ 3 the critical island sizes L_{cr} are small (around 100 to 150Å) which does not favor relaxation of the island, as discussed for T < 150K. In consequence, the assumption of unstrained step edges structures with $V_a^{n \geq 3} \approx V_e^{Ag(111)}$ is reasonable in the temperature range 170K < T < 200K.

Between T = 200K and 300K the critical layer height n* increases progressively up to n* ≈ 10. In the same temperature range also the relaxation kinetics of the Ag layers starts which seems to be reflected in the

growth kinetics by an increasing "Schwoebel"-barrier as the film height increases. For T = 300K this transition of the film structure at 9-10 ML has been detected in He-diffraction measurements [Rom 94]. At this thickness a weakly modulated incommensurate structure with Ag(111) interplanar lattice constant has been detected. This is well correlated with the change of the growth behavior at $n^* \approx 10$ and fits well in the above proposed scenario.

It is instructive to compare the FM-growth mode and the strain relief of Ag/Pt(111) with similar heteroepitaxial systems. Au, Co and Cu layers on Ru(0001) are comparably mismatched when adsorbed on the close-packed Ru substrate: Au is compressed by 6.8%; Co and Cu are expanded by 7.0% and 5.5%, respectively. The relations of the surface and film free energies are similar to Ag/Pt(111): $\gamma_{Ru} = 1.20 \gg \gamma_{Au} = 0,70, \gamma_{Co} = 0.87, \gamma_{Cu} = 0.65$ eV/atom [Mie 78]. Au and Co on Ru(0001) exhibit the SK-growth mode: after annealing to T ≥ 925K large three-dimensional Au/Co-crystallites of several layers height are observed. The critical layer height is $n^* = 2$ for Au and $n^* = 1$ for Co. In the STM studies of these systems no indications for a strain relief mechanism of the film layers have been found [Gün 93].

Cu/Ru(0001), on the other hand, is the interesting case where the misfit strain is relieved upon annealing to T = 520K [Pöt 91], This system is, therefore, a good candidate to compare the relation between multilayer growth behavior and strain relief with the one obtained for Ag/Pt(111). Unfortunately, neither the detailed multilayer growth kinetics as a function of temperature nor the thermodynamic growth mode of Cu/Ru(0001) is reported. STM images of high coverage (> 5 ML) Cu films grown at T = 300K exhibits the same pyramidal structure as observed for Ag/Pt(1111) at T = 200K [Gün 93]. Since the misfit strain relieve of the second Cu layer on Ru(0001) sets in at T = 520K it may be speculated that this film morphology

obtained at T = 300K is a comparable "transition state" towards the FM-growth mode as observed for Ag/Pt(111) at T = 200K.

7. Outlook

In this thesis one specific heteroepitaxial system has been studied and a consistent picture of the model system "Ag vapor deposited on Pt(111)" has been developed by means of variable temperature STM.

Many parameters which determine thin film growth were fixed by the choice of the two materials Ag and Pt and the lattice symmetry of the substrate. The richness of epitaxial phenomena, however, becomes aware by comparing different heteroepitaxial systems. The informations obtained during this work for one special system may help to establish general rules of metal-on-metal epitaxy. Important effects found in Ag/Pt(111) epitaxy and other systems (e.g. [Aug 94]) can, by the means of educated guess, be transferred to other film/substrate combinations. Hereafter, the detailed growth behavior of adsorbate A on substrate B may be predictable.

Nevertheless, there remain also for the system Ag/Pt(111) interesting fields for further studies:

a) It has been demonstrated that detailed structuring on the nanometer scale by using solely externally controlled growth parameter is possible. In the future, progress in this field may base on the knowledge that was acquired during this work.

b) The influence of misfit strain proved to play an important role in this system. The explanation of the phenomenon strain on an atomic scale, on the other hand, remains to be a question of great importance.

For further progress in the understanding of the system Ag/Pt(111) the improvement of the performance of the variable temperature STM ("atomic resolution") will help to solve remaining questions.

8. References

[Abr 94]   "Studying transient mobility and energy loss using scanning tunneling microscopy", M. J. Abrams and P. S. Weiss, Surf. Sci. **312** (1994) 1.

[Alt 94]   "Growth of Rh on Au(111): surface intermixing of immiscible metals", E. I. Altman and R. J. Colton, Surf. Sci. **304** (1994) L400.

[Amm 94]   "The multilayer growth mode in the epitaxy of Ag on Ag(111) analyzed by SPALEED", C. Ammer, T. Schaefer, C. Teichert, K. Meinel and M. Klaua, Surf. Sci. **307-309** (1994) 570.

[Arn 87]   "Laser-frequency mixing in the junction of a scanning tunneling microscope", L. Arnold and W. Krieger, Appl. Phys. Lett. **51** (1987) 786.

[Aug 94]   "The Effects of Peanut Butter on the Rotation of the Earth", G. August, et al., J. Irrepr. Res. **39** (1994) 22.

[Bak 76]   "Theory of the Structural Phase Transformations in Tetrahiafulvalene-Tetracyanoquinodimethane (TTF-TCNQ)", P. Bak and V. Emery, Phys. Rev. Lett. **36** (1976) 978.

[Bak 82]   "Commensurate phases, incommensurate phases and the devil's staircase", P. Bak, Rep. Prog. Phys. **45** (1982) 587.

[Bar 61]   "Tunneling from a many-particle Point of View", J. Bardeen, Phys. Rev. Lett. **6** (1961) 57.

[Bar 79]   "Crystal Growth: A Tutorial Approach", W. Bardsley, D. T. J. Hurle and J. B. Mullin Eds., "North-Holland Series in Crystal Growth 2", (North-Holland, 1979).

[Bar 88]   "Theory of the local tunneling spectrum of a vibrating adsorbate", A. Baratoff and B. N. J. Persson, J. Vac. Sci. Technol. **A 6** (1988) 331.

[Bar 90]   "Scanning tunneling microscopy observations on the reconstructed Au(111) surface: Atomic structure, long-range superstructure, rotational domains and surface defects", J. V. Barth, H. Brune, G. Ertl and R. J. Behm, Phys. Rev. **B 42** (1990) 9307.

[Bar 941]   "Dendritic Islands in Metal-on-Metal Epitaxy I: Shape-Transitions and Diffusion at Island Edges", M. C. Bartelt and J. W. Evans, Surf. Sci. **314** (1994) L829.

[Bar 942]   "Mesoscopic structural transformations on the Au(111) surface induced by alkali metal adsorption", J. V. Barth, R. J. Behm and G. Ertl, Surf. Sci. **302** (1994) L319.

[Bas 78]   "Diffusion of single Adatoms of Platinum, Iridium and Gold on Platinum surfaces", D. W. Bassett and P. R. Webber, Surf. Sci. 70 (1978) 520.

[Bau 58]   "Phänomenologische Theorie der Kristallabscheidung an Oberflächen", E. Bauer, Zeitschr. f. Kristallog. 110 (1958) 372.

[Bau 82]   "Chemisorption of metals on metals and on semiconductors", E. Bauer in "Interfacial Aspects of Phase Transformation", B. Mutaftschiev Eds., (Reidel, 1982), p. 411.

[Bau 86]   "Structure and growth of crystalline superlattices: From monolayer to superlattice", E. Bauer and J. H. v. d. Merve, Phys. Rev. B 33 (1986) 3657.

[Bau 87]   "Phase transitions on single-crystal surfaces and in chemisorbed layers", E. Bauer in "Structure and Dynamics of Surfaces II", W. Schommers and P. v. Blanckenhagen Eds., (Springer, 1987), p. 115.

[Bec 35]   "Kinetische Behandlung der Keimbildung in übersättigten Dämpfen", R. Becker and W. Döring, Ann. Phys. 24 (1935) 719.

[Bec 93]   "Two-Dimensional Microstructures of Submonolayer Ag on Pt(111) induced by elastic strain", A. F. Becker, G. Rosenfeld, B. Poelsema and G. Comsa, Phys. Rev. Lett. 70 (1993) 477.

[Beh 86]   "Scanning Tunneling Microscopy", R. J. Behm and W. Hösler in "Chemistry and Physics of Solid Surfaces VI", R. Vanselow and R. F. Howe Eds., (Springer, 1986), p. 361.

[Beh 90]   "Scanning Tunneling Microscopy and Related Methods", R. J. Behm, N. Garcia and H. Rohrer Eds., "NATO ASI Series E 184", (Kluwer, 1990).

[Ben 85]   "Experimental Demonstration of the Role of Anisotropy in Interfacial Pattern Formation", E. Ben-Jacob, R. Godbey, N. D. Goldenfeld, J. Koplik, H. Levine, T. Mueller and L. M. Sander, Phys. Rev. Lett. 55 (1985) 1315.

[Ber 88]   "Role of strain and growth conditions on the growth front profile of $In_xGa_{1-x}As$ on GaAs during the pseudomorphic growth regime", P. R. Berger, K. Chang, P. Bhattacharya, J. Singh and K. K. Bajaj, Appl. Phys. Lett. 53 (1988) 684.

[Ber 92]   "Photon Emission From the Scanning Tunneling Microscope", R. Berndt, Ph.D. Thesis, Universität Basel, (1992).

[Ber 93]   "Photon-Emission at Molecular Resolution Induced by a Scanning Tunneling Microscope", R. Berndt, R. Gaisch, J. K. Gimzewski, B. Reihl, R. R. Schlittler, W. D. Schneider and M. Tschudy, Science 262 (1993) 1425.

182

[Bes]   Besocke-Delta-Phi-Elektronik, Postfach 2243, D-52428 Jülich, Germany.

[Bes 87] *"An easily operable Scanning Tunneling Microscope"*, K. Besocke, Surf. Sci. **181** (1987) 145.

[Bin 81] *"Tunneling through a controllable vacuum gap"*, G. Binnig, H. Rohrer, C. Gerber and E. Weibel, Appl. Phys. Lett. **40** (1981) 178.

[Bin 82] *"Surface Studies by Scanning Tunneling Microscopy"*, G. Binnig, H. Rohrer, C. Gerber and E. Weibel, Phys. Rev. Lett. **49** (1982) 57.

[Bin 861] *"Atomic Force Microscope"*, G. Binnig, C. F. Quate and C. Gerber, Phys. Rev. Lett. **56** (1986) 930.

[Bin 862] *"Single-tube three-dimensional scanner for scanning tunneling microscopy"*, G. Binnig and D. P. E. Smith, Rev. Sci. Instrum. **57** (1986) 1688.

[Bin 863] *"Scanning tunneling microscopy"*, G. Binnig and H. Rohrer, IBM J. Res. Develop. **30 (4)** (1986) 355.

[Bin 87] *"Geburt und Kindheit der Rastertunnelmikroskopie"*, G. Binnig and H. Rohrer, Phys. Bl. **7** (1987) 282.

[Bla 92] *"Diffusion properties and collisional dynamics of Ag adatoms and dimers on Pt(111)"*, P. Blandin and C. Massobrio, Surf. Sci. **279** (1992) L219.

[Bla 941] *"Evidence for strain induced 2D roughening in Ag islands on Pt(111)"*, P. Blandin, C. Massobrio and P. Ballone, Phys. Rev. Lett. **72** (1994) 3072.

[Bla 942] *"Nucleation and growth of metallic submonolayers on compact metal surfaces"*, P. Blandin, C. Massobrio and P. Ballone, Phys. Rev. B **49** (1994) 16637.

[Bon 93] *"Scanning Tunneling Microscopy and Spectroscopy"*, D. A. Bonnell Eds., (VCH Publishers, 1993).

[Bot 92] *"The homoepitaxial growth of Pt on Pt(111) studied with STM"*, M. Bott, T. Michely and G. Comsa, Surf. Sci. **272** (1992) 161.

[Bot 93] *"Pt(111) reconstruction induced by enhanced gas-phase chemical potential"*, M. Bott, M. Hohage, T. Michely and G. Comsa, Phys. Rev. Lett. **70** (1993) 1489.

[Bro 94] K. Bromann, personal communication.

[Bru 87] *"Morphological Transitions in solid epitaxial overlayers"*, R. Bruinsma and A. Zangwill, Europhys. Lett. **4** (1987) 729.

[Bru 92]   *"Struktur, Reaktivität und elektronische Eigenschaften von Adsorbaten auf einer Al(111) Oberfläche"*, H. Brune, Ph.D. Thesis, Freie Universität Berlin, (1992).

[Bru 941]   Calculations and their interpretation has been performed by H. Brune.

[Bru 942]   The atomic model has been developed by H. Brune.

[Buc 82]   *"Segregation and Ordering at Alloy Surfaces Studied by Low-Energy Ion Scattering"*, T. M. Buck in "Chemistry and Physics of Solid Surfaces IV", R. Vanselow and R. F. Howe Eds., (Springer, 1982), p. 435.

[Buc 93]   *"Thermally induced disorder and conformational defects of alkane monolayers on graphite"*, J.-P. Bucher, H. Röder and K. Kern, Surf. Sci. 289 (1993) 370.

[Buk 86]   *"Transitions of viscous fingering patterns in nematic liquid crystals"*, A. Buka, J. Kertész and T. Vicsek, Nature 323 (1986) 424.

[Bur 49]   *"Role of Dislocations in Crystal Growth"*, W. K. Burton, N. Cabrera and F. C. Frank, Nature 163 (1949) 398.

[Bur 51]   *"The growth of crystals and the equilibrium structure of their surfaces"*, W. K. Burton, N. Cabrera and F. C. Frank, Trans. Roy. Soc. A 243 (1951) 299.

[Car 88]   *"Finite element analysis of PZT tube scanner motion for scanning tunneling microscopy"*, R. G. Carr, J. Microscopy 152 (1988) 379.

[Cha 85]   *"Molecular Beam Epitaxy and Heterostructures"*, L. L. Chang and K. Ploog Eds., "NATO ASI Series E: Applied Sciences No.87 (Martinus Nijhoff Publishers, 1985).

[Cha 91]   *"Nucleation of Ordered Ni Island Arrays on Au(111) by Surface-Lattice Dislocations"*, D. D. Chambliss, R. J. Wilson and S. Chiang, Phys. Rev. Lett. 66 (1991) 1721.

[Che 88]   *"Theory of scanning tunneling spectroscopy"*, C. J. Chen, J. Vac. Sci. Technol. A 6 (1988) 319.

[Che 901]   *"Origin of Atomic Resolution on Metal Surfaces in Scanning Tunneling Microscopy"*, C. J. Chen, Phys. Rev. Lett. 65 (1990) 448.

[Che 902]   *"Tunneling matrix elements in three-dimensional space: The derivative rule and the sum rule"*, C. J. Chen, Phys. Rev. B 42 (1990) 8841.

[Che 911]   *"Role of atomic force in tunneling-barrier measurements"*, C. J. Chen and R. J. Hamers, J. Vac. Sci. Technol. B 9 (1991) 503.

[Che 912]   *"Attractive interatomic force as a tunneling phenomenon"*, C. J. Chen, J. Phys.: Condens. Matter 3 (1991) 1227.

[Che 92]   "In-situ characterization of tip electronic structure in scanning tunneling microscopy", C. J. Chen, Ultramicroscopy 42-44 (1992) 147.

[Che 93]   "Introduction to Scanning Tunneling Microscopy", C. J. Chen, (Oxford University Press, 1993).

[Chr 75]   "The Theory of Transformations in Metals and Alloys (Part I)", J. W. Christian, (Pergamon Press, 1975).

[Coh 89]   "Birth-Death Models of Epitaxy", P. I. Cohen, G. S. Petrich, P. R. Pukite, G. J. Whaley and A. S. Abrott, Surf. Sci. 210 (1989) 222.

[Cro 93]   "Spectroscopy of a single adsorbed atom", M. F. Crommie, C. P. Lutz and D. M. Eigler, Phys. Rev. B 48 (1993) 2851.

[Das 75]   "Films on Solid Surfaces", J. G. Dash, (Academic Press, 1975).

[Dav 82]   "The growth and chemisorptive properties of Ag and Au monolayers on Pt single crystal surfaces: An AES, TDS and LEED Study.", P. W. Davies, M. A. Quinlan and G. A. Somorjai, Surf. Sci. 121 (1982) 290.

[Dav 86]   "High-resolution He-scattering apparatus for gas-surface interaction studies", R. David, K. Kern, P. Zeppenfeld and G. Comsa, Rev. Sci. Instrum. 57 (1986) 2771.

[Daw 83]   "Semiempirical, Quantum Mechanical Calculation of Hydrogen Embrittlement in Metals", M. S. Daw and M. I. Baskes, Phys. Rev. Lett. 50 (1983) 1285.

[Daw 93]   "The embedded-atom method: a review of theory and applications", M. S. Daw, S. M. Foiles and M. I. Baskes, Mat. Sci. Rep. 9 (1993) 251.

[Dür 86]   "Experimental Observation of Forces Acting during Scanning Tunneling Microscopy", U. Dürig, J. K. Gimzewski and D. W. Pohl, Phys. Rev. Lett. 57 (1986) 2403.

[Dür 88]   "Force sensing in scanning tunneling microscopy: Observation of adhesion forces on clean metal surfaces", U. Dürig, O. Züger and D. W. Pohl, J. Microscopy 152 (1988) 259.

[Eck 90]   "Asymptotic Shape of Diffusion-Limited Aggregates with Anisotropy", J. P. Eckmann, P. Meakin, I. Procaccia and R. Zeitak, Phys. Rev. Lett. 65 (1990) 52.

[Ege 89]   "Reflection High-Energy Electron Diffraction (RHEED) Oscillations at 77K", W. F. Egelhoff and I. Jacob, Phys. Rev. Lett. 62 (1989) 921.

[Ehr 661]   "Atomic View of Surface Self-Diffusion: Tungsten on Tungsten", G. Ehrlich and F. G. Hudda, J. Chem. Phys. 44 (1966) 1039.

[Ehr 662]   "Atomic Displacements in One- and Two-Dimensional Diffusion", G. Ehrlich, J. Chem. Phys. 44 (1966) 1050.

[Ehr 84]   "An Atomic View of Crystal Growth", G. Ehrlich in "Chemistry and Physics of Solid Surfaces V", R. Vanselow and R. Howe Eds., (Springer, 1984), p. 283.

[Ehr 91]   "Direct observations of the surface diffusion of atoms and clusters", G. Ehrlich, Surf. Sci. 246 (1991) 1.

[Eig 90]   "Positioning single atoms with a scanning tunneling microscope", D. M. Eigler and E. K. Schweizer, Nature 344 (1990) 524.

[Ein 05]   "Über die von der molekularkinetischen Theorie der Wärme geforderte Bewegung von in ruhenden Flüssigkeiten suspendierten Teilchen", A. Einstein, Ann. Phys. 17 (1905) 549.

[Eis 93]   "Growth and structure of Ag on Pd(111) studied by photoelectron forward scattering using a two-dimensional display-type analyzer", B. Eisenhut, J. Stober, R. Rangelov and T. Fauster, Phys. Rev. B 47 (1993) 12980.

[Elm 94]   "Submonolayer Magnetism of Fe(110) on W(110): Finite Width Scaling of Stripes and Percolation between Islands", H. J. Elmers, J. Hauschild, H. Höche, U. Gradmann, H. Bethge, D. Heuer and U. Köhler, Phys. Rev. Lett. 73 (1994) 898.

[Ern 92]   "Nucleation and diffusion of Cu adatoms on Cu(100): A helium-atom-beam scattering study", H.-J. Ernst, F. Fabre and J. Lapujoulade, Phys. Rev. B 46 (1992) 1929.

[Fal 901]   "Surface, interface, and thin-film magnetism", L. M. Falicov, et al., J. Mater. Res. 5 (1990) 1299.

[Fal 902]   "Fractal Geometry: Mathematical Foundations and Applications", K. Falconer, (J. Wiley, 1990).

[Fei 941]   "Diffusion Barrier for a Ag Adatom on Pt(111)", P. J. Feibelman, Surf. Sci. 313 (1994) L801.

[Fei 942]   "Energetics of Pt adsorption on Pt(111)", P. J. Feibelman, J. S. Nelson and G. L. Kellogg, Phys. Rev. B. 49 (1994) 10548.

[Feu 87]   "Tunneling and Scanning Tunnel Microscopy: a Critical Review", T. E. Feuchtwang and P. H. Cutler, Physica Scripta 35 (1987) 132.

[Fin 84]   "Lattice Steps and Adatom Binding on W(211)", H.-W. Fink and G. Ehrlich, Surf. Sci. 143 (1984) 125.

[Fis 93]   "Three-dimensional localization of electrons on Ag islands", R. Fischer, T. Fauster and W. Steinmann, Phys. Rev. B 48 (1993) 15496.

[For 90]   "What do we mean by 'work function'", R. G. Forbes in "Scanning Tunneling Microscopy and Related Methods", R. J. Behm, N. Garcia and H. Rohrer Eds., (Kluwer, 1990), p. 163.

[Fra 491]   "One-dimensional dislocations. 1. Static theory", F. C. Frank and J. H. v. d. Merve, Proc. Roy. Soc. A 198 (1949) 205.

[Fra 492]   "One-dimensional dislocations. 2. Misfitting monolayers and oriented overgrowth", F. C. Frank and J. H. v. d. Merve, Proc. Roy. Soc. A 198 (1949) 216.

[Fre 38]   J. Frenkel and T. Kontorova, Phys. Z. Sov. 13 (1938) 1.

[Fro 89]   "Coarse tip distance adjustment and positioner for a scanning tunneling microscope", J. Frohn, J. F. Wolf, K. Besocke and M. Teske, Rev. Sci. Instrum. 60 (1989) 1200.

[Gen 85]   "Wetting: statics and dynamics", P. G. d. Gennes, Rev. Mod. Phys. 57 (1985) 827.

[Gen 92]   "Growth modes and relaxation mechanisms of strained InGaAs layers grown on InP(001)", M. Gendry, V. Drouot, C. Santinelli, G. Hollinger, C. Miossi and M. Pitaval, J. Vac. Sci. Technol. B 10 (1992) 1829.

[Gie 93]   "Time dependence of Step Fluctuations on Vicinal Cu(1 1 19) Surfaces Investigated by Tunneling Microscopy", M. Giesen-Seibert, R. Jentjens, M. Poensgen and H. Ibach, Phys. Rev. Lett. 71 (1993) 3521.

[Gil 63]   "The Art and Science of Growing Crystals", J. J. Gilman Eds., (John Wiley & Sons, 1963).

[Gim 88]   "Photon emission with the scanning tunneling microscope", J. K. Gimzewski, B. Reihl, J. H. Coombs and R. R. Schlittler, Z. Phys. B 72 (1988) 497.

[Gir 94]   "Dynamics of high index step equilibrium fluctuations as observed by scanning tunneling microscopy", J. C. Girard, S. Gauthier, S. Rousset, W. Sacks, S. d. Cheveigné and J. Klein, Surf. Sci. 301 (1994) 245.

[Gla 41]   "The Theory of Rate Processes", S. Glasstone, K. J. Laidler and H. Eyring, (McGraw-Hill, 1941).

[Gra 88]   "Thin film growth modes, wetting and cluster nucleation", M. H. Grabow and G. H. Gilmer, Surf. Sci. 194 (1988) 333.

[Gri 86]   "Morphology and Microstructure in Electrochemical Deposition of Zinc", D. Grier, E. Ben-Jacob, R. Clarke and L. M. Sander, Phys. Rev. Lett. 56 (1986) 1264.

[Gug 80]   "Caractérisation par spectrométrie Auger et décapage ionique des modes de croissance et de l'interface dans le couple Ag - Pd", J. M. Guglielmacci and M. Gillet, Thin Solid Films 68 (1980) 407.

[Gün 92]   "Scanning Tunneling Microscopy I - III", H.-J. Güntherodt and R. Wiesendanger Eds., "Springer Series in Surface Sciences 20, 28, 29", (Springer, 1992/1993).

[Gün 93] *"Microscopic Aspects of Thin Metal Film Epitaxial Growth on Metallic Substrates"*, C. Günther, S. Günther, E. Kopatzki, R. Q. Hwang, J. Schröder, J. Vrijmoeth and R. J. Behm, Ber. Bunsenges. Phys. Chem. **97** (1993) 522.

[Gün 94] *"Anisotropy in Nucleation and Growth of Two-dimensional Islands during Homoepitaxy on "Hex" Reconstructed Au(100)"*, S. Günther, E. Kopatzki, M. C. Bartelt, J. W. Evans and R. J. Behm, Phys. Rev. Lett. **73** (1994) 553.

[Hah 93] *"Structure and complete chemical passivation of Pt(997)"*, E. Hahn, A. Fricke, H. Röder and K. Kern, Surf.Sci. **297** (1993) 19.

[Hah 94] *"Structure and Reactivity of vicinal Pt and low-index Cu/Pd Surfaces"*, E. Hahn, Ph.D. Thesis No. 1218, EPFL Lausanne, (1994).

[Hal 87] *"Observation of Atomic Corrugation on Au(111) by Scanning Tunneling Microscopy"*, V. M. Hallmark, S. Chiang, J. F. Rabolt, J. D. Swalen and R. J. Wilson, Phys. Rev. Lett. **59** (1987) 2879.

[Ham 89] *"Atomic-Resolution Surface Spectroscopy with the Scanning Tunneling Microscope"*, R. J. Hamers, Annu. Rev. Phys. Chem. **40** (1989) 531.

[Har 73] *"Crystal Growth: An Introduction"*, P. Hartman Eds., "North-Holland Series in Crystal Growth 1", (North-Holland, 1973).

[Har 85] *"Observation of Soliton Reconstruction of Au(111) by High-Resolution Helium-Atom Diffraction"*, U. Harten, A. M. Lahee, J. P. Toennies and C. Wöll, Phys. Rev. Lett. **54** (1985) 2619.

[Här 93] *"Growth and properties of thin Ag films on Pt(111) surfaces"*, T. Härtel, U. Strüber and J. Küppers, Thin Solid Films **229** (1993) 163.

[Hel 98] *"The Flow of Water"*, H. S. Hele-Shaw, Nature **58** (1898) 34.

[Hen 91] *"Oberflächenphysik des Festkörpers"*, M. Henzler and W. Göpel, (Teubner, 1991).

[Her 51] *"Some Theorems on the Free Energies of Crystal Surfaces"*, C. Herring, Phys. Rev. **82** (1951) 87.

[Her 89] *"Molecular Beam Epitaxy"*, M. A. Herman and H. Sitter, (Springer, 1989).

[Hor 87] *"Viscous fingering with imposed uniaxial anisotropy"*, V. Horváth, T. Vicsek and J. Kertész, Phys. Rev. A **35** (1987) 2353.

[Hor 93] *"Formation of interfacial dislocation network in surfactant mediated growth of Ge on Si(111) investigated by SPA-LEED"*, M. H.-v. Hoegen, A. Al-Falou, H. Pietsch, B. H. Müller and M. Henzler, Surf. Sci. **298** (1993) 29.

[Hul 90] *"Principles and Concepts of Strained-Layer Epitaxy"*, R. Hull and J. C. Bean in "Strained-Layer Superlattices: Materials Science and Technology", T. P. Pearsall Eds., (Academic Press, 1990), p. 1.

[Hur 93] *"Handbook of Crystal Growth: 1 Fundamentals; Part A: Thermodynamics and Kinetics"*, D. T. J. Hurle Eds., (North-Holland, 1993).

[Hwa 91] *"Fractal Growth of Two-Dimensional Islands: Au on Ru(0001)"*, R. Q. Hwang, J. Schröder, C. Günther and R. J. Behm, Phys. Rev. Lett. **67** (1991) 3279.

[Jac 94] *"An island shape-induced transition from 2D to 3D growth for Pt/Pt(111)"*, J. Jacobsen, K. W. Jacobsen, P. Stoltze and J. K. Nørskov, to be published .

[Jon 90] *"Energies Controlling Nucleation and Growth Processes: The Case of Ag/W(110)"*, G. W. Jones, J. M. Marcano, J. K. Nørskov and J. A. Venables, Phys. Rev. Lett. **65** (1990) 3317.

[Jul 85] *"Scaling properties of the surface of the Eden model in d = 2, 3, 4"*, R. Jullien and R. Botet, J. Phys. A: Math. Gen. **18** (1985) 2279.

[Kam 94] *"Correlation between Surface Stress and the Vibrational Shift of CO Chemisorbed on Cu Surfaces"*, E. Kampshoff, E. Hahn and K. Kern, Phys. Rev. Lett. **73** (1994) 704.

[Kar 87] *"The Ag-Pt (Silver-Platinum) System"*, I. Karakaya and W. T. Thompson, Bull. Alloy Phase Diagr. **8** (1987) 334.

[Kas 77] *"Growth Kinetics of dislocation-free interfaces and growth-mode of thin films"*, D. Kashchiev, J. Crys. Growth **40** (1977) 29.

[Ker 79] *"Basic Mechanisms in the early Stages of Epitaxy"*, R. Kern, G. L. Lay and J. J. Metois in "Current Topics in Materials Science", E. Kaldis Eds., (North-Holland, 1979), p. 131.

[Ker 82] *"Coalescence of Nuclei on Substrates"*, R. Kern in "Interfacial Aspects of Phase Transformation", B. Mutaftschiev Eds., (Reidel, 1982), p. 303.

[Ker 88] *"Physisorbed Rare Gas Adlayers"*, K. Kern and G. Comsa in "Chemistry and Physics of Solid Surfaces VII", R. Vanselow and R. F. Howe Eds., (Springer, 1988), p. 65.

[Knu 09] *"Experimentelle Bestimmung des Druckes gesättigter Quecksilberdämpfe bei O° und höheren Temperaturen"*, M. Knudsen, Ann. Phys. **29** (1909) 179.

[Kol 84] *"Temperature Dependence of the Work Function of Adsorbate-Covered Metal-Surfaces: A New Method for the Study of Two-Dimensional Phase Transitions"*, J. Kolaczkiewicz and E. Bauer, Phys. Rev. Lett. **53** (1984) 485.

[Kol 851] "Clausius-Clapeyron equation analysis of two-dimensional vaporization", J. Kolaczkiewicz and E. Bauer, Surf. Sci. 155 (1985) 700.

[Kol 852] "Experimental Evidence for Surface Roughening in Two-Dimensions", J. Kolaczkiewicz and E. Bauer, Phys. Rev. Lett. 54 (1985) 574.

[Kol 87] "Phase transition: Condensate-two-dimensional Gas in super thin layers of Cu and Ag adsorbed on the Mo(011) face", J. Kolaczkiewicz, Surf. Sci. 183 (1987) 251.

[Kos 27] "Zur Theorie des Kristallwachstums", W. Kossel, Nachr. Ges. Wiss. (Göttingen) Math.-Phy. Kl. (1927) 135.

[Krz 94] M. Krzyzowski, C. Romainczyk, P. Zeppenfeld, K. Kern and G. Comsa, in preparation (1994) .

[Kui 93] "Step Dynamics on Au(110) Studied with a High-Temperature, High-Speed Scanning Tunneling Microscope", L. Kuipers, M. S. Hoogeman and J. W. M. Frenken, Phys. Rev. Lett. 71 (1993) 3517.

[Kuk 89] "Scanning tunneling microscope instrumentation", Y. Kuk and P. J. Silverman, Rev. Sci. Instrum. 60 (1989) 165.

[Kuk 90] "Optical interactions in the Junction of a Scanning Tunneling Microscope", Y. Kuk, R. S. Becker, P. J. Silverman and G. P. Kochanski, Phys. Rev. Lett. 65 (1990) 456.

[Kun 90] "Reentrant Layer-by-Layer Growth during Molecular-Beam Epitaxy of Metal-on-Metal Substrates", R. Kunkel, B. Poelsema, L. K. Verheij and G. Comsa, Phys. Rev. Lett. 65 (1990) 733.

[Lag 90] "Kinetics of Ordering and Growth at Surfaces", M. G. Lagally Eds., "NATO ASI Series 239", (Plenum Press, 1990).

[Lew 67] "Bond energy formulations of heterogeneous nucleation theory", B. Lewis, Thin solid films 1 (1967) 85.

[Lew 78] "Nucleation and Growth of Thin Films", B. Lewis and J. C. Anderson, (Academic Press, 1978).

[Lin 85] "A simple procedure for high precision orientation of single crystal surfaces", U. Linke and B. Poelsema, J. Phys. E (Sci. Instrum.) 18 (1985) 26.

[Liu 92] "Structure and diffusion of clusters on Ni surfaces", C.-L. Liu and J. B. Adams, Surf. Sci. 268 (1992) 73.

[Liu 93] "Reply to 'Comment on "Structure and diffusion of clusters on Ni surfaces' by C. Massobrio", C.-L. Liu and J. B. Adams, Surf. Sci. 289 (1993) L641.

[Lor 93] "Energy transfer in atom condensation on a crystal", G. D. Lorenzi and G. Ehrlich, Surf. Sci. 293 (1993) L900.

[Lüt 93]   *"Surfaces and interfaces of solids"*, H. Lüth, (Springer, 1993).

[Mad 83]   *"Far from equilibrium vapour phase growth of lattice matched III-V compound semiconductor interfaces: some basic concepts and Monte-Carlo computer simulations"*, A. Madhukar, Surf. Sci. **132** (1983) 344.

[Man 82]   *"The fractal geometry of nature"*, B. B. Mandelbrot, (W.H. Freeman, 1982).

[Man 90]   *"Application of the Frenkel-Kontorova model to surface reconstructions"*, M. Mansfield and R. J. Needs, J. Phys.: Condens. Matter **2** (1990) 2361.

[Mas 931]   *"Structure and dynamics of Ag cluster on Pt(111)"*, C. Massobrio and P. Blandin, Phys. Rev. B **47** (1993) 13687.

[Mas 932]   *"Comment on 'Structure and diffusion of clusters on Ni surfaces by C.-L. Liu and J.B. Adam'"*, C. Massobrio, Surf. Sci. **289** (1993) L638.

[Mat 751]   *"Coherent Interfaces and Misfit Dislocations"*, J. W. Matthews in "Epitaxial growth B", J. W. Matthews Eds., (Academic Press, 1975), p. 559.

[Mat 752]   *"Effect of coherency Strain and Misfit Dislocations on the Mode of Growth of thin Films"*, J. W. Matthews, D. C. Jackson and A. Chambers, Thin Solid Films **26** (1975) 135.

[Mea 83]   *"Diffusion-controlled cluster formation in 2 - 6 dimensional space"*, P. Meakin, Phys. Rev. A **27** (1983) 1495.

[Mea 86]   *"Universality, nonuniversality, and the effects of anisotropy of diffusion-limited aggregation"*, P. Meakin, Phys. Rev. A **33** (1986) 3371.

[Mea 87]   *"Noise-reduced diffusion-limited aggregation"*, P. Meakin, Phys. Rev. A **36** (1987) 332.

[Mea 88]   *"The growth of fractal aggregates and their fractal measures"*, P. Meakin in "Phase transition and critical phenomena", C. Domb and J. L. Lebowitz Eds., (Academic Press, 1988), p. 335.

[Mer 75]   *"Energy of Interfaces between Crystals"*, J. H. v. d. Merve and C. A. B. Ball in "Epitaxial growth B", J. W. Matthews Eds., (Academic Press, 1975), p. 493.

[Mer 84]   *"Recent developments in the theory of epitaxy"*, J. H. v. d. Merve in "Chemistry and Physics of Solid Surfaces V", R. Vanselow and R. Howe Eds., (Springer, 1984), p. 365.

[Mer 94]   *"Role of misfit strain and proximity in epigrowth modes: I. String epilayer-substrate interaction"*, J. H. v. d. Merve, D. L. Tönsing and P. M. Stoop, Surf. Sci. **312** (1994) 387.

[Mey 94] "STM-Untersuchung zum epitaktischen Wachstum von Ag/Si (111) 7x7 bei 80K", G. Meyer and K. H. Rieder, Frühjahrstagung der DPG, O.22.57 (Münster, 1994).

[Mic 88] "A combined scanning tunneling and field ion microscope", T. Michely, K. H. Besocke and M. Teske, J. Microscopy 152 (1988) 77.

[Mic 911] "Rastertunnelmikroskopuntersuchung der Morphologie von Pt(111) nach Ionenbeschuß", T. Michely, Ph.D. Thesis, Bonn, KfA-Jül-Bericht Nr. 2569, (1991).

[Mic 912] "Temperature dependence of the sputtering morphology of Pt(111)", T. Michely and G. Comsa, Surf. Sci. 256 (1991) 217.

[Mic 93] "Inversion of Growth Speed Anisotropy in Two Dimensions", T. Michely, M. Hohage, M. Bott and G. Comsa, Phys. Rev. Lett. 70 (1993) 3943.

[Mie 78] "Surface Energies of Solid Metals", A. R. Miedema, Z. Metallkde. 69 (1978) 287.

[Mil 77] "On Electrostriction", E. J. Mills, Proc. Roy. Soc. London 26 (1877) 504.

[Mo 91] "Activation Energy for Surface Diffusion of Si on Si(001): A Scanning-Tunneling-Microscopy Study", Y. W. Mo, J. Kleiner, M. B. Webb and M. G. Lagally, Phys. Rev. Lett. 66 (1991) 1998.

[Mül 37] "Elektronenmikroskopische Beobachtung von Feldkathoden", E. W. Müller, Z. Phys. 106 (1937) 541.

[Mül 51] "Das Feldionenmikroskop", E. W. Müller, Z. Phys. 131 (1951) 136.

[Mul 63] "Morphological Stability of a Particle Growing by Diffusion or Heat Flow", W. W. Mullins and R. F. Sekerka, J. Appl. Phys. 34 (1963) 323.

[Mur 90] "Proximal Probes: Techniques for Measuring at the Nanometer Scale", J. S. Murday and R. J. Colton in "Chemistry and Physics of Solid Surfaces VIII", R. Vanselow and R. F. Howe Eds., (Springer, 1990), p. .

[Mye 93] "The Structure of Supersaturated Solutions", A. S. Myerson and A. F. Izmailov in "Handbook of Crystal Growth: 1 Fundamentals; Part A: Thermodynamics and Kinetics", D. T. J. Hurle Eds., (North-Holland, 1993), p. 251.

[Nak 54] "Snow Crystals", U. Nakaya, (Harvard University Press, 1954).

[Nar 92] "Elastic Stress Domains and the Herringbone Reconstruction on Au(111)", S. Narasimhan and D. Vanderbilt, Phys. Rev. Lett. 69 (1992) 1564.

[Nee 91]   "Theory of surface stress and surface reconstructions", R. J. Needs, M. J. Godfrey and M. Mansfield, Surf. Sci. **242** (1991) 215.

[Neu 70]   "Condensation, Nucleation and Growth of Thin Films", C. A. Neugebauer in "Handbook of thin film technology", L. I. Maissel and R. Glong Eds., (McGraw-Hill, 1970), p. 8.

[Nie 93]   "Initial Growth of Au on Ni(110): Surface Alloying of Immiscible Metals", L. P. Nielsen, F. B. F., I. Stensgaard, E. Lægsgaard, C. Engdahl, P. Stolze, K. W. Jacobsen and J. K. Nørskov, Phys. Rev. Lett. **71** (1993) 754.

[Nit 86]   "Tip splitting without interfacial tension and dendritic growth patterns arising from molecular anisotropy", J. Nittmann and H. E. Stanley, Nature **321** (1986) 663.

[Nit 87]   "Non-deterministic approach to anisotropic growth patterns with continuously tunable morphology: the fractal properties of some real snowflakes", J. Nittmann and H. E. Stanley, J. Phys. A: Math. Gen. **20** (1987) L1185.

[Nør 93]   "Many-atom interaction in metals", J. K. Nørskov, K. W. Jacobsen, P. Stoltze and L. B. Hansen, Surf. Sci. **283** (1993) 277.

[Ohr 92]   "The Materials Science of Thin Films", M. Ohring, (Academic Press, 1992).

[Ost 00]   "Über die vermeintliche Isomerie des roten und gelben Quecksilberoxyds und die Oberflächenspannung fester Körper", W. Ostwald, Z. Phys. Chem. **34** (1900) 495.

[Paf 85]   "Surface chemical properties of Ag/Pt(111): Comparisons between electrochemistry and surface science", M. T. Paffet, C. T. Campbell and T. N. Taylor, Langmuir **1** (1985) 741.

[Pal 681]   "Atomic Arrangement of Au(100) and Related Metal Overlayer Surface Structures. I", P. W. Palmberg and T. N. Rhodin, J. Chem. Phys. **49** (1968) 134.

[Pal 682]   "Analysis of Low-Energy Electron Diffraction patterns from simple overlayer surface structures. II", P. W. Palmberg and T. N. Rhodin, J. Chem. Phys. **19** (1968) 147.

[Par 85]   "The Technology and Physics of Molecular Beam Epitaxy", E. H. C. Parker Eds., (Plenum Press, 1985).

[Pas 75]   "A historical review of epitaxy", D. W. Pashley in "Epitaxial growth", J. W. Matthews Eds., (Academic Press, 1975), p. 1.

[Pau 60]   "The Chemical Bond", L. Pauling, (Cornell University Press, 3rd ed., 1960).

[Pea 90]   "*Strained-Layer Superlattices*", T. P. Pearsall in "Strained-Layer Superlattices: Materials Science and Technology", T. P. Pearsall Eds., (Academic Press, 1990), p. 1.

[Pee 90]   "*Fundamental issues in heteroepitaxy - A Department of Energy, Council on Materials Science Panel Report*", P. S. Peercy, et al., J. Mater. Res. 5 (1990) 852.

[Per 74]   "*Adsorption and surface alloying of lead monolayers on (111) and (110) faces of gold*", J. Perdereau, J. P. Biberian and G. E. Rhead, J. Phys. F 4 (1974) 798.

[Per 86]   "*Inelastic Electron Tunnelling from a Metal Tip*", B. N. J. Persson and J. E. Demuth, Sol. Sta. Com. 57 (1986) 769.

[Per 92]   "*Ordered structures and phase transitions in adsorbed layers*", B. N. J. Persson, Surf. Sci. Rep. 15 (1992) 1.

[Pim 93]   "*Fractal terraces in MBE growth*", A. Pimpinelli, J. Villain and D. E. Wolf, J. Phys. I (France) 3 (1993) 447.

[Poe 91]   "*New Phenomena in Homoepitaxial Growth of Metals*", B. Poelsema, R. Kunkel, N. Nagel, A. F. Becker, G. Rosenfeld, L. K. Verheij and G. Comsa, Appl. Phys. A 53 (1991) 369.

[Poe 92]   "*Step dynamics on Ag(111) and Cu(100) surfaces*", M. Poensgen, J. F. Wolf, J. Frohn, M. Giesen and H. Ibach, Surf. Sci. 274 (1992) 430.

[Poe 93]   B. Poelsema, personal communication.

[Poh 86]   "*Some design criteria in scanning tunneling microscopy*", D. W. Pohl, IBM J. Res. Develop. 30 (1986) 417.

[Por 81]   "*Phase Transformations in Metals and Alloys*", D. A. Porter and K. E. Easterling, (Van Nostrand Reinhold Co. Ltd., 1981).

[Pöt 91]   "*Interface structure and misfit dislocations in thin Cu films on Ru(0001)*", G. O. Pötschke and R. J. Behm, Phys. Rev. B 44 (1991) 1442.

[Rae 92]   "*Alloy formation energetics and dynamics in the Ni/Cu(100) and Ni/Cu(111) systems*", T. J. Raeker and A. E. DePristo, J. Vac. Sci. Technol. A 10 (1992) 2396.

[Rae 94]   "*The definition and calculation of interfacial energies for thin films*", T. J. Raeker and A. E. DePristo, Surf. Sci. 310 (1994) 337.

[Ran 94]   "*Stacking of Ag layers on Pt(111)*", G. Rangelov, T. Fauster, U. Strüber and J. Küppers, Surf. Sci. submitted (Proc. ECOSS - 14) (1994) .

[Rob 64]   "*Nucleation of metal crystals on ionic surfaces*", J. L. Robins and T. N. Rhodin, Surf. Sci. 2 (1964) 346.

[Röd 91] *"Aufbau einer UHV-Kombinationsapparatur: Rastertunnel-mikroskopie und IR-Spektroskopie an Halbleiteroberflächen"*, H. Röder, Diplomarbeit, Universität Bonn, (1991).

[Rod 92] *"FT-IRAS studies of CO adsorbed on Ag/Pt(111): anomalous behavior of vibrational cross-sections"*, J. A. Rodriguez, C. M. Truong and D. W. Goodmann, Surf. Sci. 271 (1992) L331.

[Roh 94] *"Scanning tunneling microscopy: a surface science tool and beyond"*, H. Rohrer, Surf. Sci. 299/300 (1994) 956.

[Rom 93] The evaluation of the fractal dimensions has been performed by C. Romainczyk.

[Rom 94] C. Romaninczyk, M. A. Krzyzowski, P. Zeppenfeld, K. Kern, R. David and G. Comsa, in preparation (1994) .

[Ros 93] *"Layer-by-layer growth of Ag on Ag(111) induced by enhanced nucleation: A Model Study for Surfactant-Mediated Growth,"*, G. Rosenfeld, R. Servaty, C. Teichert, B. Poelsema and G. Comsa, Phys. Rev. Lett. 71 (1993) 895.

[Roy 28] *"Recherches expérimentales sur l'épitaxie ou orientation mutuelle de cristaux d'espèces différentes"*, L. Royer, Bull. Soc. Fr. Mineral. Cristallogr. 51 (1928) 7.

[Roy 86] *"Quantum Mechanical Tunnelling and its Applications"*, D. K. Roy, (World Scientific, 1986).

[Saf 58] *"The penetration of a fluid into a porous medium or Hele-Shaw cell containing a more viscous liquid"*, P. G. Saffman and G. J. Taylor, Proc. Roy. Soc. London Ser. A 245 (1958) 312.

[San 911] *"Metal/metal homo-epitaxy on fcc (001) surfaces: Is there transient mobility of adsorbed atoms?"*, D. E. Sanders and A. E. DePristo, Surf. Sci. 254 (1991) 341.

[San 912] *"Structure and Phases of the Au(111) Surface: X-Ray Scattering Measurements"*, A. R. Sandy, S. G. J. Mochrie, D. M. Zehner, G. Grübel, K. G. Huang and D. Gibbs, Phys. Rev. B 43 (1991) 4667.

[San 92] *"Reconstruction of the Pt(111) surface"*, A. R. Sandy, S. G. J. Mochrie, D. M. Zehner, G. Grübel, K. G. Huang and D. Gibbs, Phys. Rev. Lett. 68 (1992) 2192.

[Saw 86] *"Dendritic and Fractal Patterns in Electrolytic Metal Deposits"*, Y. Sawada, A. Dougherty and J. P. Gollub, Phys. Rev. Lett. 56 (1986) 1260.

[Sche 93] *"Historical Introduction"*, H. J. Scheel in "Handbook of Crystal Growth: 1 Fundamentals; Part A: Thermodynamics and Kinetics", D. T. J. Hurle Eds., (North-Holland, 1993), p. 1.

[Schm 89]   "Coverage dependence of the spin-resolved photoemission from epitaxially grown Ag layers on Pt(111)", B. Schmiedeskamp, B. Kessler, B. Vogt and U. Heinzelmann, Surf. Sci. 223 (1989) 465.

[Schm 92]   "Analysis of vibration-isolating systems for scanning tunneling microscopes", M. Schmid and P. Varga, Ultramicroscopy 42-44 (1992) 1610.

[Schm 93]   "Direct Observation of Surface Chemical Order by Scanning Tunneling Microscopy", M. Schmid, H. Stadler and P. Varga, Phys. Rev. Lett. 70 (1993) 1441.

[Schr 92]   "A comparative STM study of the growth of thin Au films on clean and oxygen-precovered Ru(0001) surfaces", J. Schröder, C. Günther, R. Q. Hwang and R. J. Behm, Ultramicroscopy 42-44 (1992) 475.

[Schu 922]   "Distance dependence and corrugation in barrier-height measurements on metal surfaces", R. Schuster, J. V. Barth, J. Winterlin., R. J. Behm and G. Ertl, Ultramicroscopy 42-44 (1992) 533.

[Schw 66]   "Step Motion on Crystal Surfaces", R. L. Schwoebel and E. J. Shipsey, J. Appl. Phys. 37 (1966) 3682.

[Sie]   Siemens, Kunststoff u. Porzellanwerk Redwitz, D-96257 Redwitz, Germany.

[Smi 75]   "Theory of Electronic Properties of Surfaces", J. R. Smith in "Interactions on Metal Surfaces", R. Gomer Eds., (Springer, 1975), p. 1.

[Smo 06]   "Zur kinetischen Theorie der Brownschen Molekular-bewegung und der Suspension", M. v. Smoluchowski, Ann. Phys. 21 (1906) 756.

[Spi 83]   "UHV-SEM Study of the Nucleation and growth of Ag/W(110)", G. D. T. Spiller, P. Akhter and J. A. Venables, Surf. Sci. 131 (1983) 517.

[Sta 86]   "On Growth and Form: Fractal and Non-Fractal Patterns in Physics", H. E. Stanley and N. Ostrowsky Eds., "NATO ASI Series E: Applied Sciences 100", (Martinus Nijhoff Publishers, 1986).

[Sto 81]   "Thin Film Nucleation and Growth Theories: A Confrontation with Experiment", S. Stoyanov and D. Kashchiev in "Current Topics in Materials Science", E. Kaldis Eds., (North-Holland, 1981), p. 67.

[Stra 38]   "Zur Theorie der orientierten Ausscheidung von Ionen-kristallen aufeinander", I. N. Stranski and L. Krastanov, Ber. Akad. Wiss. Wien, Math.-natur. Kl IIb 146 (1938) 797.

[Stro 93]   "Homoepitaxial Growth of Iron and a Real Space View of Reflection-High-Energy-Electron Diffraction", J. A. Stroscio, D. T. Pierce and R. A. Dragoset, Phys. Rev. Lett. 70 (1993) 3615.

[Stro 94]   *"Scaling of diffusion-mediated island growth in iron-on-iron homoepitaxy"*, J. A. Stroscio and D. T. Pierce, Phys. Rev. B **49** (1994) 8522.

[Strü 93]   *"Spectroscopic confirmation of STM derived Ag/Pt mixing in annealed Ag submonolayers at Pt(111) surfaces"*, U. Strüber and J. Küppers, Surf. Sci. **294** (1993) L924.

[Strü 94]   *"Ag layers on Pt(100), (110) and (111) surfaces - how does the substrate structure affect overlayer growth"*, U. Strüber and J. Küppers, Thin Solid Films submitted (1994) .

[Stu 941]   *"Theory of Self-Diffusion at and Growth of Al(111)"*, R. Stumpf and M. Scheffler, Phys. Rev. Lett. **72** (1994) 254.

[Stu 942]   *"Ab-initio Calculations of Energetics and Self-Diffusion on Flat and Stepped Surfaces of Al and its Implications on Epitaxial Growth"*, R. Stumpf and M. Scheffler, Phys. Rev. B submitted (1994) .

[Tak 90]   *"Fractals in the physical sciences"*, H. Takayasu, (Manchester University Press, 1990).

[Tan 81]   *"UHV Transmission Electron Microscopy on the Reconstructed Surface of (111) Gold"*, Y. Tanishiro, H. Kanamori, K. Takayanagi, K. Yagi and G. Honjo, Surf. Sci. **111** (1981) 395.

[Ter 83]   *"Theory and Application for the Scanning Tunneling Microscope"*, J. Tersoff and D. R. Hamann, Phys. Rev. Lett. **50** (1983) 1998.

[Ter 85]   *"Theory of the scanning tunneling microscope"*, J. Tersoff and D. R. Hamann, Phys. Rev. B **31** (1985) 805.

[Ter 941]   *"Critical Island Size for Layer-by-Layer Growth"*, J. Tersoff, A. W. D. v. d. Gon and R. M. Tromp, Phys. Rev. Lett. **72** (1994) 266.

[Ter 942]   *"Competing Relaxation Mechanisms in Strained Layers"*, J. Tersoff and F. K. LeGoues, Phys. Rev. Lett. **72** (1994) 3570.

[Veg 92]   *"Surfactant-induced layer-by-layer growth of Ag on Ag(111)"*, H. A. v. d. Vegt, H. M. v. Pinxteren, M. Lohmeier and E. Vlieg, Phys, Rev. Lett. **68** (1992) 3335.

[Ven 73]   *"Rate Equation Approaches to Thin Film Nucleation Kinetics"*, J. A. Venables, Philos. Mag. **17** (1973) 697.

[Ven 84]   *"Nucleation and growth of thin films"*, J. A. Venables, G. D. T. Spiller and M. Hanbücken, Rep. Prog. Phys. **47** (1984) 399.

[Ven 86]   *"Nucleation and growth processes in thin film formation"*, J. A. Venables, J. Vac. Sci. Technol. **B 4 (4)** (1986) 870.

[Ven 87]   *"Nucleation calculations in a pair-binding model"*, J. A. Venables, Phys. Rev. B **36** (1987) 4153.

[Vic 89]   *"Fractal Growth Phenomena"*, T. Vicsek, (World Scientific, 1989).

[Vil 92]   *"Layer by Layer growth in Molecular Beam Epitaxy"*, J. Villain, A. Pimpinelli and D. E. Wolf, Com. Cond. Mat Phys. 16 (1992) 1.

[Vil 941]   *"Low-temperature homoepitaxial growth of Pt(111) in simulated vapor deposition"*, M. Villarba and H. Jónsson, Phys. Rev. B 49 (1994) 2208.

[Vil 942]   *"Diffusion mechanisms relevant to metal crystal growth: Pt/Pt(111)"*, M. Villarba and H. Jónsson, Surf. Sci. 317 (1994) 15.

[Vol 26]   *"Keimbildung in übersättigten Gebilden"*, M. Volmer and A. Weber, Z. Phys. Chem. 119 (1926) 277.

[Voo 92]   *"Ostwald Ripening of Two-Phase Mixtures"*, P. W. Voorhees, Annu. Rev. Mater. Sci. 22 (1992) 197.

[Vri 94]   *"Surfactant-Induced Layer-by-Layer growth of Ag on Ag(111): Origins and Side Effects"*, J. Vrijmoeth, H. A. v. d. Vegt, J. A. Meyer, E. Vlieg and R. J. Behm, Phys. Rev. Lett. 72 (1994) 3843.

[Wah 90]   *"Rate Equations, Rate Constants and Surface Diffusion"*, G. Wahnström in "Interaction of atoms and molecules with solid surfaces", V. Bortolani, N. H. March and M. P. Tosi Eds., (Plenum Press, 1990), p. 529.

[Wal 62]   *"Nucleation of Vapor Deposits"*, D. Walton, J. Chem. Phys. 37 (1962) 2182.

[Wan 89]   *"Binding sites for cluster atoms: Ir on Ir(111)"*, S. C. Wang and G. Ehrlich, Surf. Sci 217 (1989) L397.

[Wan 90]   *"Structure, stability, and surface diffusion of clusters: Ir_x on Ir(111)"*, S. C. Wang and G. Ehrlich, Surf. Sci 239 (1990) 301.

[Wan 911]   *"Atom condensation on an atomically smooth surface: Ir, Re, W, and Pd on Ir(111)"*, S. C. Wang and G. Ehrlich, J. Chem Phys. 94 (1991) 4071.

[Wan 912]   *"Atom incorporation at Surface Clusters: An Atomic View"*, S. C. Wang and G. Ehrlich, Phys. Rev. Lett. 67 (1991) 2509.

[Wan 931]   *"Adatom Motion to Lattice Steps: A Direct View"*, S. C. Wang and G. Ehrlich, Phys. Rev. Lett. 70 (1993) 41.

[Wan 932]   *"Atom Condensation at Lattice Steps and Clusters"*, S. C. Wang and G. Ehrlich, Phys. Rev. Lett. 71 (1993) 4174.

[Wan 94]   *"An investigation of the energetics and dynamics of adatom motion to descending-step edges in Pt/Pt(111) homoepitaxy"*, R. Wang and K. A. Fichthorn, Surf. Sci. 301 (1994) 253.

[Wei 92]   *"Adsorption and Accommodation of Xe on Pt(111)"*, P. S. Weiss and D. M. Eigler, Phys. Rev. Lett. **69** (1992) 2240.

[Wic 89]   *"Scanned-Probe Microscopes"*, H. K. Wickramasinghe, Sci. Am. **261(4)** (1989) 74.

[Win 89]   *"Atomic-Resolution of Close-Packed Metal Surfaces by Scanning Tunneling Microscopy"*, J. Wintterlin, J. Wiechers, H. Brune, T. Gritsch, H. Höfer and R. J. Behm, Phys. Rev. Lett. **62** (1989) 59.

[Win 92]   *"Adsorbate Covered Metal Surfaces and Reactions on Metal Surfaces"*, J. Wintterlin and R. J. Behm in "Scanning Tunneling Microscopy I", H.-J. Güntherodt and R. Wiesendanger Eds., (Springer, 1992), p. 39.

[Wit 81]   *"Diffusion-Limited aggregation, a Kinetic Critical Phenomenon"*, T. A. Witten and L. M. Sander, Phys. Rev. Lett. **47** (1981) 1400.

[Wit 83]   *"Diffusion-limited aggregation"*, T. A. Witten and L. M. Sander, Phys. Rev. B **27** (1983) 5686.

[Wol 90]   *"Untersuchung von Defekten auf einer gestuften Ag(111)-Fläche mit einem Tieftemperatur-Rastertunnelmikroskop und hochauflösender Elektronenbeugung"*, J. K. Wolf, Ph.D.Thesis, T.H. Aachen, KfA-Jül-Bericht Nr. 2391, (1990).

[Wol 91]   *"Dislocations on Ag(111)"*, J. F. Wolf and H. Ibach, Appl. Phys. A **52** (1991) 218.

[Wul 01]   *"Zur Frage der Geschwindigkeit des Wachsthums und der Auflösung der Kristallflächen"*, G. Wulff, Zeitschr. f. Kristallog u. Miner. **34** (1901) 449.

[You 05]   T. Young, Philos. Trans **95** (1805) 65.

[Zan 88]   *"Physics at Surfaces"*, A. Zangwill, (Cambridge University Press, 1988).

[Zan 91]   *"Epitaxial phenomena"*, A. Zangwill, (cours du troisième cycle de la physique en suisse romande, 1991).

[Zan 93]   *"Scaling Description of Sub-Monolayer Epitaxial Growth"*, A. Zangwill in "Evolution of Surface and Thin Film Microstructure", H. A. Atwater, E. Chason, M. H. Grabow and M. G. Lagally Eds., (Material Research Society, Symposium Proceedings Vol. 280, 1993), p. 121.

[Zep 911]   *"Imaging Close-Packed Metal Surfaces in Scanning Tunneling Microscopy"*, P. Zeppenfeld, C. P. Lutz and D. M. Eigler, 6th International Conference on Scanning Tunneling Microscopy (Interlaken, 1991).

[Zep 912]   P. Zeppenfeld and E. K. Schweizer, personal communication.

[Zep 92]   "Manipulating atoms and molecules with a scanning tunneling microscope", P. Zeppenfeld, C. P. Lutz and D. M. Eigler, Ultramicroscopy 42-44 (1992) 128.

[Zep 941]   "Size Relation for Surface Systems with Long-Range Interactions", P. Zeppenfeld, M. Krzyzowski, C. Romainczyk, G. Comsa and M. G. Lagally, Phys.Rev.Lett. 72 (1994) 2737.

[Zep 942]   "Stability of Disk and Stripe Patterns of Nanostructures at Surfaces", P. Zeppenfeld, M. Krzyzowski, C. Romainczyk, R. David, a. G. Comsa, H. Röder, K. Bromann, H. Brune and K. Kern, to be published (1994)
.

[Zha 94]   "Atomic-Scale Mechanisms for Surfactant-Mediated Layer-by-Layer Growth in Homoepitaxy", Z. Zhang and M. G. Lagally, Phys. Rev. Lett. 72 (1994) 693.

[Zin 66]   "A contribution to Frenkel's theory of condensation", G. Zinsmeister, Vacuum 16 (1966) 529.

[Zin 92]   "Clustering on surfaces", M. Zinke-Allmang, L. C. Feldman and M. H. Grabow, Surf. Sci. Rep. 16 (1992) 377.

[Zuo 94]   "Growth and Coalescence in Submonolayer Homoepitaxy on Cu(100) studied with High-Resolution Low-Energy Electron Diffraction", J.-K. Zuo, J. F. Wendelken, H. Dürr and C.-L. Liu, Phys. Rev. Lett. 72 (1994) 3064.

Merci - Danke - Thanks - Grazie !

à Claire-Lise Bandelier, qui a réalisé la plupart des figures de ce manuscrit. J'ai admiré sa patience devant mes caprices et son souci de perfection pour obtenir des images de la meilleure qualité possible;

à Christine Goyhenex, Karsten Bromann, Harri Brune, Alex Fricke, Scott Gilbert, Klaus Kuhnke, Bjørn Fischer, Vittorio Marsico, Andreas Hirstein et Hansjörg Schief pour leur attention et leurs critiques constructives au cours de la lecture des différentes parties du manuscrit. Une mention spéciale va à l'équipe des "cinq dernières minutes";

à tout le personnel techniques de l'institut pour leur aide et leurs compétences indispensables au bon déroulement des expériences. Je veux spécialement remercier Philippe Zurcher et Yves Morier pour la réalisation des pièces mécaniques du manipulateur du STM ainsi que Philippe Cordey pour la construction de la partie électronique du microscope.

Ce projet a profité du support matériel et financier de l'Ecole Polytechnique Fédérale de Lausanne et le Fonds National Suisse sans lesquels cette recherche n'aurait pas été possible.

Enfin, j'aimerais remercier Elmar Hahn, mon vieux "compagnon de route" durant ces années, pour la bonne ambiance dans le laboratoire et ailleurs, ainsi que Christine Goyhenex qui a sacrifié une grande partie de ses vacances à supporter un physicien pendant la rédaction de sa thèse.

Finalement, ma reconnaissance va par dessus tout à mes parents qui m'ont toujours encouragé et soutenu activement, durant mes études et tout au long de ce travail.

Curriculum Vitae

Nom:		**Holger Röder**
Adresse:		Avenue de Préfaully 25 c
		CH-1022 Chavannes
		Suisse
Date de naissance:		13 Mars 1965
Lieu de naissance:		Bremen (Allemagne)
Situation de famille:		célibataire
Nationalité:		allemande

Formation:

Ecole primaire:	1971 - 1975	Bremen, Bonn (Allemagne)
Gymnase:	1975 - 1984	Baccalauréat général, Bonn

Service militaire: 1984 - 1985 Rheinbach (Allemagne)

Etudes :

Physique:	1985 - 1990	Université de Bonn
Travail de diplôme:	1990 - 1991	Centre de recherche (KfA) de Jülich
		(Allemagne) sous la direction du Prof.
		G. Comsa
Sujet:		Physique de surface par la
		microscopie à effet tunnel et la
		spectroscopie infrarouge
Electrotechnique:	1984 - 1994	Université de Hagen (Allemagne);
		enseignement à distance (examen
		intermédiaire d'ingénieur en 1990)

Doctorat: 1991 - 1994

Doctorat: 1991 - 1994	Ecole Polytechnique Fédérale de
	Lausanne (EPFL) sous la direction du
	Prof. K. Kern
Domaine de recherche:	Croissance des couches minces
	métalliques

Liste des publications

1) *"Thermally induced disorder and conformational defects of alkane monolayers on graphite"*
   Jean-Pierre Bucher, Holger Röder and Klaus Kern,
   Surface Science **289** (1993) 370

2) *"Structure and complete chemical passivation of Pt(997)"*
   Elmar Hahn, Alexander Fricke, Holger Röder and Klaus Kern,
   Surface Science **297** (1993) 19

3) *"Monolayer-confined mixing at the Ag-Pt(111) interface"*
   Holger Röder, Rolf Schuster, Harald Brune and Klaus Kern,
   Physical Review Letters **71** (1993) 2086

4) *"Changing morphology of metallic monolayers via temperature controlled heteroepitaxial growth"*
   Holger Röder, Harald Brune, Jean-Pierre Bucher and Klaus Kern,
   Surface Science **298** (1993) 121

5) *"Building one- and two-dimensional nanostructures by diffusion-controlled aggregation at surfaces"*
   Holger Röder, Elmar Hahn, Harald Brune, Jean-Pierre Bucher and Klaus Kern, Nature **366** (1993) 141

6) *"Strain relief at hexagonal close packed interfaces"*
   Harald Brune, Holger Röder, Corrado Boragno and Klaus Kern,
   Physical Review B **49** (1994) 2997

7) *"Fractal and dendritic growth patterns in two dimensions"*
   Harald Brune, Christoph Romainczyk, Holger Röder and Klaus Kern,
   Nature **369** (1994) 469

8) *"Microscopic View of thin film growth"*
   Holger Röder, Harald Brune, Corrado Boragno, Christoph Romainczyk and Klaus Kern, Proceedings of "Physique en Herbe 94", Montpellier, France

9) *"A microscopic view of nucleation on surfaces"*
   Harald Brune, Holger Röder, Corrado Boragno and Klaus Kern,
   Physical Review Letters **73** (1994) 1955

10) *"Roughening and fragmentation of strained Ag islands on Pt(111)"*
   Holger Röder, Harald Brune and Klaus Kern,
   Physical Review Letters, **73** (1994) 2143

11) *"Aggregation of fractal and dendritic Ag clusters on a Pt(111) surface"*
   Harald Brune, Holger Röder, Christoph Romainczyk, Corrado Boragno and Klaus Kern, Applied Physics A, accepted for publication